Formation and evolution of dust and molecules in the supernova remnant Cassiopeia A

Inauguraldissertation

zur
Erlangung der Würde eines Doktors der Philosophie
vorgelegt der
philosophisch-naturwissenschaftlichen Fakultät
der Universität Basel
von

Chiara Biscaro

aus Italien

Basel, 2015

Genehmigt von der philosophisch-naturwissenschaftlichen Fakultät

auf Antrag von

Prof. Dr. Friedrich-Karl Thielemann, PD Dr. Isabelle Cherchneff und Prof. Dr. Anthony Jones.

Basel, den 16. September 2014

Prof. Dr. Jörg Schibler

Namensnennung-Keine kommerzielle Nutzung-Keine Bearbeitung 3.0 Schweiz
(CC BY-NC-ND 3.0 CH)

Sie dürfen: **Teilen** — den Inhalt kopieren, verbreiten und zugänglich machen

Unter den folgenden Bedingungen:

Namensnennung — Sie müssen den Namen des Autors/Rechteinhabers in der von ihm festgelegten Weise nennen.

Keine kommerzielle Nutzung — Sie dürfen diesen Inhalt nicht für kommerzielle Zwecke nutzen.

Keine Bearbeitung erlaubt — Sie dürfen diesen Inhalt nicht bearbeiten, abwandeln oder in anderer Weise verändern.

Wobei gilt:

- **Verzichtserklärung —** Jede der vorgenannten Bedingungen kann **aufgehoben** werden, sofern Sie die ausdrückliche Einwilligung des Rechteinhabers dazu erhalten.
- **Public Domain (gemeinfreie oder nicht-schützbare Inhalte) —** Soweit das Werk, der Inhalt oder irgendein Teil davon zur Public Domain der jeweiligen Rechtsordnung gehört, wird dieser Status von der Lizenz in keiner Weise berührt.
- **Sonstige Rechte —** Die Lizenz hat keinerlei Einfluss auf die folgenden Rechte:
    - Die Rechte, die jedermann wegen der Schranken des Urheberrechts oder aufgrund gesetzlicher Erlaubnisse zustehen (in einigen Ländern als grundsätzliche Doktrin des **fair use** bekannt);
    - Die **Persönlichkeitsrechte** des Urhebers;
    - Rechte anderer Personen, entweder am Lizenzgegenstand selber oder bezüglich seiner Verwendung, zum Beispiel für **Werbung** oder Privatsphärenschutz.
- **Hinweis —** Bei jeder Nutzung oder Verbreitung müssen Sie anderen alle Lizenzbedingungen mitteilen, die für diesen Inhalt gelten. Am einfachsten ist es, an entsprechender Stelle einen Link auf diese Seite einzubinden.

Quelle: http://creativecommons.org/licenses/by-nc-nd/3.0/ch/ Datum: 12.11.2013

Abstract

This PhD thesis addresses the formation of molecules and dust in the ejecta of supernovae (SNe) of Type IIb and in their following reprocessing by shocks in the supernova remnant (SNR), with a focus on the Cassiopeia A (Cas A) remnant. Cas A is a young (∼300 years), close by (3.4 kpc) SNR, where the reverse shock is currently reprocessing the material formed after the SN explosion. Recent observation of dust and molecules with *Herschel* and ALMA in Cas A, as well as in the young SNR 1987A pose the question whether SNe and SNRs are efficient dust providers to the galaxy. It is not clear how much dust is formed in SNe ejecta, as well as how much is destroyed by the inward reverse shock during the remnant phase. High dust mass are inferred from the reddening of quasars at high redshift, pointing to SNe as the main source of dust at early times. At the moment, theory and observations disagree on the amount of dust formed in SNe ejecta, with lower dust masses observed than predicted by theories.

In this thesis, we want to assess how much dust and molecules form in Cas A ejecta, and how much survive the reprocessing by the reverse shock, in order to infer if SNe Type IIb are dust providers or destroyers.

We first model the SN ejecta chemistry to identify the molecules and dust clusters that form after the explosion and are reprocessed by the reverse shock. We find that Cas A progenitor could have formed large quantities of molecules and dust only in a dense ejecta involving clumps. We then model the impact of the reverse shock on oxygen and carbon-rich ejecta clumps, considering various reverse shock speeds and investigating the post-shock chemistry. We found that the reverse shock destroys the molecules and clusters present in the O-rich clump. CO reforms in the post shock gas with abundances that concur with recent *Herschel* observations of shocked clumps in Cas A. We derive a dust size distribution for the ejecta of the Cas A progenitor, and investigate the effect of different reverse shock velocities on this dust size distribution. After the clump disruption by the reverse shock, we investigate dust reprocessing by the hot interclump medium.

Results show that medium- and large-sized grains in clumps survive the reverse shock and that small dust clusters do not efficiently reform in the shocked gas. This result indicates that the dust formed in the SN ejecta and destroyed by the reverse shock is unable to reform from the gas phase in the SN remnant. Once the grains are released in the hot interclump medium, small grains are quickly destroyed, while only the larger ones survive. Oxide grains are almost completely destroyed, pointing to the inability of SN Type IIb to contribute significantly to the galactic dust budget. Large grains, with radius ~ 1 μm (such as formed in Type IIP SNe) are required to survive the remnant phase. Carbon and silicon carbide grains are more resistant, and survive even at smaller radii. SNRs with dense clumps and dust grain size distributions including large grains can be significant contributors to the dust budget in the early as well as in the local universe.

List of Figures

List of Tables

Contents

1. Introduction

1.1 Massive stars and supernovae

1.1.1 Life of a massive star

Massive star are defined as stars with mass $\gtrsim 8$ $M_\odot$. This classification is justified by the possibility for massive star to ignite the burning of carbon and heavy elements after the first burning of hydrogen and helium. These stars are important contributors of heavy elements, in particular of α elements such as ^{16}O, ^{20}Ne, ^{24}Mg, ^{28}Si, ^{32}S, ^{36}Ar, ^{40}Ca, ^{48}Ti. Part of the heavy elements formed in the star are returned to the ISM when the star end its life in a supernova (SN) explosion, contributing to the chemical enrichment of the galaxy.
Massive stars are born in giant molecular clouds that have typical densities of 100 cm^{-3}, a diameter of ~ 30 pc, and masses up to 6×10^6 $M_\odot$ (Williams et al., 2000). The collapse of such a cloud to protostars is possibly triggered by one of several events, including molecular clouds collisions, a shock from a nearby SN, or galactic collisions. The protostar will continue to collapse as long as there is a way to eliminate gravitational energy, through radiation from the cloud itself and from the heated dust. When the increasing density makes the material opaque, some energy is released by the dissociation of H_2 molecules and the subsequent ionization of hydrogen and helium atoms. High mass stars can further continue to accrete mass while their core temperature rises, until density and temperature are high enough to begin fusion.

Hydrogen burning

The required core temperature for hydrogen burning is $\geq 3 \times 10^7$ K, while the required density is around a few g cm^{-3}. For massive stars, the primary channel for fusing H to He is the CNO-cycle (see Figure 1.1).

The start of hydrogen fusion marks the start of the star main sequence phase, which lasts for most of its life. The release of nuclear energy by fusion compensate for the star self-gravity, producing a constant pressure gradient and halting the collapse. During this phase, a massive star converts four protons into one helium nucleus via the CNO-cycle, releasing 25 MeV. It uses nuclei of carbon, nitrogen and oxygen as catalysts to produce helium. The pp-cycle is also contributing to the burning, but its contribution is less efficient with respect to the CNO-cycle at the high temperatures in the cores of massive stars. This process creates helium by first fusing two protons into deuterium, followed by a deuterium burning reaction, releasing about 26.2 MeV.

Helium burning

Once the hydrogen is exhausted in the center of the star, burning of helium begins in a shell around the degenerate core if the central temperature is $\geq 10^8$ K. The increasing thermal pressure due to helium burning leads to an expansion of the outer layers of the

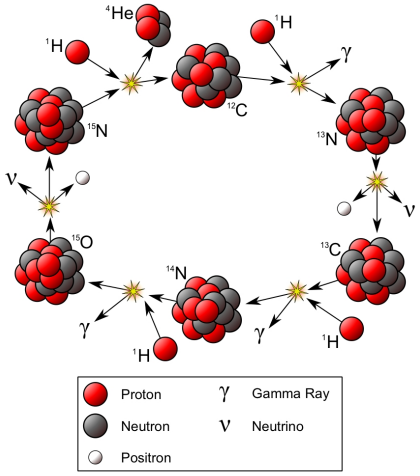

Figure 1.1: Schematic representation of the CNO cycle (Wikimedia commons)

star, with strong mass loss. The expansion and cooling of the outer layers will bring the star in the red giant branch of the Hertzsprung-Russel diagram.

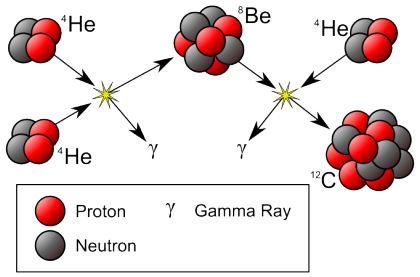

Figure 1.2: Schematic representation of the triple α process (Wikimedia commons)

The main source of nuclear energy is the so called triple α process, in which three helium nuclei are burned into carbon. The process needs a first step in which two helium nuclei form an unstable beryllium nucleus. When the temperature is $\geq 10^8$ K, the rate of formation of beryllium is greater than its decay rate, and the process may go on with the addition of one more helium nucleus.
During the helium burning phase, the formation of ^{22}Ne via the the process

$$^{14}\mathrm{N}(\alpha,\gamma)^{18}\mathrm{F}(\mathrm{e}^{+}\nu_{\mathrm{e}})^{18}\mathrm{O}(\alpha,\gamma)^{22}\mathrm{Ne} \tag{1.1}$$

is important for the formation of elements heavier than iron, since ^{22}Ne is the main neutron source of the s process.

Carbon burning

Massive stars continue their burning after the exhaustion of helium with the fusion of heavier elements, starting from carbon. This burning phase requires temperatures $\geq 5 \times 10^8$ K and densities $\geq 3 \times 10^6$ g cm^{-3}.
The sequence of reactions starts with two carbon nuclei forming an excited ^{24}Mg nucleus, that decays in a variety of different products, the most commong being ^{20}Ne, ^{23}Na, ^{23}Mg. Other isotopes form in minor abundances via other reaction channels. Neutrinos coming

from pair production start to be a source of energy loss during this burning phase, with the effect of accelerating the burning rate and decreasing the duration of the burning phase.
While carbon fusion is ongoing near the degenerate core, the high temperature allows helium and hydrogen to burn in shells outside the core.

Neon burning

The burning of carbon builds up a oxygen-neon-magnesium core. Its contraction causes temperature and density to increase up to the photodisintegration of neon, at a temperature of $\sim 1.2 \times 10^9$ K. The α particles liberated in this process are captured by ^{20}Ne, producing ^{24}Mg and ^{28}Si.

Oxygen burning

Oxygen burning takes places at temperatures $\sim 1.5 \times 10^9$ K and densities $\sim 10^7$ g cm^{-3}. Fusion of two ^{16}O produces excited ^{32}S, which decays into ^{28}Si and ^{31}P. The stars consume its oxygen in period of six months to one year, when the oxygen burning moves to the shell while silicon burning begins in the core.

Silicon burning

Silicon burning is the final stage of fusion for massive stars, and it starts when the core temperature is $\gtrsim 3 \times 10^9$ K. Fusion via ^{28}Si + ^{28}Si is suppressed by its high Coulomb barrier, so the fusion proceeds via capture of α particles resulting from photodisintegration. When the temperature is $\geq 4 \times 10^9$ K, all the nuclei are in equilibrium via strong and electromagnetic interactions, called nuclear-statistical equilibrium. At this stage, fusion products converge towards the nucleus with the highest binding energy, ^{56}Ni.

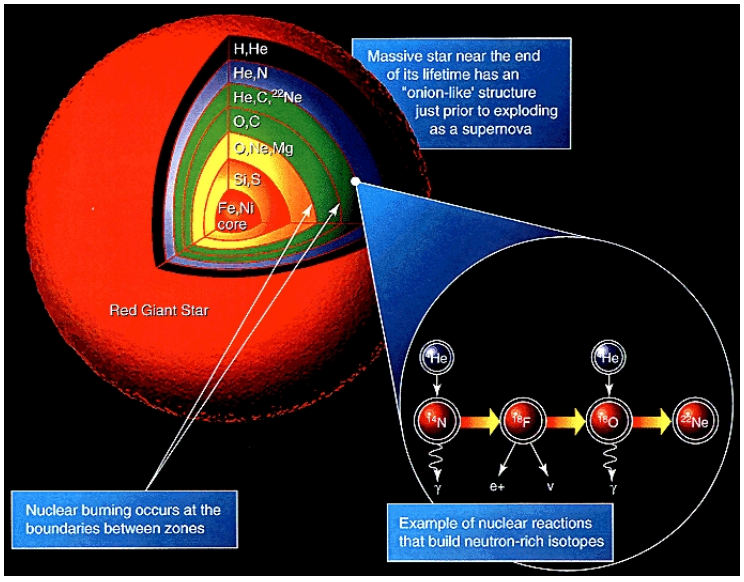

Figure 1.3: Schematic cross section of a massive star near the end of its life. The reaction $^{14}N(\alpha,\gamma)^{18}F(e^+\nu_e)^{18}O(\alpha,\gamma)^{22}Ne$ happens during the Helium burning phase and forms ^{22}Ne, a main neutron source for the s process. (Wikimedia commons)

^{56}Ni is unstable, with an half life of 6.02 days, but the star finishes its fuel before nichel has enough time to decay, and begins to contract. Since no more energy can be

generated by fusion, the contraction accelerates, leading to the collapse of the star and the formation of a supernova.

1.1.2 Supernovae

A supernova (SN) is a catastrophic stellar explosion that emits a substantial fraction of the luminosity of a typical galaxy. They play a fundamental role in the chemical evolution of galaxies, since they produce the bulk of the heavy elements and then disperse them in the interstellar medium. Feedback from supernovae explosion is a trigger for the formation of new stars in a galaxy, causing the collapse of molecular clouds.
The classification scheme for SNe is based on their spectra near maximum light and does not necessary reflect the underlying physics of the explosion or the progenitor type, as shown in Figure 1.4.

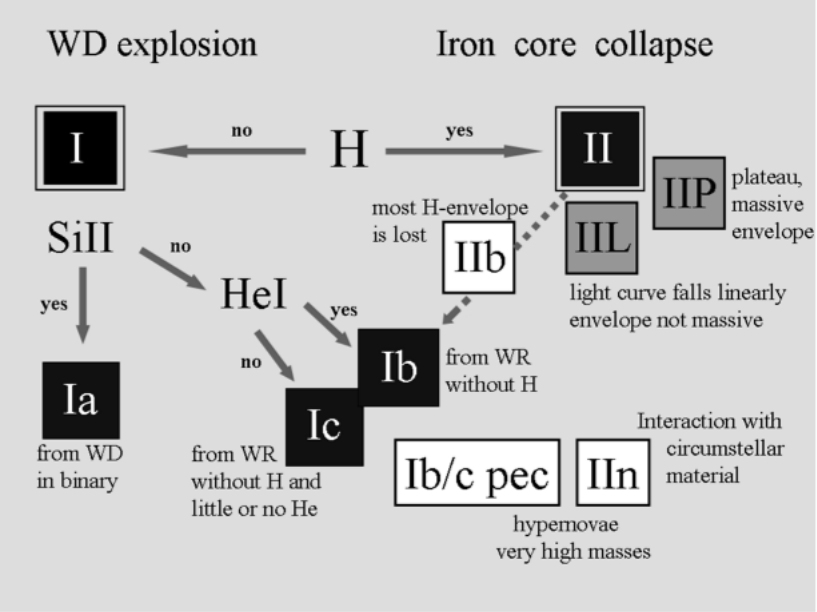

Figure 1.4: Supernova classification from Maeder (2009).

The first, coarse distinction is whether hydrogen lines are present in the SN spectrum or not. In the first case, the supernova is called of type II, in the second of type I.
Type I SNe are further classified in type Ia, which have silicon lines in their spectra, and type Ib and Ic, which have no silicon but helium lines (type Ib) or no silicon nor helium (type Ic). Type II SNe are further classified by the shape of their light curve, while light curves of SN type Ia are very similar. Type II-L (i.e. linear) show a behaviour similar to type Ia, Type II-P (i.e plateau) stay within one order of magnitude of maximum brightness for many days before fading. Type II SNe are thought to be the result of the core collapse of massive stars, with a mass ≥ 8 $M_{\odot}$.

1.1.3 Core collapse supernovae

After silicon burning is over, the massive star has a central core composed mainly of iron, with a shell like structure above, composed of oxygen, carbon, helium and hydrogen shells (see Figure 1.3).
Stars with smaller initial mass (8-10 $M_{\odot}$) have a degenerate O/Ne/Mg core that undergoes a gravitational collapse caused by electron capture by magnesium, followed by explosive

oxygen fusion which lead to a SN.
In more massive stars, the iron core reaches the Chandrasekhar mass, defined as

$$M_{ch} = 1.44 \left(\frac{Y_e}{0.5} \right)^2 M_\odot, \tag{1.2}$$

where Y_e is the electron fraction and $M_\odot$ is the mass of the Sun. At this mass, the electron degeneracy pressure can no longer stabilize the core via a temperature increase, and the core contraction does not stop.
As the core collapses, the chemistry is under nuclear statistical equilibrium due to the very high temperature, and the composition is determined only by density, temperature and electron fraction. High temperatures favour small nuclei, and iron nuclei are photo-disintegrated into helium and free neutrons. The increasing density favours instead the formation of neutrons from electrons and protons, with emission of energetic neutrinos that carry away energy and accelerate the collapse. When the core density approaches nuclear density ($\sim 2.6 \times 10^{14}$ g cm^{-3}) the short range nuclear force has a repulsive effect that stops the collapse and makes the infalling material bounce back. This bounce forms the shock wave that moves outward and initiated the explosion.

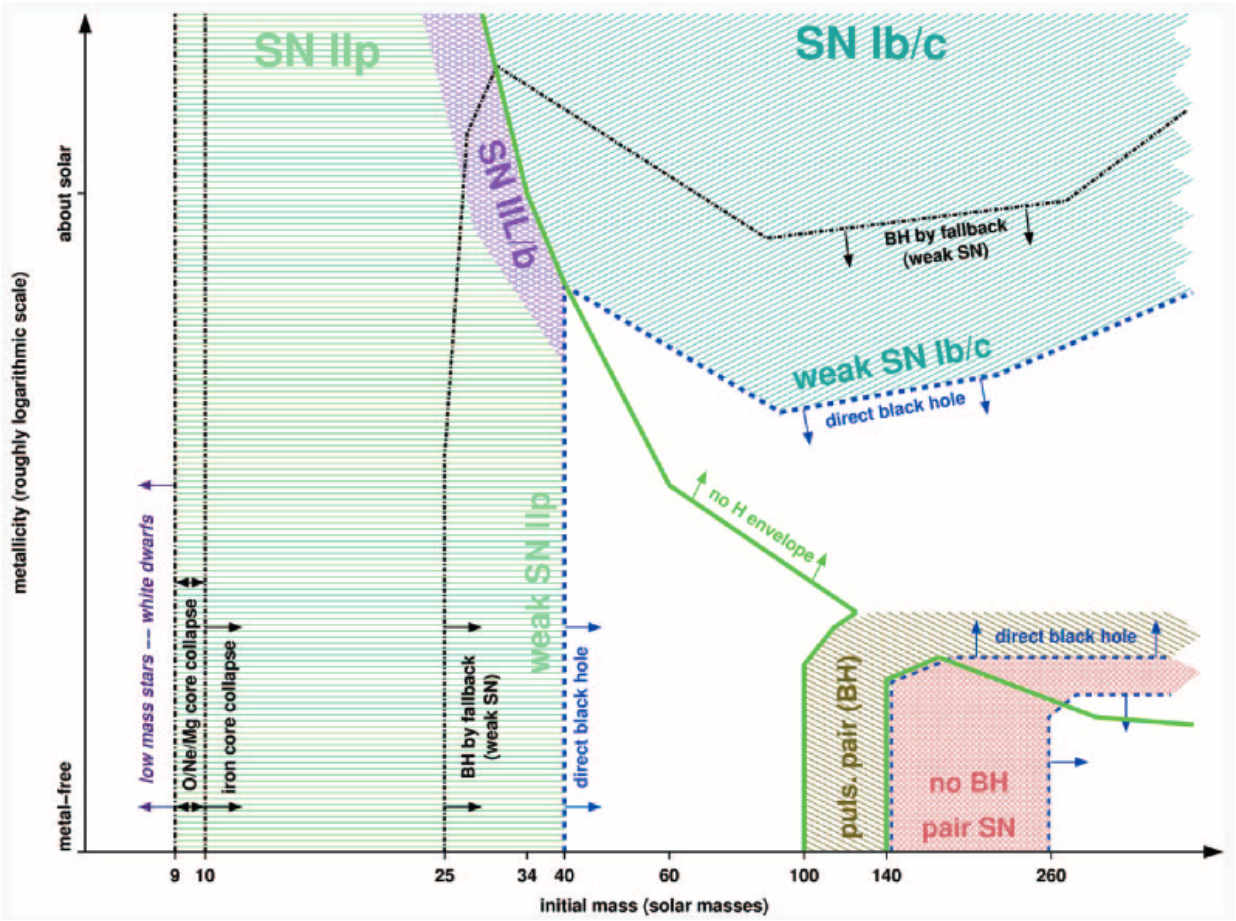

Figure 1.5: Supernova types, remnants and cause of collapse as a function of the initial mass and initial metallicity. (Heger et al., 2003)

The shock is slowed down by the still infalling material from the outer core, loses energy and stalls at $\sim$ 100 km from the core. The physical mechanism that revives the

shock is most probably energy deposition from escaping neutrinos. This delayed explosion mechanism permits the shock to expand outwards again and to break through the surface of star in a period that goes from hours to days, depending on the stellar radius.

Figure 1.5 shows the different possible Type II SNe as a function of their initial mass and metallicity, and gives information on their collapse mechanism and remnants. The thick green line separates stars with hydrogen envelope (left and lower right) from those who lost it (upper right and bottom). The dashed blue line delimits the region of direct black hole formation after the explosion, apart from the small area at the bottom labelled "no BH pair SN" which denotes pair instability supernovae that leave no remnant behind. Type II-P supernovae form in the green horizontal hatching region between 9 and $\sim$ 40 $M_\odot$. They may be faint Type II-P, with a mass range 8-25 $M_\odot$, and leave a neutron star as remnant, or standard Type II-P, with a mass of 25-40 $M_\odot$ and low or solar metallicity. In this last case the remnant is a black hole caused by the fallback of the star material into the neutron star.
If the metallicity is higher than solar, for the initial mass range of 20-40 $M_\odot$ the SN is of Type II-L or II-b, with a small hydrogen envelope and a neutron star as a remnant. For higher masses, the remnant, when present, is always a black hole.
The cause of collapse is also different in the different regions, as outlied but the dotted-dashed black lines: below 10 $M_\odot$ the collapse is caused by electron capture in the degenerate core, from 10 to $\sim$ 140 $M_\odot$ by the collapse of the iron core after reaching the Chandrasekhar mass , from 140 to 250 $M_\odot$ by pair instability, and from 250 $M_\odot$ on by photodisintegration.

1.2 Supernova Remnants

After the explosion the ejected material (ejecta) travels at some 10^4 km s^{-1} and the energy liberated is of the order of 10^{51} ergs.
The supernova remnant (SNR) goes through three phases while interacting with the interstellar medium (ISM), as shown in Figure 1.6, before gradually merge into the interstellar medium when the speed of the ejecta becomes comparable to the sound speed of the ISM, about 10^5 years after explosion.

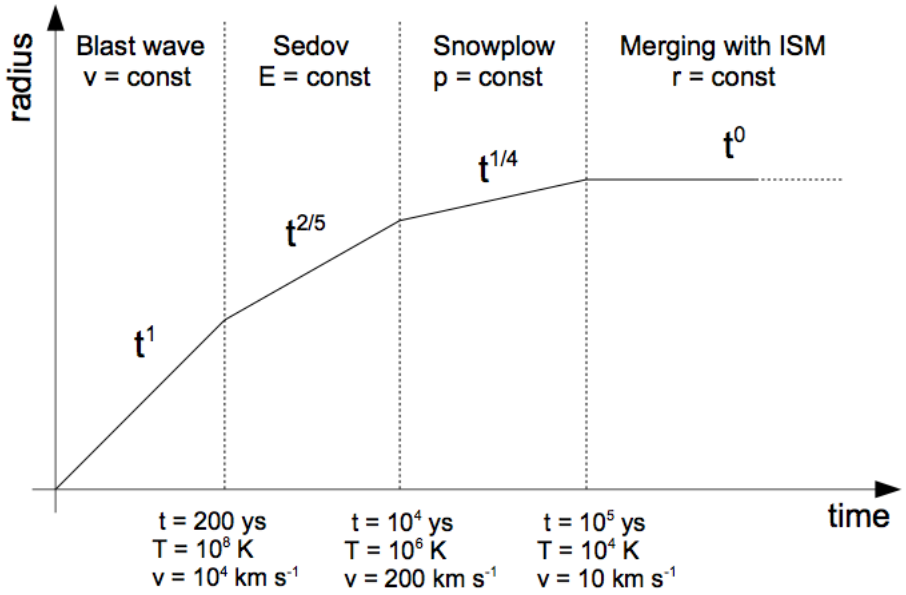

Figure 1.6: Schematic representation of the various phases of a supernova remnant, with times (t), temperatures (T) and velocities (v). Adapted from Rosswog (2007)

Blast wave phase

During the first stage the ISM has little impact on the evolution of the SNR, since the mass swept up by the forward shock is too small, and the velocity of the ejecta does not change. This phase ends when the mass swept up by the forward shock is roughly equal to the ejected mass, M_{ej}. The radius of the SNR at the end of the first phase is then

$$R_{SNR} \sim \left(\frac{3M_{ej}}{4\pi\rho_{ISM}} \right)^{1/3}, \tag{1.3}$$

where ρ_{ISM} is the density of the ISM. For an ejecta mass $M_{ej} = 1$ M$_\odot$, an explosion energy $E_{sn} = 10^{51}$ ergs and a velocity $v_{SNR} = 10^4$ km s^{-1}, the radius is $R_{SNR} = 2.4$ pc at the end of the blast wave phase, 240 years post explosion.
As the shock sweeps up material and decelerates, the sudden deceleration of the inner ejecta develops a reverse shock, that travels inward towards the center of the SNR.

Sedov-Taylor phase

In the second phase the ejecta expands because of its high pressure, but the gas in the SNR is unable to cool owing to the almost complete gas ionization brought by the high

temperatures in the remnant ($\sim 10^6$ K). The expansion slows down due to the increasing swept up mass, but the energy is conserved. By imposing the conservation of energy it is possible to write expressions for the radius as a function of time

$$R_{SNR}(t) = \left(\frac{\xi E_{sn}}{\rho_{ISM}}\right)^{1/5} t^{2/5}, \tag{1.4}$$

and the velocity as a function of time

$$v_{SNR}(t) = \frac{2}{5}\left(\frac{\xi E_{sn}}{\rho_{ISM}}\right)^{1/5} t^{-3/5}, \tag{1.5}$$

where t is the post explosion time and ξ is defined as

$$\xi = \frac{75}{8\pi}\left(\phi_k + \frac{4}{(\gamma^2-1)}\phi_i\right)^{-1}, \tag{1.6}$$

where γ is the adiabatic index, ϕ_i is the average pressure of the gas in units of the postshock pressure, and ϕ_k is the average kinetic energy in units of $M_{ej}v_{SNR}$.
These equations show that the evolution of the SNR depends only by the total energy of the explosion and the density of the ISM, and by the constants ϕ_i and ϕ_k. These latter two parameters depend on the velocity and pressure distribution of the shocked gas inside the remnant. For an homogeneous ISM and an adiabatic index of 5/3, the value of ϕ_k is 0.417 and of ϕ_i is 0.470 (Tielens, 2005).

Snowplow phase

When the shock slows down to less than 250 km s^{-1} and the gas temperature to less than 10^6 K, radiative cooling becomes important. The SNR continues its expansion due to the overpressure with respect to the ISM, but energy is radiated away, allowing the formation of a dense shell of shocked gas just after the forward shock. In this pressure-driven phase, the evolution is governed by the conservation of momentum, that gives the following scaling for the radius

$$R_{SNR}(t) = 21.6\left(\frac{E_{sn}}{10^{51}erg}\right)^{11/45} n_H^{-11/45}\left(\frac{t}{t_0}\right)^{2/7}, \tag{1.7}$$

where R_{SNR} is the radius in pc, n_H is the number density of hydrogen and t_0 is the normalization time in years, given by

$$t_0 = 2.4\times 10^4\left(\frac{E_{sn}}{10^{51}}\right)^{11/45} n_H^{-11/45}. \tag{1.8}$$

This radius correspond to a mass

$$M(t) = M_0\left(\frac{t}{t_0}\right)^{6/7}, \tag{1.9}$$

where $M(t)$ is in $M_\odot$ and M_0 is the mass in $M_\odot$ at the end of the previous phase of the SNR. The velocity is

$$v_{SNR}(t) = 250\left(\frac{t}{t_0}\right)^{-5/7}, \tag{1.10}$$

in km s^{-1}.
This phase ends when the shock wave velocity drops to the ambient sound speed of 12 km s^{-1}, corresponding to a time in years

$$t = 1.7 \times 10^6 E_{sn}^{11/45} n_H^{-11/45}, \tag{1.11}$$

when the remnant gradually merges with the ISM and disappears.

1.3 Cosmic dust

Dust consists of particles that range in size from a few molecules to a few microns, and it is an important component of the interstellar medium (ISM). Dust in the ISM provide opacity, locks up heavy elements, provides a surface for further accretion of elements and molecules. Its presence was first recognized by indirect detection, via the reddening of light from distant stars. Comparing the absorption of light at different frequencies can provide information on the nature of the absorbing dust. Dust is also an efficient scatterer of light, and elongated dust grains can influence starlight polarization.
A number of different dust grains components have been identified in the ISM.
Silicates are generally associated with absorption features at 9.7 and 18 μm, attributed to the Si-O streching and bending modes. The silicates composition is of the kind $(Mg,Fe)_2SiO_4$ and they have an abundance of 5.2 $\times$ 10^{-5} per hydrogen atom.
Graphite has been deduced from the strong 2175 Å feature in the observed interstellar extinction curve, associated with a strong graphite resonance. The required abundance of carbon in form of graphite is 7.2 $\times$ 10^{-4} per hydrogen atom.
Diamond is found in the spectra of two Herbig AeBe starts that exhibits emission bands at 3.4 and 3.5 μm, which are fitted by laboratory measured diamond bands. Observation of diamond grains in the ISM is difficult due to their lack of vibrations in the infrared.
Carbides are deduced from the 11.3 μm emission feature observed in many C-rich AGB stars, but not in the ISM. This requires a limit on the abundance of SiC grains of $\sim$ 6 $\times$ 10^{-3} with respect to hydrogen. The main characteristics of prominent dust species are outlined in Table 1.1.

Finally, individual grains can be extracted from carbonaceous meteorites. These grains, called presolar grains, formed in stellar outflows and in stellar explosions and survived the formation of the solar system. Once isolated, the isotopic ratios of measured elements present anomalies with respect to the ratios present in the solar system, pointing to a presolar origin. Such anomalies are also used to infer the origin of the grain, and are to date a reliable indication of the main dust sources in the galaxy. For example, silicon carbide grains are classified according to their peculiar anomalies and formation site as: mainstream, C, Y, AB, X or Z grains. Mainstream grains have carbon and nitrogen isotopic composition that are in agreement with an AGB origin. They comprise roughly 90 % of all silicon carbide grains, indicating a favoured AGB origin. Grains classified as C, Y and AB also come from low mass AGB or post AGB stars with low metallicity, and are $\sim$ 6 % of the total. X grains are roughly 1 % ot the total, and their isotopic carbon and nitrogen ratios show signature of helium burning, indicating a SN origin. They also have calcium excess, coming from the decay of ^{44}Ti, an element produced only in SNe explosions (Timmes et al., 1996).
Graphite grains are divided in low density (LD, 1.6 - 1.92 g cm^{-3}) and high density (HD, 2.10 - 2.20 g cm^{-3}). LD grains are similar to SiC X grains and have SN origin, while HD grains originated from low-metallicity AGB stars. Oxide and silicates grains are divided

Family	Name	Formula	Prominent bands	Reference
		Oxides		
Silicates	Pyroxene	[Mg,Fe]SiO_3	10-20	1
	Enstatite	$MgSiO_3$	9-12, 15.4, 19.5, 36.2	2
	Ferrosilite	$FeSiO_3$	11.3, 20.4, 31.7	2
	Olivine	$[Mg,Fe]_2SiO_4$	10, 20	1
	Forsterite	Mg_2SiO_4	10-20, 16.3, 19.5-24	3
	Fayalite	Fe_2SiO_4	10-12, 16.3, 19.5-24	4
Quartz	Silica	SiO_2	9.1, 12.6, 20.4-21.2-26.1	5
Metal oxides	Alumina	Al_2O_3	13	6
	Spinel	$MgAl_2O_4$	13, 16.8, 32	7
	Magnesia	MgO	19	8
	Wuestite	FeO	23.4	8
	Hematite	Fe_2O_3	9.2, 18, 20, 21	9
	Magnetite	Fe_3O_4	17,25	9
	Calcium oxide	CaO	31.4	10
	Calcite	$CaCO_3$	6.8, 11.4, 44, 92	11
	Dolomite	$CaMg[CO_3]_2$	6.6, 11.3, 60-62	11
		Carbon		
	Amorphous carbon	C	6.2, 8	12
	Graphite	C	6.3, 11.52	13
		Carbides		
	Silicon carbide	SiC	11.3	14
	Titanium carbide	TiC	20	15
		Sulphides		
	Magnesium sulphide	MgS	39	10
	Iron sulphide	FeS	34, 39	10

Table 1.1: Main characteristics of some prominent dust species. REFERENCES: (1) Dorschner et al. (1995), (2) Chihara et al. (2002), (3) Koike et al. (2003), (4) Suto et al. (2002), (5) Fabian et al. (2000), (6) Koike et al. (1995a), (7) Fabian et al. (2001), (8) Henning et al. (1995), (9) Koike et al. (1981), (10) Hofmeister et al. (2003), (11) Posch et al. (2007), (12) Colangeli et al. (1995), (13) Draine (1984), (14) Mutschke et al. (1999), (15) Koide et al. (1990).

in four groups, the first three with AGB star origin, and the fourth of SN origin, due to their oxygen excess (Zinner, 2014).
The formation mechanisms and contributions of various formation sites of the observed dust are still debated, and a further challenge is posed by the detection of large amount of dust in quasars at high redshift, which suggest a main contribution from massive stars.

1.3.1 Dust formation in massive stars

Observational evidence for dust in high redshift galaxies and quasars at $z > 6$ (Hines et al., 2006; Pei et al., 1991; Steidel et al., 1994) rises the question of dust formation sites at such early epochs.
The age of the universe was less than 1 Gyr, so a fast and efficient dust production mechanism is needed to account for the inferred dust masses of over 10^8 $M_\odot$. If star formation started at redshift 10-50, then the maximum time available to form the observed dust masses is of $\sim$ 500 Myr.
In the local universe, AGB stars are the primary source of dust (Gehrz, 1989; Sedlmayr, 1994), which is injected into the ISM during intense mass loss in the late stages of AGB stellar evolution. The composition of dust depends on the C/O ratio in the photosphere of the star: stars with $C/O < 1$ form silicates and metal oxides in their oxygen rich environment, while for $C/O > 1$ formation of hydrocarbon molecules and carbonaceous dust is favoured. Other sources of dust are high-mass stars that go through a red supergiant phase, during which they have strong stellar winds similar to those of AGB stars. Luminous blue variables (LBVs) also produce some dust. They are massive evolved stars with unstable spectra and brightness, due to irregular giant eruptions that increase mass loss and luminosity. Dust production in SNe Type II is based on observations and on the analysis of presolar grains, but their dust production rate is still unknown. There are no observations of significant amount of dust in SNe Type Ic, Ib, or Ia (Borkowski et al., 2006), with the exception of Kepler SNR (see Table 1.3). In the early universe, massive stars are strongly favoured, due to their shorter lives with respect to AGB star and to the SN origin of high redshift dust derived from extinction curves. However, the efficiency of dust formation in SN is debated, with uncertainties in both observations and theoretical models.

Observations

Warm dust emits in the near-infrared and mid-infrared, while cold dust emits in the far-infrared or sub-millimetre range. Observations are difficult because cold dust can easily be confused with cold foreground material, and it is impossible to infer the structure and the spatial distribution of grains within the ejecta. Observation are thus model-dependent, and suffer from several uncertainties, most notably the choice of dust species, the optical constants and the grain size distribution. Further uncertainties arise from the choice of SN ejecta physics and the assumption of uniform dust and gas distribution.
The presence of dust in SN ejecta is inferred by the attenuation of broad and intermediate spectral emission lines, and thermal emission from dust is detected as an IR excess, due to its heating in the hot shocked gas. It is difficult to differentiate between newly formed and pre-existing dust in the circumstellar medium.
Only ten SNe and five SNRs have observational evidence for dust (Tables 1.2 and 1.3).

The first evidence of dust from a Type IIP SN comes from SN1987A in the Large Magellanic Cloud (Wooden et al., 1993). The formation of dust is indicated by a drop in the visual light output around 530 days (Lucy et al., 1989; Whitelock et al., 1989), by a

SN	Type	Progenitor	M_p ($M_\odot$)	t (d)	M_d ($M_\odot$)	T_d (K)	Reference
2007od	IIP	SAGB	9.7-11	300	1.7-1.9$\times10^{-4}$	490-600	1,2
2007it	IIP	—	16-27	351	1.6-7.3$\times10^{-4}$	500	3
				561-718	7.0-8.0$\times10^{-5}$	590-700	3
2006jc	Ibn	LBV	40	200	6.9×10^{-5}	800	4,5
				230	3×10^{-4}	950	6
2005af	IIP	—	—	214	4×10^{-4}	—	4,7
2004et	IIP	RSG	9	300-464	3.9-6.6 $\times10^{-5}$	650-900	4,8,9
				795	1.5 $\times10^{-4}$	450	8
2004dj	IIP	RSG	12-20	267-859	0.3-3.3 $\times10^{-5}$	186-710	10-15
				849-1393	0.1-7.6$\times10^{-4}$	120-530	10,15
2003gd	IIP	RSG	8	499	2.0-17$\times10^{-4}$	480	4,16
				678	2.7-20$\times10^{-3}$	—	16
1999em	IIP	RSG	15	510	$\sim 10^{-4}$	510	4,18
1998S	IIn	—	—	360	2×10^{-3}	1250	4,19
1987A	IIP	BSG	20	615	3.7-31 $\times10^{-5}$	422	4,20
				775	5.9-50$\times10^{-5}$	307	20
				615-755	2-13 $\times10^{-4}$	—	21
				1144-6067	1-20$\times10^{-4}$	90-100	22,23
				8467,8564	0.4-0.7	17-23	24
				8865	> 0.2	26	25

Table 1.2: Observed and derived properties of SNe. M_p is the progenitor mass, t is the post-explosion time, M_d is the dust mass and T_d is the dust temperature. REFERENCES: (1) Inserra et al. (2011), (2) Andrews et al. (2010), (3) Andrews et al. (2011), (4) Smartt et al. (2009), (5) Sakon et al. (2009), (6) Mattila et al. (2008), (7) Kotak (2008), (8) Kotak et al. (2009), (9) Maguire et al. (2010), (10) Szalai et al. (2011), (11) Maíz-Apellániz et al. (2004), (12) Kotak et al. (2005), (13) Wang et al. (2005), (14) Vinkó et al. (2009), (15) Meikle et al. (2011), (16) Sugerman et al. (2006), (17) Meikle et al. (2007), (18) Elmhamdi et al. (2003), (19) Pozzo et al. (2004), (20) Wooden et al. (1993), (21) Ercolano et al. (2007), (22) Dwek et al. (1992), (23) Bouchet et al. (2004), (24) Matsuura et al. (2011), (25) Indebetouw et al. (2014). Adapted from Gall et al. (2011)

SNR	SN Type	Progenitor	M_p ($M_\odot$)	t (yr)	M_d ($M_\odot$)	T_d (K)	Reference
Cas A	IIb	WR	15-30	326	7.7 $\times10^{-5}$	170	1,2
				326	3.8×10^{-2}	52	2
				330	10^{-7}-10^{-4}	350,90	3
				330	5×10^{-6}, 10^{-5}	268,226	4
				330	3×10^{-3}	79,82	4
				330	< 1.5	—	5
				335	2-5.4$\times10^{-2}$	40-150	6
				337	~ 1	20	7
				337	6×10^{-2}	35	8
				337	7.5 $\times10^{-2}$	35	9
				340	$\lesssim 0.1$	40-100	10
Kepler	Ia / Ib	—	8	405	1-2 $\times10^{-4}$	107	11,12
				405	0.1-1.2	16,88	13
B0540	IIP	—	15-25	700-1100	1-3$\times10^{-3}$	50-65	14-16
Crab	IIP	—	8-10	950	1-7$\times10^{-2}$	45	16-19
				950	1-20 $\times10^{-3}$	50,74	19,20
1E0102	Ib / Ic	—	30	1000	1.4 $\times10^{-2}$	50-150	21-23

Table 1.3: Observed and derived properties of SNRs. M_p is the progenitor mass, t is the post-explosion time, M_d is the dust mass and T_d is the dust temperature. REFERENCES: (1) Krause et al. (2008), (2) Arendt et al. (1999), (3) Douvion et al. (2001), (4) Hines et al. (2004), (5) Wilson & Batrla (2005), (6) Rho et al. (2008), (7) Dunne et al. (2009), (8) Sibthorpe et al. (2010), (9) Barlow et al. (2010), (10) Arendt et al. (2014) (11) Blair et al. (2007), (12)Reynolds et al. (2007), (13) Gomez et al. (2009), (14) Reynolds (1985), (15) Williams et al. (2008), (16)Chevalier (2006), (17) Nomoto et al. (1982), (18) Kitaura et al. (2006), (19) Green et al. (2004), (20) Temim et al. (2006), (21) Blair et al. (2000), (22) Chevalier (2005), (23) Rho et al. (2009b). Adapted from Gall et al. (2011)

stronger IR continuum, indicating an increase in the radiation from solid particles; and from a blue shift of the optical line profiles, caused by the increase in internal extinction as the dust condenses. The last two features are shown in Figure 1.7, where the spectrum at 615 days post explosion shows increased IR continuum at a wavelenght $\sim$ 7 μm, as well as blueshift of the optical lines starting at $\sim$ 550 days post explosion.

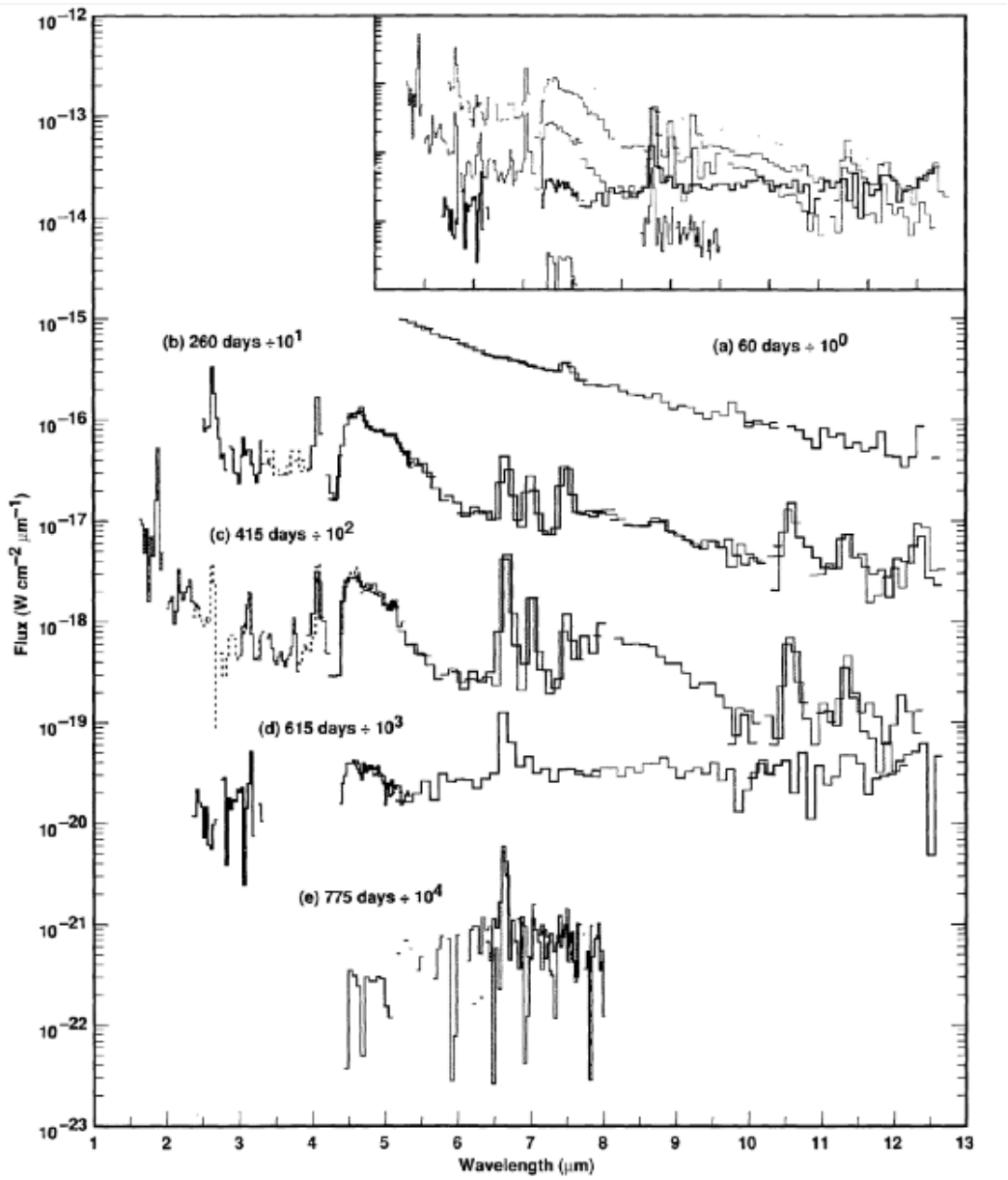

Figure 1.7: Spectrophotometry of SN1987A at 60, 260, 415, 615 and 775 days. The spectra are divided by powers of 10 in order to show the spectral features. The inset at the top shows the true flux scale, where it is clear the rise of the dust continuum at 615 days. From Wooden et al. (1993)

Figure 1.8 shows the inferred amount of dust for SNe and SNRs as a function of time and temperature. A clear trend is seen in the temperature, with higher masses of cold dust ($<$ 100 K) with respect to warm and hot dust ($>$ 100 K). Possible correlations with post-explosion time or mass of the progenitor are not clear. The inferred masses are low, with most of the SNe and SNRs exhibiting values in the range 10^{-1} - 10^{-5} $M_{\odot}$, with four objects with an higher inferred mass around 1 $M_{\odot}$.

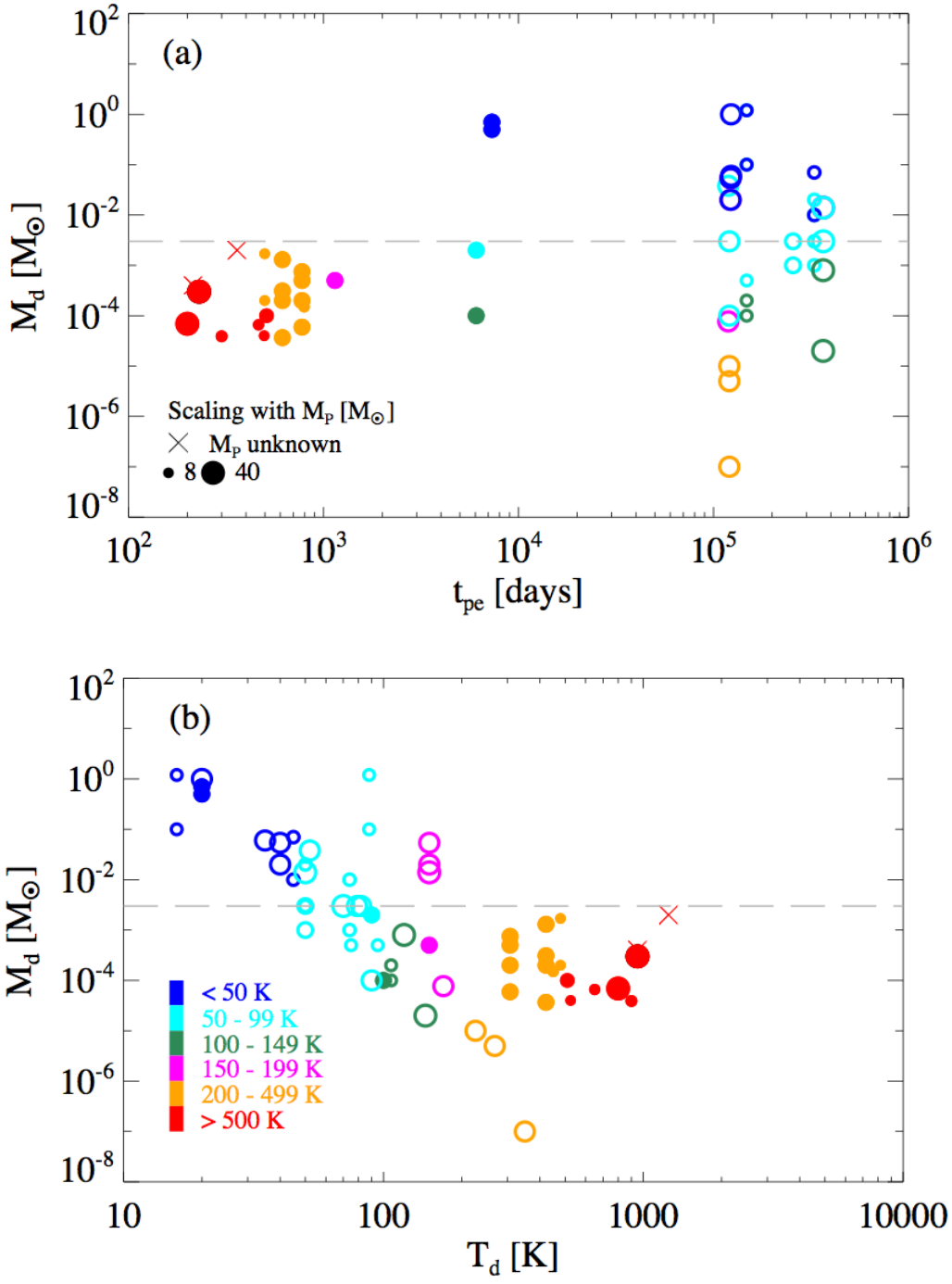

Figure 1.8: Inferred masses of dust from SN and SNR at different epochs (a) and temperatures (b). Filled circles are observation of SNe and open circles are observations of SNRs. The size of the symbols is scaled by the mass of the SN progenitor. From Gall et al. (2011)

The identification of dust type requires laboratory data of relevant solids at the appropriate temperatures in order to interpret astronomical spectra. Derived optical constants are used as input in radiative transfers calculations, as well as assumed source geometry, dust grains composition, abundance, size and shape. The most recent laboratory data cover amorphous (Dorschner et al., 1995) and crystalline silicates (Chihara et al., 2002), oxides (Henning et al., 1995), metallic iron (Ordal et al., 1988), metal sulphides (Begemann et al., 1994), amorphous carbon (Koike et al., 1995b), silicon carbide (Borghesi et al., 1986; Pegourie, 1988), titanium carbide (von Helden et al., 2000) and carbonates (Kemper et al., 2002). Several uncertainties are still present, especially in converting the optical properties in a realistic way to absorption and scattering efficiencies. This can be done exactly only for very regular shapes that are just approximation of real, irregular grain shapes, and not for all materials. Optical constants are also temperature dependent, but are often only been measured at room temperatures.

Theory

In contrast with observations, most theoretical models predict a high amount of dust in the SN ejecta in the first 600 - 1000 days (Bianchi & Schneider, 2007; Kozasa et al., 1991; Nozawa et al., 2003; Todini & Ferrara, 2001), with masses of the order of 10^{-1}-1 $M_{\odot}$. Dwek et al. (2007) calculated that at 1 $M_{\odot}$ of dust per SN is required to match the observations of high redshift quasars.
The high predicted dust masses in these models stem from the use of classical nucleation theory for the formation of dust and steady state for molecules . Classical nucleation theory considers the nucleation from the gas phase via the formation of critical clusters, and it is derived from studies of condensation of water droplets in the Earth atmosphere (Feder et al., 1966). Stoichiometric equations are used to derive dust masses, but these equations do not correspond to real chemical pathways to dust formation.
Bianchi & Schneider (2007) and Nozawa et al. (2007), consider the effect of the reverse shock crossing an homogeneous ejecta on dust grains, including sputtering processes in their calculation. The percentage of surviving grains depends on the density of the ISM, and on the type of progenitor, with 2-20 % of dust surviving. The timescales of dust destruction in these models are too long (up to 10^4 years) to explain the low mass inferred from SN observations at earlier times.
The size distribution of grains varies greatly among different studies, due to the different initial physical and chemical conditions assumed in the ejecta.
To try and reconcile models and observation, Cherchneff & Dwek (2009, 2010) use a chemical kinetic approach based on the initial chemical composition of the gas and a set of chemical reactions describing the chemistry in the ejecta. They apply this model to zero metallicity stars, leading to dust masses smaller by a factor of five and a complex chemical composition, different from the previous models. In contrast to classical nucleation theory, this approach considers the nucleation phase of dust, with chemical reactions describing the formation and growing of molecules and small dust clusters, that limit the amount of dust synthesis. This approach has been used to reconcile early and late time observations of dust mass in SN1987A (Sarangi & Cherchneff, 2013). At early times, the dust clusters mass is low, between 10^{-6} and 10^{-3} $M_{\odot}$, in agreement with mid-IR observations. The mass and the chemical complexity of clusters rise with time, with the formation of alumina, silicates and carbon, with a mass of $\sim 10^{-2}$ that is compatible with late time submm observations of SNRs that detect a larger amount of cold dust in the ejecta.

At the moment, it is still not clear if SNe are efficient dust providers and if dust grains survive the remnant phase and the reprocessing by the reverse shock. Many uncertainties remain both in the inferred mass from observations and in the ones calculated from theoretical models, where the complex physics and chemistry of the ejecta and of the remnant phase is still not completely understood.

1.4 Molecule detection in SNe and SNRs

Vibrational transitions of CO and SiO are detected in various SNe, starting some hundreds days post-explosion. In particular, the fundamental band of CO at 4.65 μm is detected in Type IIP SN 2004dj, at 89-129 days post-explosion, with a temperature $\sim$ 5500 K (Kotak et al., 2005). Both CO and SiO fundamental bands are detected in the Type IIP SN 2005af at $\sim$ 200 days post explosion, with a derived SiO mass $\sim 2 \times 10^{-4}$ $M_\odot$ (Kotak et al., 2006). Kotak et al. (2009) find a declining amount of SiO in SN2004et between 64 and 1406 days post explosion, an indication of depletion of SiO into dust.
The first detection of CO in SN1987A shows that molecule form in the ejecta as early as $\sim$ 100 days post explosion. Analysis of the spectra until 255 days post-explosion infer a CO mass of $\sim 5 \times 10^{-5}$ $M_\odot$ (Spyromilio et al., 1988). Roche et al. (1991) detect SiO in SN1987A at $\sim$ 500 days post explosion, with a mass of $4 \pm 2 \times 10^6$ $M_\odot$. Recently, Kamenetzky et al. (2013) detected rotational transitions of cold CO and SiO in the ejecta of SN1987A. The lines are emitted by at least 0.01 $M_\odot$ of cold CO at a temperature $>$ 14 K. The emitting CO is expected to be enclosed into C/O rich clumps in the central part of the SNR. Other CO first overtone detection in near infrared include SN 1995ad (Spyromilio & Leibundgut, 1996), SN 1998S (Fassia et al., 2001), SN 1999dl, SN1999em (Spyromilio et al., 2001), SN1999gi and SN 2000 ew (Gerardy et al., 2002). Rho et al. (2012) detect the fundamental band of carbon monoxide in Cas A with *AKARI* in four positions in the remnant. The derived temperature is between 900 and 2500 K, and the CO mass is between 2.4 and 6×10^{-5} $M_\odot$.
Molecule observation in SNe, starting a hundred days post explosion, and in SNRs as late as $\sim$ 330 years post-explosion is evidence of active chemistry and efficient molecule formation.

1.5 Cassiopeia A

Cassiopeia A (Cas A) is a SRN in the constellation of Cassiopeia, observed in a wide range of wavelengths, from radio waves to gamma rays. It is the remnant of a SN that exploded in the year 1681 $\pm$ 19, as viewed from Earth (Fesen et al., 2006), at a distance of $3.4\ ^{+0.3}_{-0.1}$ kpc (Reed et al., 1995).

Krause et al. (2008) study Cas A light echoes due to scattering, absorption and re-emission of the SN light by the dust in the remnant. The echo spectrum shows the presence of the hydrogen line, which classifies Cas A as a Type II SN. The additional presence of weak helium lines is typical of SNe Type IIb, which originate from massive stars that have lost most or all of their hydrogen envelope. Comparison of Cas A spectrum with the spectrum of IIb SN 1993J (Matheson et al., 2000) shows similarities in spectral features and their strength. SN 1993J is the result of the collapse of a red supergiant with a main sequence mass between 13 and 20 $M_\odot$ (Nomoto et al., 1993). The similarities between the two objects suggest that Cas A is the remnant of a red supergiant with a mass of 15-25 $M_\odot$ that exploded as a SN Type IIb.

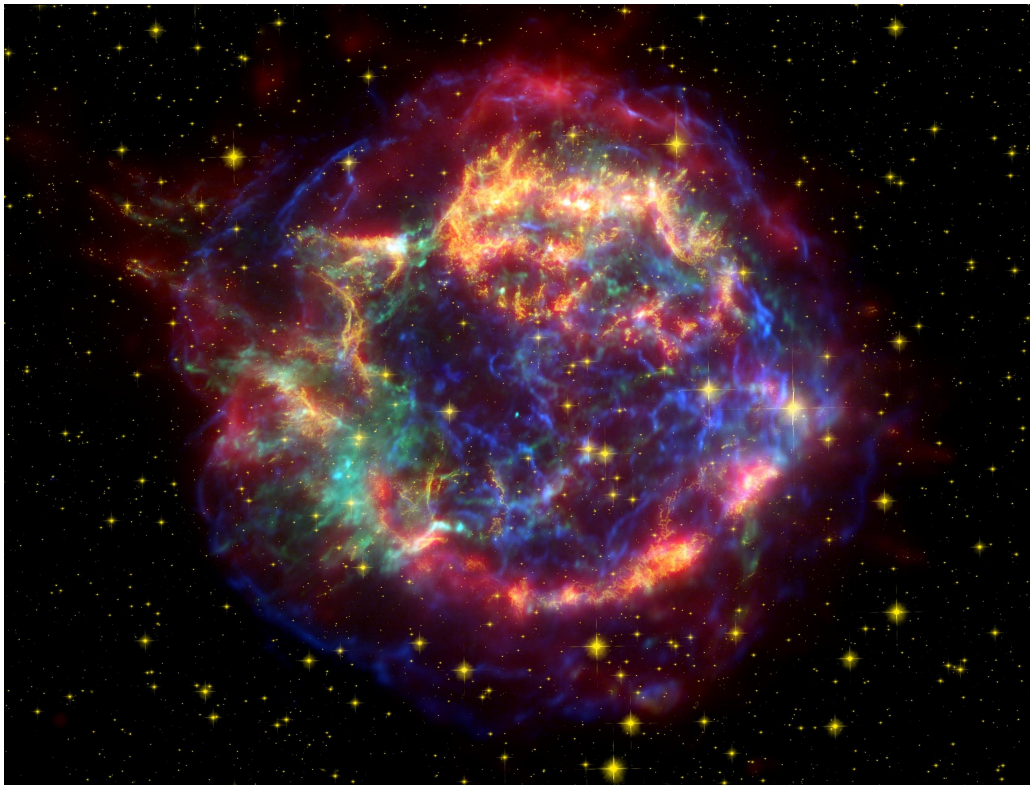

Figure 1.9: Composite image of Cassiopeia A in false colors. Infrared data from *Spitzer* are in red, optical data from *Hubble* in orange and data in the X band from *Chandra* in blue and green. NASA/JPL-Caltech

1.5.1 Cas A three dimensional structure

Cas A brightest emission is concentrated in the 200" Bright Ring where the ejecta is heated and compressed by the reverse shock (Patnaude & Fesen, 2007). The forward shock is visible in the X-rays and it is approximately 300" in diameter (Gotthelf et al., 2001). In addition to these mostly symmetrical structures, jets of silicon and solfur rich ejecta are observed in the northeast and southwest of the remnant (called Jet and Counterjet, respectively), beyond the forward shock radius (Hwang et al., 2004). DeLaney et al. (2010) study the three dimensional structure of Cas A with a Doppler analysis of the ejecta using infrared data from from the *Spitzer Space Telescope* and X-ray data from *Chandra*. This study uses Doppler velocities and sky positions of the data to reconstruct their three dimensional positions, assuming a spherical shell geometry.

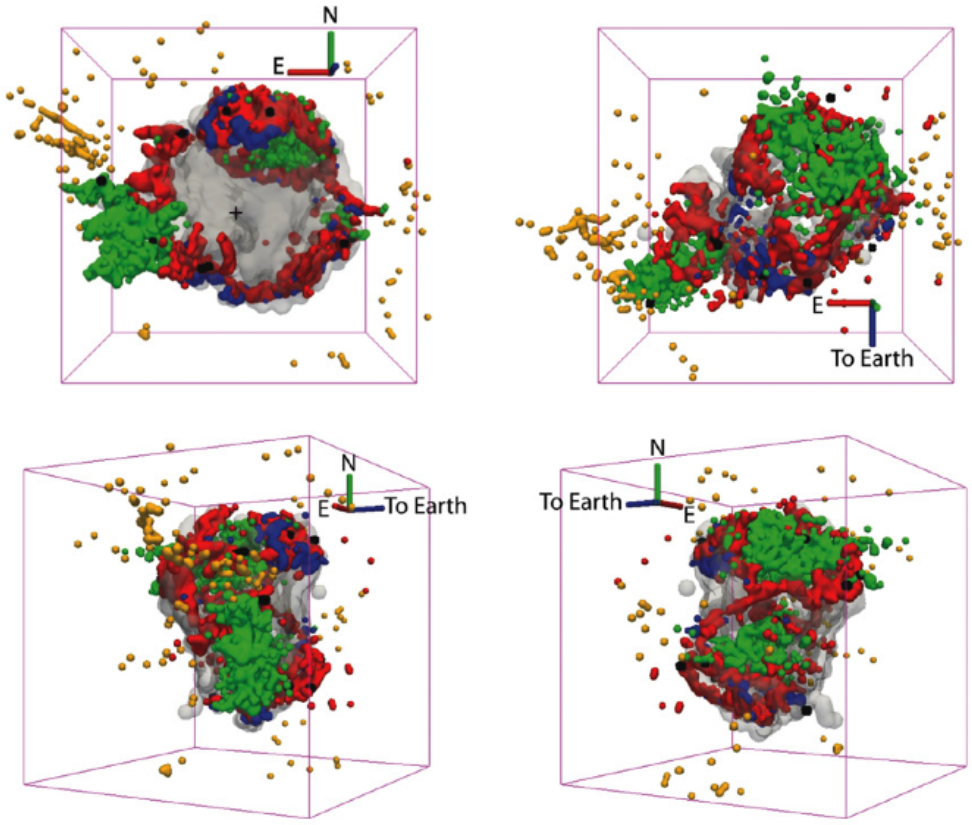

Figure 1.10: Three dimensional projection of [Ar II] (red), [Ne II]/[Ar II] (blue), [Si II] (gray), Fe-K (green) and Si XIII (black) emission, and outer optical knots (yellow). From DeLaney et al. (2010)

In Figure 1.10, [Ar II], [NeII] and Si XIII emissions are organized as rings on the surface of the sphere that defines the reverse shock. In the northeast and the west they are instead extended to larger radii, presumably due to a distortion of the reverse shock in these locations. Fe-K emission is localized in the west, the north and the southeast, where it forms a jet-like structure that extends outwards of the reverse shock sphere. These Fe-K region are circled by rings of [Ar II] ejecta, and distorted [Ar II] rings are also present at the base of the Jet and the Counterjet. The proposed explanation is that in all these regions the ejecta were faster than average, and have emerged as "pistons". The rings would be the intersection of the pistons with the reverse shock sphere.

These feature and emission from outer ejecta knot suggest that Cas A SN explosion was probably asymmetric, and that the ejecta are not homogeneous in density and velocity.

1.5.2 Dust detection in Cas A

Warm dust

Rho et al. (2008) map the entire Cas A remnant with *Spitzer* in the wavelength range 5.5-35 μm. Figure 1.11 shows a representative set of spectra.

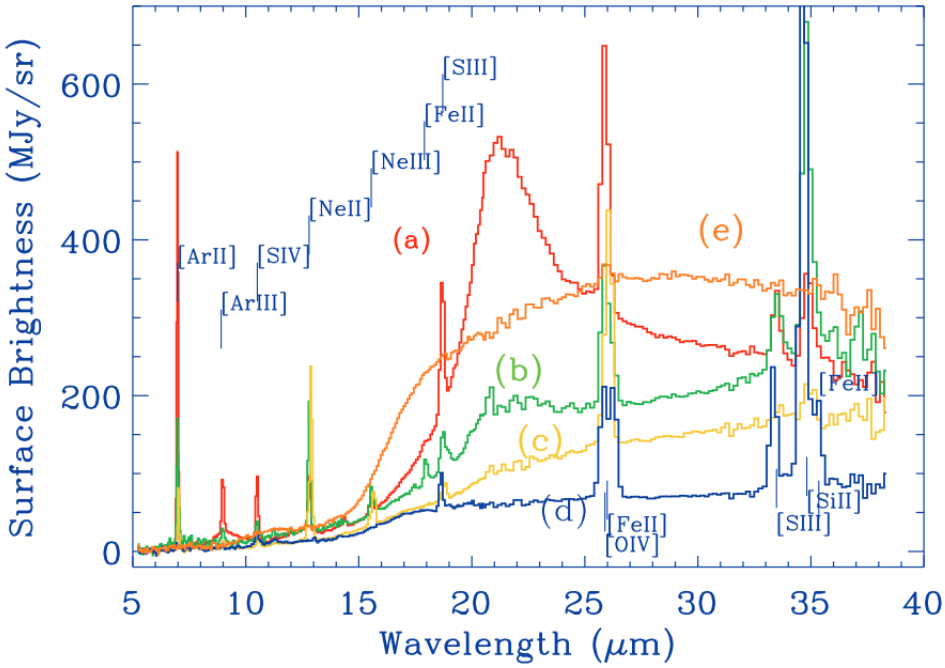

Figure 1.11: Representative set of Cas A spectra. (a) is the continuum 21 μm peak dust associated with strong Ar line, (b) is the weak 21 μm dust associated with strong Ne lines, (c) is a continuous rising featureless spectrum, (d) is the gently rising featureless spectrum and (e) is a broad continuum spectrum arising from interstellerar/cirmustellar medium. The spectra are multiplied by 1.4 (a), 2.8 (b), 0.8 (c), 1.5 (d) and 2 (e) for illustration purposes.(Rho et al., 2008)

Each dust spectrum in Figure 1.11 is separately fit with its own dust composition and temperature. The strong 21 μm peak dust (curve a in Fig. 1.11) is best fitted by Mg protosilicate, amorphous SiO_2 and FeO grains with temperatures of 60-120 K. The silicate composition suggests that the dust forms in the inner oxygen- and silicon-sulphur rich zones, consistent with the presence of a strong Ar line. Other dust types are used to fit smaller features, such as FeO, FeS, Al_2O_3, Si and Fe.
The weak 21μm (curve b in Fig. 1.11) is fitted by FeO and forsterite or Mg protosilicate. Other contributions come from carbon dust at a temperature of 80K and Al_2O_3 at a temperature of 100 K.
The featureless spectra (curves c and d in Fig. 1.11) come from a wide-spread interior 70 μm emission, likely coming from colder and still unshocked ejecta. Three possible fit are possible for this component, all of which include enstatite, FeO and Si, and either aluminium oxide, Fe, or a combination of the two to fit the longer wavelengths. A summary of the mass derived for each dust type is shown in Table 1.4.

Composition	Least massive composition	Most massive composition
Al_2O_3	8.20×10^{-4}	5.10×10^{-5}
Carbon	1.07×10^{-3}	2.08×10^{-3}
$MgSiO_3$	2.55×10^{-5}	2.55×10^{-5}
Mg_2SiO_4	3.00×10^{-6}	8.07×10^{-5}
Mg protosilicate	8.77×10^{-5}	4.67×10^{-5}
SiO_2	2.23×10^{-3}	1.40×10^{-3}
Si	8.66×10^{-3}	3.00×10^{-3}
Fe	0.00	3.14×10^{-2}
FeO	6.08×10^{-3}	1.41×10^{-2}
FeS	5.90×10^{-4}	2.15×10^{-3}
Total	0.020	0.054

Table 1.4: Sum of the masses in $M_\odot$ using the least massive dust composition among the possible fits (second column) and the most massive dust composition (third column). Adapted from Rho et al. (2008)

Cold dust

Dunne et al. (2003) detected a submm excess emission in nonthermal flux levels, attributed to a cold dust component with mass between 2 and 4 $M_\odot$ and temperature $\sim$ 15 - 20 K. Krause et al. (2004) argued that most of the detected excess is caused by foreground molecular clouds, making the initial mass estimation too high. Sibthorpe et al. (2010) use AKARI high resolution data and find evidence of a cold dust component in Cas A, with a temperature of $\sim$35 K and an estimated mass of 0.06 $M_\odot$, confined in the central area of the remnant. Barlow et al. (2010) observe Cas A with the *Herschel* Space Observatory between 70 and 500 μm.

In order to identify the cold dust component, they first subtract Cas A nonthermal emission, the warm dust component at 24 μm in the image from *Spitzer* from Hines et al. (2004) (middle top panel of Figure 1.12), and the cold intestellar dust component. Subtraction of the warm dust component from *Herschel* 70 μm image (central panel of Fig 1.12), leads to the middle-right image in Fig. 1.12, where emission from cold dust is seen in the unshocked interior of the remnant. This image is very similar to the one in the top-right panel, showing emission from cold dust at 100 μm. The cold dust emission is fitted by Barlow et al. (2010) with 0.075 ± 0.028 $M_\odot$ of silicate dust at a temperature of $\sim$ 35 K.

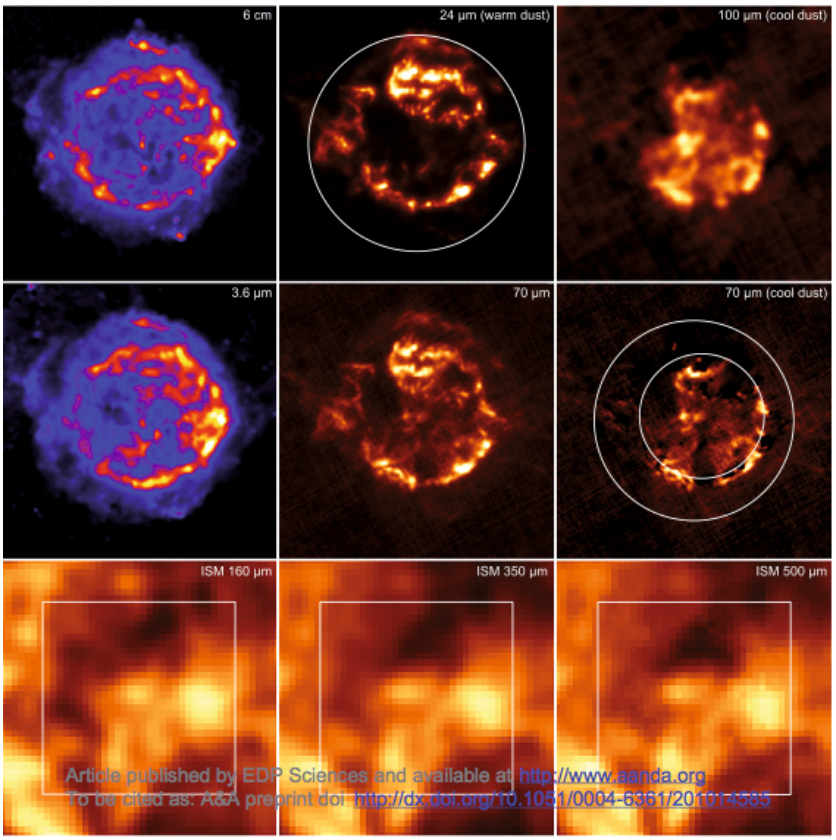

Figure 1.12: Images of Cas A at infrared, submillimiter and radio wavelengths. The top six images are 7' on a side, while the lower three images are 10' on a side, with inset boxes showing the 7' field. (Barlow et al., 2010)

1.6 This work

The aim of this work is to assess wheter Cas A and SNRs in general are feasible as dust providers in the universe, looking at molecules and dust clusters formation, and dust condensation in the ejecta. We also want to investigate the effect of the remnant reverse shock on dust in clumps, and after the clump disruption.
Section 2 introduces the physical and chemical models of the ejecta of Cas A progenitor, outlines the chemical kinetic method and its use in Cas A progenitor case. Results in this section regard molecules and dust clusters mass, and the role of density on chemical reactions in the gas phase and on chemical complexity. At the end of the section, dust condensation is considered, and dust size distributions are calculated for clumps in the ejecta. Section 3 reviews models for the reverse shock in Cas A. One dimensional models for shocks in oxygen-rich clumps are considered and used as input condition to model the gas phase chemistry in an oxygen-rich clump in Cas A. The aim is to look at molecules and dust clusters reformation in the dense postshock gas. Section 4 outlines observation of a dense knot in Cas A with the space telescope *Herschel*. Several high excitation CO lines are observed, pointing to a recently shocked dense clump in which CO is reforming. Section 5 describes the sputtering model used in this work to treat sputtering of dust in Cas A. This model is applied to the dust distributions calculated in Section 2 for oxygen-rich and carbon-rich clumps in the remnant. First dust grains are subject to non-thermal sputtering in the clump, and then to thermal sputtering in the interclump medium after the disruption of the clump caused by the reverse shock. Denser clumps present in Type IIP SNe are also considered. The aim is to assess if dust can survive in Cas A and in SNRs in general and with which radius and mass.

2. Dust formation in the Cas A supernova precursor

2.1 Physical model of the ejecta

In order to study dust formation and final dust budget in the remnant, it is first necessary to correctly assess the formation of molecules and small clusters in the ejecta, as this is the bottleneck for dust formation. We start from 100 days after the explosion, as the elements produced via nucleosynthesis during the stellar evolution of the progenitor start to assemble into molecules and dust clusters. This is supported by observations of SN1987A, which detected CO, SiO and dust formation between 100 and 500 days post explosion (Catchpole et al., 1988; Danziger et al., 1991; Wooden et al., 1993) .
SN ejecta are characterised by high gas temperatures, high velocities, and radioactivity coming from the decay of ^{56}Ni. Radioactivity is of particular importance since it powers the light curve of supernovae of type II. From observation of SN1987A between 100 and 1000 days, 0.075 $M_\odot$ of ^{56}Ni are required for reproduce the light curve (Woosley et al., 1989) . These extreme conditions lead to a chemistry that is modelled with a chemical kinetic approach, following Cherchneff & Dwek (2009). This approach starts from the gas initial chemical compositions and evolves it using a set of chemical reactions describing the chemical reactions happening in the specific physical conditions of the hot, high density ejecta of supernovae.
Cas A is a SNR resulting from the explosion of a blue super-giant of mass 15-25 $M_\odot$ as a type IIb SN (Krause et al., 2008) . We follow the model presented in Nozawa et al. (2010) for Cas A as a type IIb SN with explosion energy E = 10^{51}erg and gas velocity 4000 km s^{-1}. Their temperature, density and velocity profiles are reproduced in Fig 2.1. The temperature evolution, for a quasi-adiabatic expansion of the gas, follows:

$$T(t) = T_0 \times \left(\frac{t}{t_0}\right)^{3(1-\gamma)}, \tag{2.1}$$

where γ is an adiabatic index, t the time after the explosion and T_0 is the gas temperature at time $t_0 = 100$ days. For the case of Cas A, fitting the temperature profile with the one in Figure 2.1 gives a value $\gamma = 1.433$ and $T_0 = 6663.95$ K.
The ejecta expansion can be treated as homologous, i.e. the fractional rate of change of density is constant, since a few hours to a few days post-explosion, as the ejecta completes its acceleration to asymptotic velocity. The gas number density variation with time follows the equation

$$n(M_r, t) = n(M_r, t_0) \times \left(\frac{t}{t_0}\right)^{-3}, \tag{2.2}$$

where M_r is the mass zone position and $n(M_r, t_0)$ is the number density for a certain mass coordinate at $t = t_0$. Following Figure 2.1, we took a flat density profile across the He-core with density 5.1×10^{-15} g cm^{-3} at $t_0 = 100$ days.

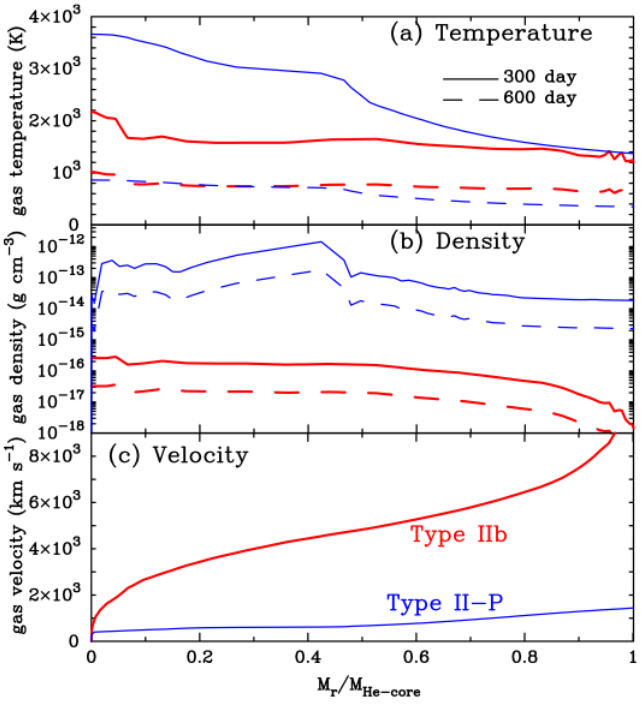

Figure 2.1: Temperature (a) and density (b) profiles of the He core gas at day 300 (solid lines) and 600 (dashed lines) post explosion, and (c) velocity distribution for the SN type IIb model (thick lines). A SN type IIP model with an ejecta mass of 17 $M_\odot$ from Umeda & Nomoto (2002) is shown for comparison. From Nozawa et al. (2010)

We consider stratified ejecta with no mixing. The initial chemical composition is taken from Rauscher et al. (2002) for a 19 $M_\odot$ progenitor with an He-core mass of 5.62 $M_\odot$, and it is showed in Figure 2.2.

2.2 Ejecta chemistry

We divide the ejecta in seven different zones, based on their peculiar chemical composition, as can be seen in Table 2.1. The mass fraction trends with respect to the mass coordinate are characterized by a plateaux, where the mass fraction of all elements are constant, followed by abrupt changes in mass fraction. We choose these regions of rapid change as the boundaries of our zones. The mass fraction we choose for each zone for each elements is thus more accurate. Each zone has its own set of species and chemical reactions appropriate for its composition. Not all elements are present in all the zones, and their mass fraction varies across several orders of magnitude. For example, helium rises fast from a mass coordinate of ~ 4 $M_\odot$ so we consider its associate chemical reactions just from this zone on. We use this composition to calculate a mean molecular weight μ_{gas} for each zone, which we use to derive the number density profile of each zone, according to the formula

$$n = \frac{\rho}{\mu_{gas}} \tag{2.3}$$

where n is the gas number density in cm^{-3}, ρ is the gas density in g cm^{-3}, and μ_{gas} is in g mol^{-1}. The ejecta temperature and number density are calculated according to equations

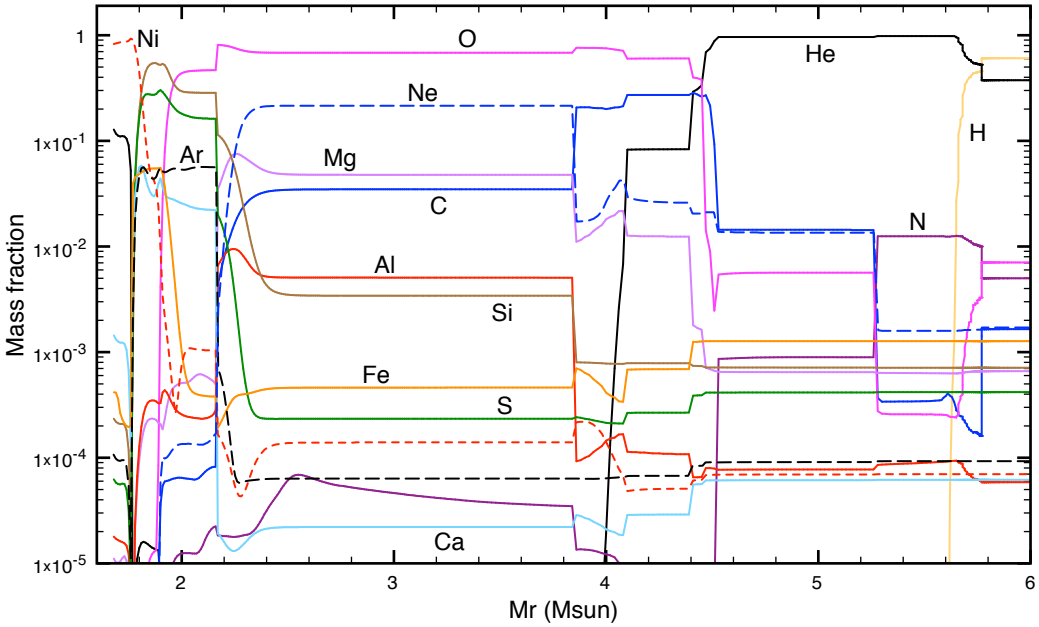

Figure 2.2: Mass fractions as a function of mass coordinate for a 19 $M_\odot$ progenitor. From Rauscher et al. (2002)

Zone	μ_{gas}	C/O	He	C	O	Ne	Mg	Al	Si	S	Ar	Fe	Ni
1a	42.3	0.08	0	1.0(-7)	1.3(-6)	6.4(-7)	1.8(-5)	2.7(-5)	3.9(-2)	2.3(-2)	4.7(-3)	5.8(-3)	1.1(-1)
1b	22.5	1(-3)	0	1.1(-4)	1.2(-1)	1.0(-4)	8.7(-4)	2.2(-4)	9.8(-2)	5.6(-2)	1.5(-2)	2.7(-3)	6.1(-4)
2	17.0	0.049	0	5.7(-2)	1.1	3.3(-1)	8.4(-2)	9.1(-3)	1.5(-2)	1.3(-3)	1.2(-4)	7.5(-4)	2.2(-4)
3a	15.1	0.27	0	2.9(-2)	1.1(-1)	2.8(-3)	2.0(-3)	1.6(-5)	1.1(-4)	3.2(-5)	8.9(-6)	7.8(-5)	2.8(-5)
3b	10.3	0.48	7.4(-2)	1.2(-1)	2.5(-1)	1.3(-2)	5.2(-3)	5.1(-5)	3.6(-4)	1.3(-4)	3.3(-5)	3.6(-4)	2.8(-5)
4a	4.1	3.0	7.2(-1)	1.2(-2)	4.2(-3)	1.0(-2)	4.8(-4)	5.8(-5)	5.4(-4)	3.1(-4)	6.8(-5)	9.5(-4)	5.2(-5)
4b	4.0	1.4	3.3(-1)	1.2(-4)	8.8(-5)	5.4(-4)	2.1(-4)	3.0(-5)	2.4(-4)	1.4(-4)	3.2(-5)	4.3(-4)	2.4(-5)
Total Yield			1.124	0.218	1.584	0.356	9.3(-2)	9.5(-3)	0.153	8.1(-2)	2.0(-2)	1.1(-2)	0.111

Table 2.1: Gas mean molecular weight μ_{gas}, C/O ratio, and initial elemental mass yields as a function of ejecta zone for the 19 $M_\odot$ progenitor of Rauscher et al. (2002). The total yield is the elemental mass yield for the total ejected material. Mass yields are in $M_\odot$ and the gas mean molecular weight μ_{gas} is in g mol¹. Nitrogen, N, is only present in Zone 4b with a yield of 4.2×10^{-3}. (Biscaro & Cherchneff, 2014).

2.1 and 2.2 and their variation as a function of post-explosion time are given in Table 2.2.

		Zone 1a 1.68-1.88 $M_\odot$	Zone 1b 1.89-2.18 $M_\odot$	Zone 2 2.19-3.86 $M_\odot$	Zone 3a 3.87-4.02 $M_\odot$	Zone 3b 4.03-4.49 $M_\odot$	Zone 4a 4.5-5.26 $M_\odot$	Zone 4b 5.27-5.62 $M_\odot$
Time	T_{gas}	n_{gas}	n_{gas}	n_{gas}	n_{gas}	n_{gas}	n_{gas}	n_{gas}
100	6664	7.2(7)	1.4(8)	1.8(8)	2.0(8)	3.0(8)	7.2(8)	7.7(8)
200	2700	9.0(6)	1.7(7)	2.3(7)	2.5(7)	3.7(7)	9.4(7)	9.6(7)
300	1600	2.7(6)	5.0(6)	6.6(6)	7.5(6)	1.1(7)	2.8(7)	2.8(7)
400	1100	1.1(6)	2.1(6)	2.8(6)	3.2(6)	4.6(6)	1.2(7)	1.2(7)
500	820	5.8(5)	1.1(6)	1.4(6)	1.6(6)	2.3(6)	6.0(6)	6.0(6)
1000	330	7.2(4)	1.4(5)	1.8(5)	2.0(5)	3.0(5)	7.5(5)	7.8(5)
1500	200	2.2(4)	4.0(4)	5.3(4)	6.0(4)	8.8(4)	2.2(5)	2.3(5)
2000	140	9.0(3)	1.7(4)	2.3(4)	2.5(4)	3.7(4)	9.4(4)	9.6(4)
2500	100	4.6(3)	8.7(3)	1.1(4)	1.3(4)	1.9(4)	4.8(4)	4.9(4)
3000	80	2.7(3)	5.0(3)	6.6(3)	7.5(3)	1.1(4)	2.8(4)	2.8(4)

Table 2.2: Ejecta temperature T_{gas} and number density n_{gas} for the Type IIb Cas A supernova as a function of post-explosion time and ejecta zones (the mass coordinates of each zone in the He-core is given). Time is in days, T_{gas} in Kelvin and n_{gas} in cm^{-3}. (Biscaro & Cherchneff, 2014).

The temporal variation of the number density of a chemical species i, n_i, is described by the rate equation (Cherchneff & Dwek, 2009)

$$\frac{dn_i}{dt} = P_i - L_i = \sum_j k_{ji} n_j n_i - \sum_k k_{ik} n_i n_k, \tag{2.4}$$

where P_i and L_i are the production and loss processes for species i, respectively. k_{ij} is the rate for the reaction of i with j, written in the Arrhenius form:

$$k_{ij}(T) = A_{ij} \times \left(\frac{T}{300}\right)^{\nu} \times exp(-E_{ij}/T), \tag{2.5}$$

where T is the gas temperature in Kelvin, ν is an exponent that gives the temperature dependence, E_{ij} is the activation energy barrier in Kelvin. The coefficient A_{ij} has units of s^{-1}, cm^3s^{-1}, or cm^6s^{-1} for unimolecular, bimolecular or termolecular reactions, respectively.
Reaction rates are taken from the NIST, KIDA and UDFA databases, and from Cherchneff & Dwek (2009). We include thermal processes, such as the ones described in Table 2.3. We also consider non-thermal processes, due to the presence of ^{56}Ni in the ejecta.

Reaction description					Gas regime/location
THERMAL					
Unimolecular	AB	$\longrightarrow$	A + B	Thermal decomposition	Very high temperature
Bimolecular	AB+ C	$\longrightarrow$	BC + A	Neutral exchange	High temperature
	A + B	$\longrightarrow$	AB + hν	Radiative association	T independent
	AB + M	$\longrightarrow$	A + B + M	Collision dissociation	High density
	AB^+ + C	$\longrightarrow$	BC^+ + A	Ion−Molecule	T independent
	AB^+ + C	$\longrightarrow$	AB + C^+	Charge exchange	T independent
	$A^+ + e^-$	$\longrightarrow$	A + hν	Radiative recombination	T independent
	$AB^+ + e^-$	$\longrightarrow$	A + B	Dissociative recombination	T independent
Termolecular	A + B + M	$\longrightarrow$	AB + M	Three-body association	High density
NON-THERMAL					
	A + CE	$\longrightarrow$	$A^+ + e^-$ +CE	Ionisation by Compton e^-	entire SN ejecta
	AB + CE	$\longrightarrow$	A + B + CE	Dissociation by Compton e^-	entire SN ejecta

Table 2.3: Thermal and non-thermal processes and chemical reaction types included in the chemical model for both the Type IIb SN ejecta. (Biscaro & Cherchneff, 2014)

Due to its radioactivity, we have the following decay chain: ^{56}Ni $\rightarrow$ ^{56}Co $\rightarrow$ ^{56}Fe.
^{56}Ni is produced in the supernova explosive nucleosynthesis, and decays in ^{56}Co with an half life of 6 days, and in turn ^{56}Co decays into ^{56}Fe with an half life of 77 days. The γ rays coming from the radioactive decay power the light curve of the SN, and then degrade to hard X-rays and UV photons via Compton scattering. This creates fast electrons, that contribute to the ionization of the ejecta and to the destruction of molecules. Following Cherchneff & Dwek (2009) we assume that all this energy will be deposited uniformly in the ejecta, and thus the rate of energy deposition by thermalized γ rays is (from Woosley et al. (1989) for SN1987A)

$$L_\gamma = 9.54 \times 10^{41} exp(-t/\tau_{56})(1 - exp[-\tau_0(t/t_0)^{-2}]), \tag{2.6}$$

in erg s^{-1}, where τ_{56}= 111.26 d is the e-folding time of the ^{56}Co decay and τ_0 is the γ ray optical depth of the ejecta at the time t_0. This rate scales linearly with the mass of ^{56}Co, so we can rewrite the destruction rate for species i in s^{-1} in terms of the mass of ^{56}Co produced in SN1987A (Cherchneff & Dwek, 2009; Liu & Dalgarno, 1995) as

$$k_C(i) = \frac{5.95 \times 10^{53}}{W_i N_{tot}} \left(\frac{M_{56}}{M_{56}(SN1987A)} \right) exp(-t/\tau_{56})(1 - exp[-\tau_0(t/t_0)^{-2}]), \quad (2.7)$$

where $M_{56}(SN1987A)$ and M_{56} are the mass of ^{56}Co in SN1987A and in the ejecta, respectively, N_i is the total number of particles in the ejecta and W_i is the mean energy per ion-pair in eV. W_i is then the energy of the incident electron divided by the number of ionization, dissociation, excitation produced by collision until it is slowed to rest (Dalgarno et al., 1999; Liu & Dalgarno, 1994) .
The effective γ ray optical depth at time t is

$$\tau(t) \equiv \kappa_{56}\rho(t)R(t) = \kappa_{56} \times \left(\frac{3M_{He}}{4\pi r(t)^2} \right), \quad (2.8)$$

where κ_{56} is the average γ ray mass absorption coefficient in cm^{2}g^{-1}, $\rho(t)$ is the mass density of the ejecta at time t and $R(t)$ is the radius of the ejecta at the same time. We adopt a value of κ_{56} of 0.033 cm^2 g^{-1} and an average value for τ_0 of 23 for all ejecta, following Cherchneff & Dwek (2009) . We test the use of a different value for the optical depth for each different zone in the ejecta, using the values in Kozma & Fransson (1992) for a 20 $M_\odot$ progenitor, but the results calculated with this method show very little differences compared with the results using an average optical depth (Sarangi & Cherchneff, 2013).
Impacts with energetic Compton electrons lead to several different reactions, whose branching rations depend on W_i, the mean energies per ion-pair for a given species. The available values of W_i are listed in Table 2.4 for the different species considered. When no value is available, we use the same W_i of CO. To put these rates in Arrhenius form, we first

Species	Reaction	W_i (eV)	A	Reference
CO	CO → O$^+$ + C	768	5.63×10^{-7}	Liu & Dalgarno 1995
	CO → C$^+$ + O	247	1.76×10^{-6}	”
	CO → O + C	125	3.46×10^{-6}	”
	CO → CO$^+$ + e^-	34	1.27×10^{-5}	”
SiO	SiO → O$^+$ + Si	678	6.38×10^{-7}	”
	SiO → Si$^+$ + O	218	1.98×10^{-6}	”
	SiO → Si + O	110	3.93×10^{-6}	”
	SiO → SiO$^+$ + e^-	30	1.44×10^{-5}	”
N_2	N_2 → N$^+$ + N	264	1.64×10^{-6}	Khare & Kumar 1977
	N_2 → N + N	133.5	1.75×10^{-6}	”
	N_2 → N_2^+ + e^-	36.3	3.46×10^{-6}	”
O	O → O$^+$ +e^-	46.2	9.36×10^{-6}	Liu & Dalgarno 1995
C	C → C$^+$ +e^-	36.4	1.19×10^{-5}	”
He	He → He$^+$ +e^-	46.3	9.34×10^{-6}	Dalgarno et al. 1999
Ne	Ne → Ne$^+$ +e^-	36.3	1.19×10^{-5}	Sharma & Veenhof 1998
Ar	Ar → Ar$^+$ +e^-	26.0	1.66×10^{-5}	”

Table 2.4: Mean energy per ion pair for the listed elements and compton election induced reactions. The rate is in Arrhenius form: A × exp(-2732.8/T). (Biscaro & Cherchneff, 2014).

derive the rate as a function of ejecta temperature, using equations 2.1 and 2.7, and then

fit this in the range of temperatures of interest for the progenitor model (see Table 2.2). All the chemical species and dust clusters used are summarized in Table 2.5. Each one of these species contributes with one equation of the form of Eq. 2.4 to the set of coupled differential equation that we solve in our model of the gas phase chemistry.

Table 2.5: Chemical species and dust clusters included in the chemical model of the SN ejecta

Atoms								
O	Si	S	C	Mg	Al	Fe	He	Ne
N	Ar							
Ions								
O^+	Si^+	S^+	C^+	Mg^+	Al^+	Fe^+	He^+	Ne^+
Ar^+	C_2^+	SiO^+	CO^+	O_2^+	SO^+			
Molecules								
O_2	CO	SiO	SO	NO	AlO	FeO	MgO	CO_2
CN	CS	SiS	SiC	FeS	MgS	S_2	N_2	
Dust Clusters								
Si_2	Si_3	Si_4	Mg_2	Mg_3	Mg_4	Fe_2	Fe_3	Fe_4
Si_2C_2	Mg_2S_2	Fe_2S_2	Fe_3S_3	Fe_4S_4	Al_2	Fe_2O_2	Fe_3O_3	Fe_4O_4
Si_2O_2	Si_3O_3	Si_4O_4	Si_5O_5	SiO_2	Si_2O_3	Si_3O_4	Si_4O_5	
$MgSi_2O_3$	$MgSi_2O_4$	$Mg_2Si_2O_4$	$Mg_2Si_2O_5$	$Mg_2Si_2O_6$	$Mg_3Si_2O_6$	$Mg_3Si_2O_7$	$Mg_4Si_2O_7$	
$Mg_4Si_2O_8$	Mg_2O_2	Mg_3O_3	Mg_4O_4	Al_2O_2	AlO_2	Al_2O_3	Al_4O_6	
C_2	C_3	C_4	C_5	C_6	C_7	C_8	C_9	C_{10}
C_{11}	C_{12}	C_{13}	C_{14}	C_{15}	C_{16}	C_{17}	C_{18}	C_{19}
C_{20}	C_{21}	C_{22}	C_{23}	C_{24}	C_{25}	C_{26}	C_{27}	C_{28}

Since the ejecta cools quickly with time, we consider two temperature regimes: a hot regime for temperatures over 300 K, and a cold regime for temperatures lower than 300 K. When available, high temperature rates for neutral-neutral reactions are replaced with low temperature ones at 1000 days, when the temperature approaches the threshold of 300 K. Other reactions that have no temperature dependence, such as radiative processes or charge exchange reactions, are left unchanged. When no measured rates are present in the databases, we substitute the missing rates with rates available for isovalent atoms, for example using C as an isovalent substitute of Si. For nucleation of small clusters we use different approaches.
For small silica, magnesium and pure metals clusters we follow the approach described in Cherchneff & Dwek (2010). Silica grows directly from SiO to form $(SiO)_n$ clusters, via the reaction

$$\mathrm{SiO} + (\mathrm{SiO})_\mathrm{n} \longrightarrow (\mathrm{SiO})_{n+1}. \tag{2.9}$$

SiO is formed by oxidation with O_2, by reaction with CO and by radiative association:

$$\mathrm{Si} + \mathrm{O_2} \longrightarrow \mathrm{SiO} + \mathrm{O}, \tag{2.10}$$

$$\mathrm{Si} + \mathrm{CO} \longrightarrow \mathrm{SiO} + \mathrm{C}, \tag{2.11}$$

$$\mathrm{Si} + \mathrm{O} \longrightarrow \mathrm{SiO} + h\nu. \tag{2.12}$$

The rate for the formation of $(SiO)_n$ is highly pressure dependent and it is taken from Zachariah & Tsang (1993). We use the rate for a pressure of 1 atm, rescaled for the ejecta pressure using the number of collision per cm^3. The most stable structure for $(SiO)_n$ are showed in Figure 2.3. This species are rather stable, with destruction coming only from termolecular fragmentation processes (Lu et al., 2003), of the form

$$\mathrm{SiO_n} + \mathrm{M} \longrightarrow (\mathrm{SiO})_\mathrm{m} + (\mathrm{SiO})_{\mathrm{n-m}} + \mathrm{M}, \tag{2.13}$$

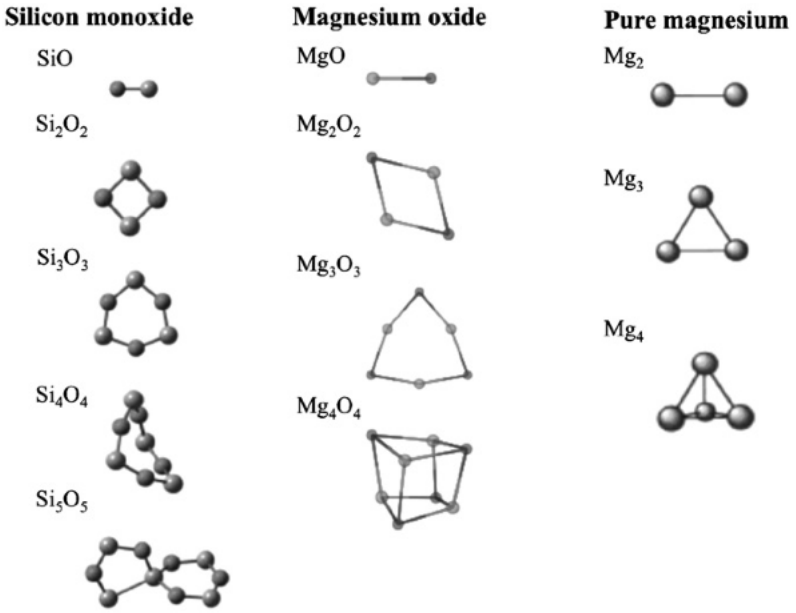

Figure 2.3: Structure of small clusters of silicon, magnesium oxide and magnesium. From Cherchneff & Dwek (2010).

where M is the ambient gas. The route for pure metal clusters starts with a termolecular formation stage, in which the metal atoms interact with the gas to form the first small clusters,

$$\mathrm{Fe} + \mathrm{Fe_n} + \mathrm{M} \longrightarrow \mathrm{Fe_{n+1}} + \mathrm{M}, \tag{2.14}$$

with analogous reactions for other metals, like Si or Mg. This step is the bottleneck of clusters formation, due to its small rate and high activation barrier, thus requiring high temperatures and high densities to proceed. The formation then continues with coagulation of small clusters together to form bigger clusters:

$$\mathrm{Fe_2} + \mathrm{Fe_2} \longrightarrow \mathrm{Fe_4}, \tag{2.15}$$

while destruction happens via thermal fragmentation

$$\mathrm{Fe_n} + \mathrm{M} \longrightarrow \mathrm{Fe_{n-1}} + \mathrm{M}. \tag{2.16}$$

Metal oxides, like magnesium oxide (MgO) or iron oxide (FeO), forms starting from oxidation with O_2 or CO_2

$$\mathrm{Fe} + \mathrm{O_2} \longrightarrow \mathrm{FeO} + \mathrm{O}, \tag{2.17}$$

$$\mathrm{Fe} + \mathrm{CO_2} \longrightarrow \mathrm{FeO} + \mathrm{CO}. \tag{2.18}$$

This monomers then grow by successives polymerizations

$$\mathrm{FeO} + (\mathrm{FeO})_\mathrm{n} \longrightarrow (\mathrm{FeO})_{\mathrm{n+1}}. \tag{2.19}$$

Metal sulfides like MgS and FeS have no documented rates. We use the isovalence between O and S to estimate the rates for the main formation processes

$$\mathrm{Fe} + \mathrm{S_2} \longrightarrow \mathrm{FeS} + \mathrm{S}, \tag{2.20}$$

$$\mathrm{Fe} + \mathrm{SO} \longrightarrow \mathrm{FeS} + \mathrm{S}, \tag{2.21}$$

and the following polymerization

$$\mathrm{FeS} + (\mathrm{FeS})_\mathrm{n} \longrightarrow (\mathrm{FeS})_{\mathrm{n}+1}. \tag{2.22}$$

Our ejecta present carbon rich, hydrogen poor external zones, where pure carbon dust can form. We thus include the formation of carbon chains up to C_9, followed by the ringed-structured C_{10}, which is more stable and thus not subject to destruction by reactions with He^+ or oxygen. These formation reactions are of the form

$$\mathrm{C} + \mathrm{C_n} \longrightarrow \mathrm{C_{n+1}} + h\nu. \tag{2.23}$$

For the formation of carbon chains we use different rates for high and low ejecta temperature. The high temperature rates follow Andreazza & Singh, who propose a low rate for the formation of C_2 (10^{-17} cm^3 s^{-1}) and higher ones for larger chains C_n, with n$\geq$ 3 (10^{-10} cm^3 s^{-1}). Wakelam et al. (2009) suggest, for a temperature between 10 and 300 K, different and temperature dependent rates for the formation of C_3 and C_4, $3 \times 10^{-16}\times$ $(\mathrm{T}/300)^{-1}$ and $4 \times 10^{-14}\times$ $(\mathrm{T}/300)^{-1}$, respectively. We use the first rates for the first 1000 days, and the second ones from 1000 days on.
We also include an alternative route to formation of carbon chains

$$\mathrm{C_{n-m}} + \mathrm{C_n} \longrightarrow \mathrm{C_n}, \tag{2.24}$$

with rates derived from Clayton et al. (2001). Destruction processes include thermal fragmentation via collision with the ambient gas

$$\mathrm{C_n} + \mathrm{M} \longrightarrow \mathrm{C_{n-m}} + \mathrm{C_m} + \mathrm{M}, \tag{2.25}$$

reactions with oxygen

$$\mathrm{O} + \mathrm{C_n} \longrightarrow \mathrm{C_{n-1}} + \mathrm{CO}, \tag{2.26}$$

compton electron collisions

$$\mathrm{C_n} + e^- \longrightarrow \mathrm{C_{n-m}} + \mathrm{C_m} + e^-, \tag{2.27}$$

and destruction by He^+, of particular importance since carbon is likely formed in the external zones of ejecta, rich in helium

$$\mathrm{C_n} + \mathrm{He^+} \longrightarrow \mathrm{C_{n-1}} + \mathrm{C^+} + \mathrm{He}. \tag{2.28}$$

The growth of carbon clusters larger than C_{10} is described following an approach proposed by Sarangi & Cherchneff (accepted), whereby the growth is powered by the addition of C_2 to the carbon lattice

$$\mathrm{C_2} + \mathrm{C_n} \longrightarrow \mathrm{C_{n+1}} + \mathrm{C}, \tag{2.29}$$

with a flat rate of 10^{-10} estimated from rates for smaller chains taken from Clayton et al. (1999). We follow the formation of carbon clusters until C_{28}, which forms the first stable cage structure.
Silicon carbide is formed according to the reactions

$$\mathrm{Si} + \mathrm{CO} \longrightarrow \mathrm{SiC} + \mathrm{O}, \tag{2.30}$$

$$\mathrm{Si} + \mathrm{C_2} \longrightarrow \mathrm{SiC} + \mathrm{C}, \tag{2.31}$$

$$\mathrm{SiO} + \mathrm{C} \longrightarrow \mathrm{SiC} + \mathrm{O}, \tag{2.32}$$

$$\mathrm{Si} + \mathrm{C} \longrightarrow \mathrm{SiC} + h\nu, \tag{2.33}$$

and nucleates then in $(\mathrm{SiC})_2$

$$\mathrm{SiC} + \mathrm{SiC} \longrightarrow (\mathrm{SiC})_2. \tag{2.34}$$

Rates are taken from the similar reactions involving SiO, since the two clusters have a similar geometric structure. The considered destruction processes are

$$\mathrm{SiC} + \mathrm{He^+} \longrightarrow \mathrm{Si} + \mathrm{C^+} + \mathrm{He}, \tag{2.35}$$

$$\mathrm{SiC} + \mathrm{O} \longrightarrow \mathrm{Si} + \mathrm{CO}, \tag{2.36}$$

$$\mathrm{SiC} + \mathrm{C} \longrightarrow \mathrm{Si} + \mathrm{C_2}, \tag{2.37}$$

$$\mathrm{SiC} + \mathrm{O} \longrightarrow \mathrm{SiO} + \mathrm{C}, \tag{2.38}$$

$$\mathrm{SiC} + \mathrm{M} \longrightarrow \mathrm{Si} + \mathrm{C} + \mathrm{M}. \tag{2.39}$$

The last process is also used for the destruction of $(\mathrm{SiC})_2$.
For the nucleation of small silicate clusters (forsterite dimer, $(\mathrm{Mg_2SiO_4})_2$, and enstatite dimer, $(\mathrm{MgSiO_3})_2$), we follow the approach of Goumans & Bromley (2012). In this paper the authors indicate a possible route to the formation of forsterite and enstatite via the growth of SiO to $(\mathrm{SiO})_2$ and $\mathrm{Si_2O_3}$. The clusters continue to grow then by alternate additions of magnesium and oxygen to the structure. The first processes in the chain are bimolecular reactions with a small activation barrier, while the subsequent inclusions of magnesium and oxygen are downhill and with no energy barrier.
Sarangi & Cherchneff (2013) derive a scheme of reaction paths that describes the polymerisation of SiO and the growth of silicate clusters up to forsterite dimers by considering the oxidising agents $\mathrm{O_2}$ and SO. This scheme is used in our model and represented in Figure 2.4.

We consider also a new pathway for the formation of the alumina dimer, $(\mathrm{Al_2O_3})_2$. Because the structure of the molecule $\mathrm{Al_2O_3}$ is akin to that of $\mathrm{Si_2O_3}$, we consider a similar growth route starting from the formation of AlO and followed by its dimerisation to $\mathrm{Al_2O_2}$ and the formation of $\mathrm{Al_2O_3}$ via oxidation. The alumina dimers are then formed from the recombination of two $\mathrm{Al_2O_3}$ molecules. Oxidising agents for the formation of silicates and alumina include atomic O, $\mathrm{O_2}$, AlO, and SO, but reactions with $\mathrm{O_2}$ and SO are prevalent for silicate clusters while reaction with AlO dominates in the case of alumina.

In order to calculate the final yields of the species considered, we collect all the chemical reactions rates for the elements and clusters in Table 2.5 in a chemical network.
This chemical network and chemical abundances are used as inputs in our code, in order to solve the chemical kinetic equations. We use the Gear's method (Gear, 1971) to solve Eq. 2.4, which represents a system of i non-linear, coupled, stiff differential equations, one for each species considered. An equation is stiff when it contains terms that can lead to rapid variation in the solution. These abrupt transitions in the time series are often the result of different time scales in the dynamics of the system. This behaviour makes certain numerical methods unstable, unless the step size is taken to be extremely small, even when the solution curve is smooth. Backward differentiation is an implicit multi-step method designed for solving stiff system of differential equations, and needs to be used in conjunction with a predictor and a corrector to ensure convergence. The Gear's method

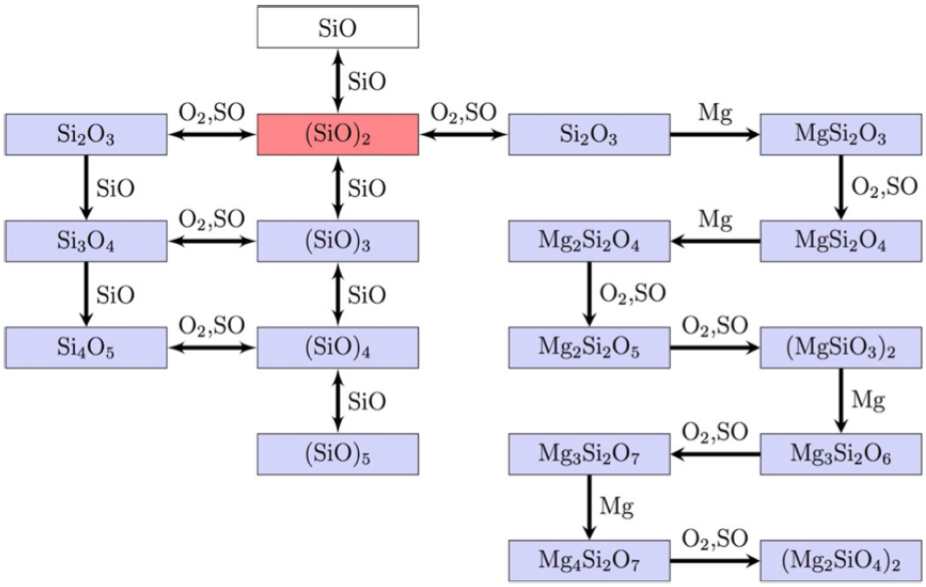

Figure 2.4: Chemical processes involved in the formation of enstatite and forsterite dimers, and the polymerisation of SiO. From Sarangi & Cherchneff (2013).

rewrites this predictor-corrector multi-step as a one step, and permits local alteration of the order of the method and of the mesh size. We implement this method using the LSODE subroutine (Hindmarsh, 1983). At each time step the code solves numerically the differential equations in order to calculate the evolution of species abundances, relative to gas number density, with time. We start from 100 days post-explosion and choose a time step of 10 days, which permits to follow the abundances evolution with time while maintaining a short running time of the code. We run the code until 3000 days post explosion for our ejecta model, when the gas number density and temperature are very low and most of the species abundances have reached a plateaux and are changing very slowly.

2.3 Results on the ejecta gas phase

2.3.1 Standard density

We first study homogeneous ejecta, whose number density and temperature profiles are given in Table 2.2, from 100 days to 3000 days post explosion, and study the variation of molecules and clusters mass with time. The resulting molecules and dust clusters masses in $M_\odot$ summed over all zones, are showed in Figure 2.5. Each zone contributes differently to the various chemical species based on its chemical composition. Heavy metal rich molecules, such as SiS or SO, form in the inner zones where these elements are prevalent, while molecules such as CO or O_2 form in the big oxygen rich zones that spans most of the ejecta. The two outer zones do not contribute to the molecular budget at this density due to their helium abundance. Helium is ionized after the explosion by the fast Compton electrons released by the decay of ^{56}Ni, and it is unable to recombine due to the rapidly decaying density. The large amount of He^+ in these zones thus ionizes other atoms by charge exchange, and breaks molecules via ion-molecule reactions, inhibiting their formation. A similar role is played by Ar^+ in the inner zones and by Ne^+ in the oxygen rich zone, though their lower abundance with respect to other element makes their

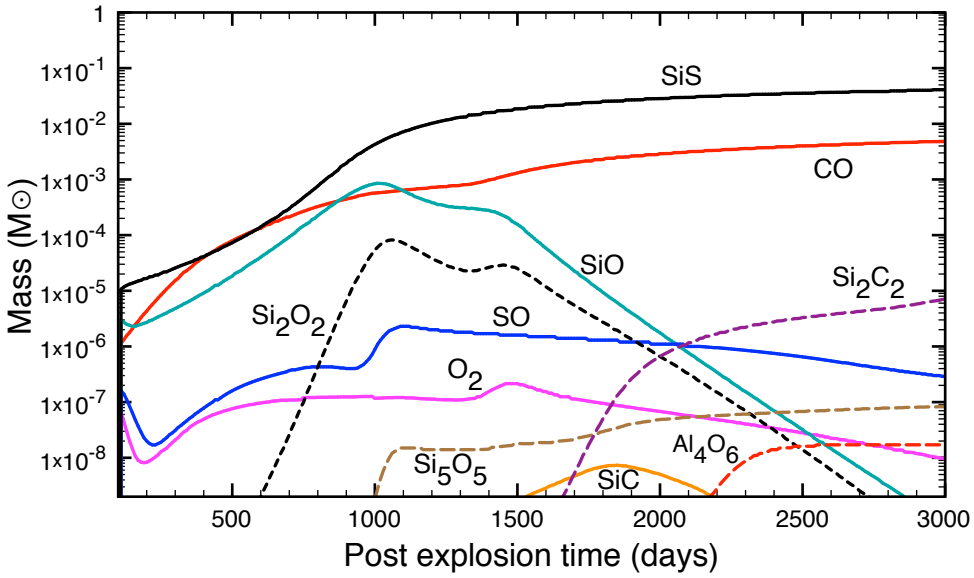

Figure 2.5: Masses of molecules and dust clusters in the ejecta as a function of post-explosion time. Biscaro & Cherchneff (2014)

contribution to the ionization of atoms and destruction of molecules less important. They are anyway effective in limiting the formation of molecules and clusters until ∼1000 days. As shown in Figure 2.6, while Ar^+ and Ne^+ eventually recombine, with masses decaying

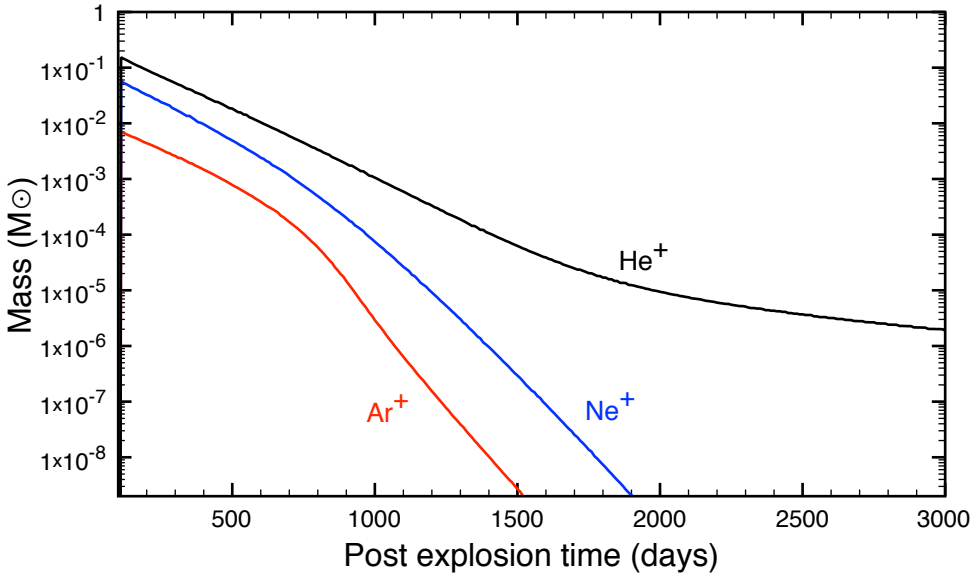

Figure 2.6: Masses of: Ar^+ summed over zones 1A/B, Ne^+ summed over zones 2,3A/B, and He^+ summed over zones 3B/4A/B.

fast after ∼1000 days, He^+ is still abundant at 3000 days, making the outer zones unable to form molecules and clusters until very late post explosion times.

The dominant species at this gas number density is SiS, which forms in the metal rich inner zones 1A/B of the ejecta, mainly from the radiative association reaction

$$\mathrm{SiS} + \mathrm{S} \longrightarrow \mathrm{SiS} + h\nu, \tag{2.40}$$

since this reaction has no energy barrier and is temperature independent, it contributes successfully to the formation of SiS even at later times. Destruction is mainly provided by the reaction

$$\mathrm{SiS} + \mathrm{Ar}^{+} \longrightarrow \mathrm{Si}^{+} + \mathrm{S} + \mathrm{Ar}. \tag{2.41}$$

The second most abundant molecule, CO, forms mainly in the oxygen rich zones also via radiative association

$$\mathrm{C} + \mathrm{O} \longrightarrow \mathrm{CO} + h\nu, \tag{2.42}$$

and via reaction with O_2

$$\mathrm{C} + \mathrm{O}_2 \longrightarrow \mathrm{CO} + \mathrm{O}. \tag{2.43}$$

CO destruction is mainly carried out by destruction by Compton electrons at early times post explosion, and at later times by charge-exchange reactions with O^+ and Ne^+, of the form

$$\mathrm{CO} + \mathrm{O}^{+} \longrightarrow \mathrm{CO}^{+} + \mathrm{O}, \tag{2.44}$$

$$\mathrm{CO} + \mathrm{Ne}^{+} \longrightarrow \mathrm{CO}^{+} + \mathrm{Ne}. \tag{2.45}$$

CO has been observed in Cas A by Rho et al. (2012) with detection in nine different positions in the remnant, with CO temperatures between 900 and 2500 K and CO mass in the range 2.4×10^{-5} -6×10^{-5} $M_\odot$. These masses are smaller than the ones calculated here, but the relatively high CO temperature suggests CO has been shocked by the reverse shock, and reformed after the shock (see Section 3). Wallström et al. (2013) also detect CO rotational lines in the submillimetre with the space telescope Herschel in a small region of Cas A where hot CO has been detected by Rho et al. (2009a) (see Section 4).
Figure 2.7 shows that in our model, CO forms in almost every zone of the ejecta, with the exceptions of the innermost zone, poor in oxygen and carbon, and of the outermost zone, due to the low carbon and oxygen abundances and high helium percentage. The formation is delayed in zone 3B due to the moderate helium abundance in this zone, which slows down the formation at early days. Contrary to the outer zones 4A/B, in this zone the lower helium abundance permits the recombination of He^+ around 1000 days, and a late formation of molecules.
Silicon monoxide primarily forms in zones 1B and 2 with a small contribution from zones 3A/B from the following radiative association process

$$\mathrm{Si} + \mathrm{O} \longrightarrow \mathrm{SiO} + h\nu, \tag{2.46}$$

and it is destroyed by the reaction

$$\mathrm{SiO} + \mathrm{Ne}^{+} \longrightarrow \mathrm{Si} + \mathrm{O}^{+} + \mathrm{Ne}. \tag{2.47}$$

Its peak and subsequent decrease in mass after 1000 days is explained by SiO depletion into $(SiO)_n$ clusters, which ends with a small mass of $(SiO)_5$ formed between 1000 and

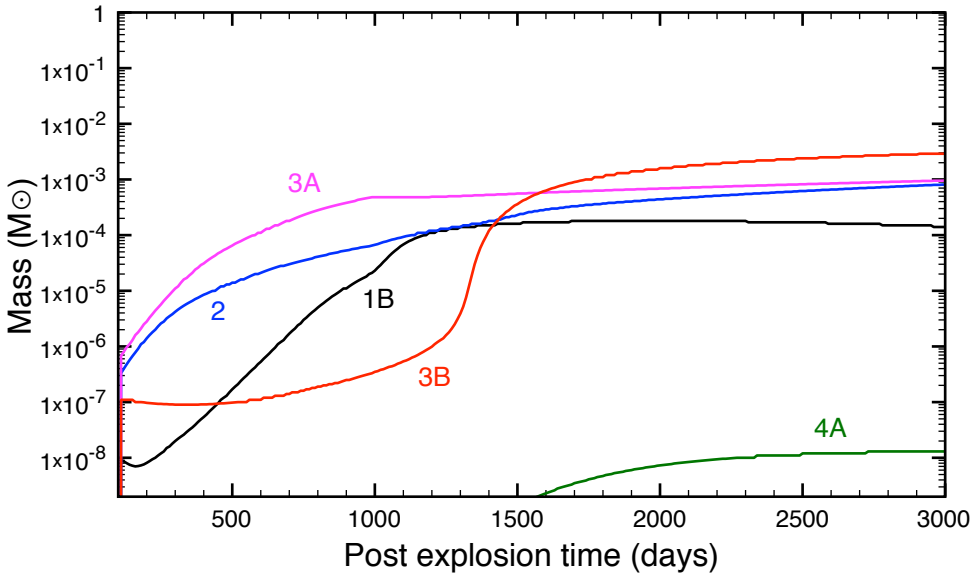

Figure 2.7: Mass of CO formed in the various zones of the ejecta.

3000 days.
SO forms in zone 1A from the radiative association

$$S + O \longrightarrow SO + h\nu, \tag{2.48}$$

and it is destroyed from charge exchange with various ions present in zone 1B, as well as by Compton electron fragmentation.
O_2 forms in zones 1B/2/3 also from radiative association

$$O + O \longrightarrow O_2 + h\nu, \tag{2.49}$$

and it is destroyed by reactions with Ne^+ and with carbon, forming carbon monoxide and oxygen:

$$O_2 + Ne^+ \longrightarrow O + O^+ + Ne, \tag{2.50}$$

$$O_2 + C \longrightarrow CO + O. \tag{2.51}$$

The most abundant dust cluster formed is $(SiO)_5$ in zones 1B, 2, 3A/B, which is responsible for the depletion of SiO and $(SiO)_2$ after 1000 days. No significant amount of silicate dust clusters forms in the O-rich zones of the ejecta because the first chemical steps in the synthesis of forsterite and enstatite dimers involve neutral-neutral processes with a moderate activation barrier (see Section 2.1), and higher gas temperatures than those found at day ∼1000 in the ejecta are thus required. The low-gas density at day > 1000 also hampers the efficient nucleation of silicate clusters.
After He^+ starts to recombine and its abundance to decrease around 1500 days, some SiC dimers begin to form in the outer zones 4A/B, but due to the low density of the ejecta at this point, a significant growth in mass is no longer possible.

Table 2.6 summarises, in the column labelled "Standard", the results for the homogeneous low gas number density ejecta of a type IIb SN. The efficiency of molecule formation is very low, at only 1.2 %, and the total mass of dust clusters is 8.2×10^{-6} $M_\odot$.

Density Case:	Standard	x200	x2000
Molecules			
SiS	4.1×10^{-2}	1.3×10^{-1}	5.7×10^{-2}
CO	4.8×10^{-3}	4.9×10^{-1}	4.9×10^{-1}
SiO	6.7×10^{-10}	8.7×10^{-12}	1.8×10^{-12}
O_2	9.5×10^{-9}	5.8×10^{-1}	1.07
SO	2.9×10^{-7}	2.6×10^{-2}	7.7×10^{-2}
Total Mass	4.6×10^{-2}	1.22	1.69
Efficiency	1.2%	31 %	43 %
Clusters			
Silicates	$--$	3.2×10^{-3}	1.3×10^{-2}
SiC	7.9×10^{-6}	3.5×10^{-4}	1.3×10^{-4}
Silica	2.7×10^{-7}	1.4×10^{-9}	8.0×10^{-15}
Alumina	1.7×10^{-8}	1.7×10^{-2}	1.4×10^{-2}
Pure metals	4.5×10^{-10}	8.8×10^{-5}	8.0×10^{-3}
Carbon	$--$	7.5×10^{-12}	9.4×10^{-3}
Iron sulphide	$--$	6.6×10^{-10}	6.2×10^{-7}
Total Mass	8.2×10^{-6}	0.021	0.045
Efficiency	0.0002 %	0.52 %	1.1%

Table 2.6: Masses of molecules and dust clusters (in $M_\odot$) at 3000 days post-explosion for the Type IIb SN with a 19 $M_\odot$progenitor that led to Cas A. The gas density cases correspond to the "standard case" and increase of 200 and 2000 in the gas number density, as discussed in the text. Efficiencies are the mass fraction of the ejected material in the form of molecules or dust clusters. Silicates correspond to forsterite clusters, pure metals to Fe, Si, and Mg clusters, and silica to polymers of SiO. (Biscaro & Cherchneff, 2014)

Spitzer and Herschel data on Cas A observed several characteristic dust spectra at various wavelengths. Fits are performed in several papers (Arendt et al., 2014; Rho et al., 2008), and the dust composition is inferred to be a combination of mainly silicates and aluminium oxides, with the presence of other dust species, such as graphite, amorphous carbon, sulphides and iron oxides, as secondary fitting components. The mass derived is between 0.02 and 0.054 $M_\odot$ in Rho et al. (2008) and $\lesssim$ 0.1 $M_\odot$ for Arendt et al. (2014).
When considering the gas phase chemistry to be out of equilibrium, dust clusters need to form out of the gas phase elements before dust can condense. This represents a bottleneck to the dust condensation process, since the low clusters formation efficiency at this density and the low density in the gas efficiently hamper dust formation.
Also, not all dust clusters automatically condense into dust, since this step is also density dependent (see Section 2.4). Our total mass of clusters ($\lesssim 10^{-5}$ $M_\odot$) is thus an upper limit to the possible dust mass that condense in the ejecta, and does not reflect the abundance or the chemical complexity found in observations.
The use of chemical kinetics leads also to contrasting results with the theoretical study of dust formation and evolution in Cas A by Nozawa et al. (2010), which finds 0.167 $M_\odot$ of dust with a complex composition. Their study is based on classical nucleation theory, and assumes all carbon and silicon atoms are locked up in CO and SiO when their abundances is less than that of oxygen. Our model, in contrast, with its very low molecule formation efficiency due to out of equilibrium destruction processes, leaves most of the gas in atomic form in every zone of the ejecta. These results highlight the importance of gas density in forming molecules and dust precursors. The ejecta may not be a homogeneous, low density gas, but may include clumps. The presence of high density clumps or knots in the ejecta impacts the chemistry and the synthesis of molecule sand dust clusters, and must be taken into account.

2.3.2 Enhanced densities

To test the results for a clumpy model of the ejecta, we first made a study on how the density of the gas impacts the results in terms of mass yields of molecules and dust clusters. We increase the ejecta number density of our standard case by various factors x ranging between 10 and 2000. This increase is applied to all zones of the ejecta at the beginning of the simulation, with the same time dependency as for the standard case. The temperature is left unchanged. We choose number density increments of 10, 200 and 2000. A density increase of 200 is the one that probably characterises clumps in Cas A, as explained in Section 3.
A density increase of 2000 reaches densities typical of a SN type IIP like SN1987A, and it is useful to consider larger number density increase to assess the impact of clumping on molecule and dust production.

Figure 2.8 shows the masses of dust clusters at 3000 days post explosion, as a function of gas number density increase. The same masses, plus molecules masses and efficiencies, are also shown in Table 2.6 for the x = 200 and x = 2000 cases. The case x = 1 is the "standard case" shown in the previous section, with a small final mass of silicon carbide, silica and alumina. For a number density increase of 10, some pure metal clusters start to appear. Mg_4 is formed mainly in the oxygen rich zones of the ejecta, while Si_4 and Fe_4 come from the innermost metal rich zone.
For a number density increase of 200, alumina and forsterite dominate the dust cluster mass, followed by silicon carbide and pure metal clusters. Silica decrease, as much of the silicon needed is locked up into forsterite, as most of the reactions for its formation are

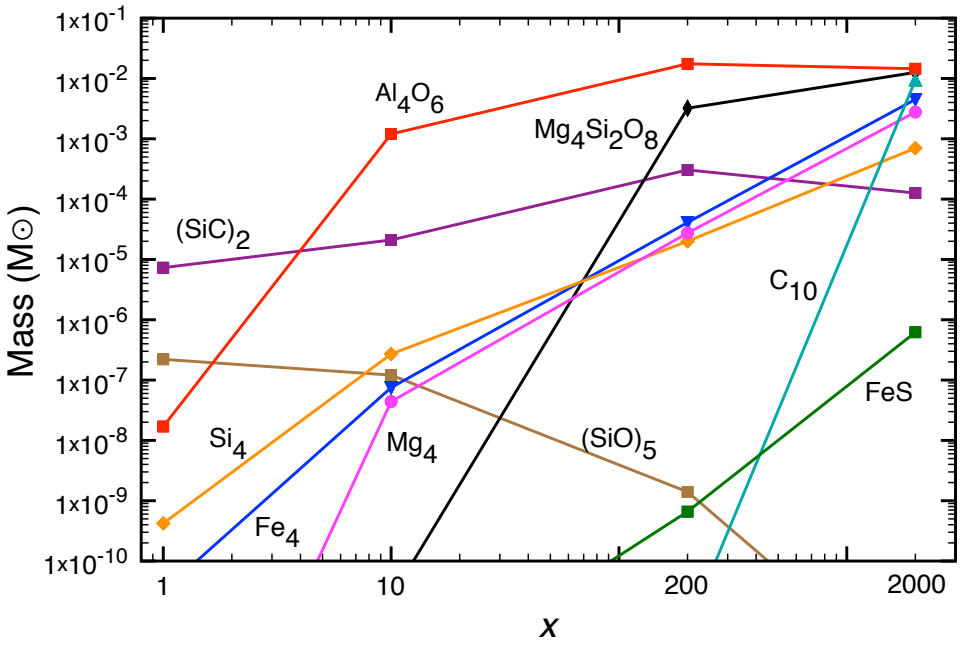

Figure 2.8: Masses of dust clusters in the ejecta at 3000 days post-explosion as a function of number density increase for the Type IIb SN with 19 $M_\odot$ progenitor that led to Cas A. The x axis represents the increment of density with respect to our "standard case" (which corresponds to $x = 1$). (Biscaro & Cherchneff 2014)

downhill and without energy barriers, and thus effective at every temperature (see Section 2.1). The carbon clusters still have a low mass at this density, and need a further number density increase to x = 2000 to form in appreciable quantities before 3000 days. This has two main explanations. First, the presence of helium in the outer, carbon rich zones, which recombines faster at larger densities, still delays and hampers molecules formation, and carbon chains forms almost exclusively in the carbon and helium rich outer zones. Second, the synthesis of large carbon clusters requires complex chemical routes to proceed. This happens at high gas number densities.

Figure 2.9 shows the time evolution of masses of molecules (top) and clusters (bottom) for the x = 200 case. We will discuss this case in more detail, since it is the most compatible with the calculated clump density in Cas A. It can be seen that all molecules and clusters form at earlier times compared with the standard density case, and with higher final masses. The most abundant molecules are CO and O_2, which form in the oxygen-rich zones with masses of ~ 0.5 $M_\odot$, followed by SiS and SO from the inner, metals rich zones. The large increase in O_2 mass compared with values for the standard case is due to the opening up of two new formation routes

$$CO + O \longrightarrow C + O_2, \tag{2.52}$$

$$AlO + O \longrightarrow Al + O_2. \tag{2.53}$$

This neutral-neutral reactions occur because the higher gas number density leads to higher abundances of CO and AlO early. The higher density also makes the radiative association formation route more efficient. This new routes permit a higher abundance of O_2 at early times. The presence of more O_2 early in the gas phase in turn makes its reactions with

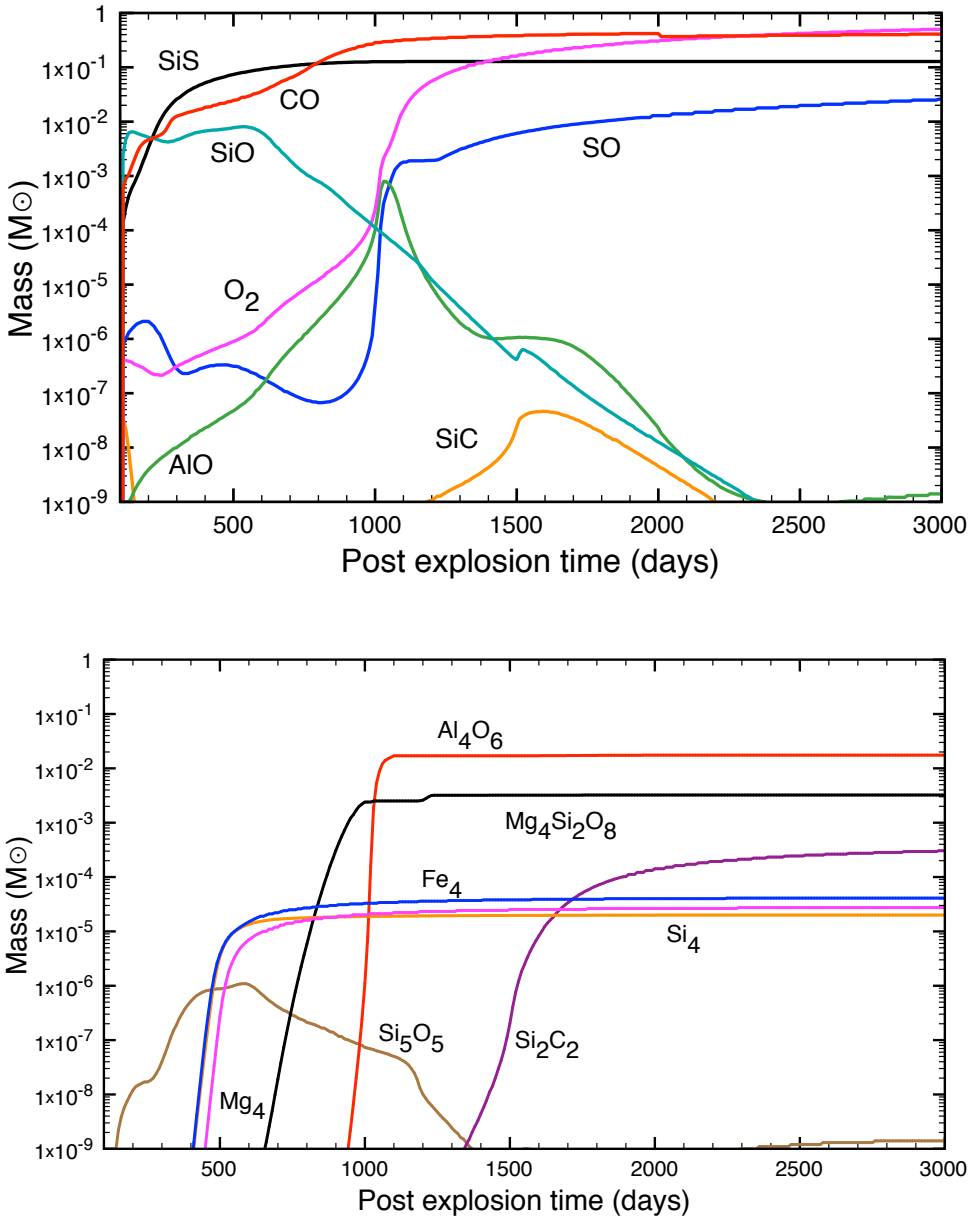

Figure 2.9: Masses of molecules and dust clusters in the ejecta as a function of post-explosion time for the Type IIb SN with 19 $M_{\odot}$ progenitor that led to Cas A, assuming a number density increase of 200 with respect to the "standard case". Top: masses of molecules; Bottom: masses of dust clusters. (Biscaro & Cherchneff 2014)

CO, SiO or SO more important, leading to an active chemistry, to more formation routes compared with the standard density, and to higher formation rates for these molecules. Other molecules, such as SiO, are quickly depleted into dust clusters. As soon as the effect of Compton electron becomes less important, clusters begin to rapidly form in the ejecta, often with a very steep increase in mass, followed by a gradual mass variation over time. Figure 2.10 shows the much faster recombination of Ar^+, Ne^+ and He^+ in the x= 200 case with respect to the standard density case. The higher density facilitates the early recombination of these active ions, leading to a faster and richer molecule and clusters

formation.
Alumina, with a mass of 10^{-2} $M_{\odot}$, is the main dust cluster present, followed by forsterite

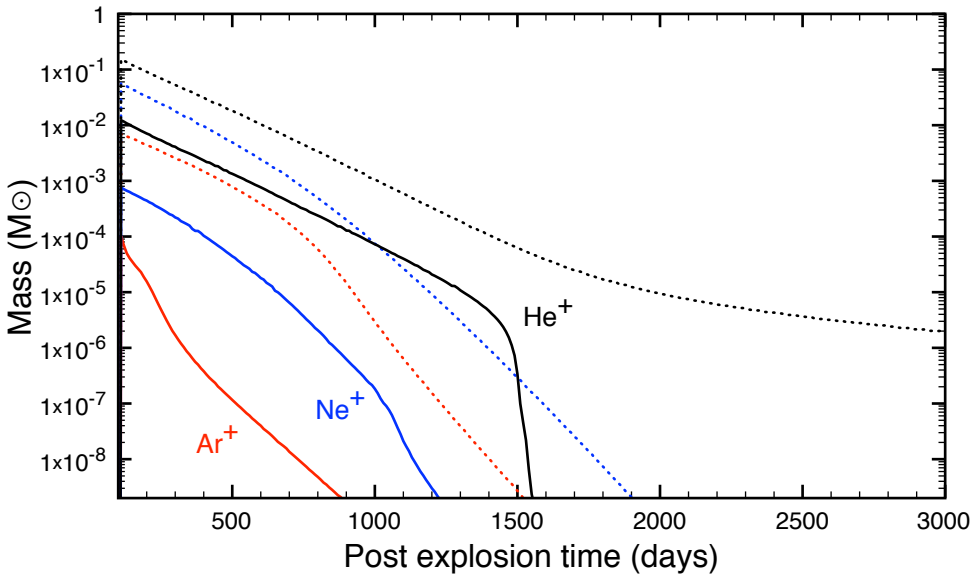

Figure 2.10: Masses of: Ar^+ summed over zones 1A/B, Ne^+ summed over zones 2,3A/B, and He^+ summed over zones 3B/4A/B for x = 200 case. The dotted lines correspond to the masses in the x = 1 case for the three ions considered, for comparison.

at 3×10^{-3} $M_{\odot}$, with silicon carbide and pure metal clusters following at lower masses. Table 2.6 compares final masses at 3000 days and efficiencies for the standard case and the 200 and 2000 times increase in number density. All species formation efficiencies increase with number density, but dust clusters constitute only 1.1 % of the mass of the ejecta, which stays mostly molecular and atomic form.
O_2 and SO are the molecules that present the most dramatic increase in mass with density, mainly due to the opening of new chemical routes effective at high number density.
For dust clusters, forsterite present the larger growth with density, due to the downhill pathway that permits a rapid formation after the initial high temperatures allow a quick proceeding of the first reaction energy barrier (see Sect 2.1). Alumina already peaks in mass at x = 200, decreasing slightly in the case x = 2000. Both alumina and forsterite need to interact with O_2 in their formation routes. Alumina needs it in the first step, to form AlO, while forsterite has several oxidation step in its formation route. In the case of x = 2000, more forsterite forms more rapidly out of oxidation with O_2, in competition with the formation of AlO. Furthermore, the destruction of alumina is a termolecular reaction which becomes more efficienty at higher densities, since it needs impacts with the gas to proceed.

This section thus shows that a clumpy ejecta is necessary to explain the masses and chemical composition of the dust observed in Cas A, with a number density increase in clumps that ranges between 200 and 2000.

2.4 Dust condensation

In order to model the condensation of small dust clusters into small grains, we follow the approach of Sarangi & Cherchneff (accepted). They consider the grow of dust seeds by coagulation to form large grains, using the formalism developed by Jacobson (2005).
The variation of the number density of a grain with a volume v with time follows a differential equation of the form

$$\frac{dn_v(t)}{dt} = \frac{1}{2}\int_0^v \beta_{v-v',v} n_{v-v'} n_{v'} dv' - n_v \int_0^\infty \beta_{v,v'} n_{v'} dv', \tag{2.54}$$

where t is the time, v' and $(v - v')$ are the volumes of the coagulating particles, n_v is the number density of grains with volume v and $\beta_{v,v'}$ is the rate coefficient of coagulation for particles with volumes v and v'. This rate is determined by physical processes such as Brownian diffusion, convective Brownian motion enhancement, gravitational collection, turbulent inertial motion and Van der Waal's forces. Brownian diffusion, i.e. the scattering, collision and coalescence of grains via Brownian motion, dominates in a free-molecular regime, when the mean free path of a particle is much greater than the radius of particle. For the case of dust in SN ejecta, the gas number densities involved at the start of dust coagulation at $\sim$ 300 days post explosion are of the order of 10^6- 10^7 cm^{-3} for a type IIb SN, and of 10^9 - 10^{11} cm^{-3} for a type IIP. These values for the gas number densities put the ejecta gas in a free-molecular regime.
In this regime, Van del Waal's forces develop a weak local charge fluctuations that facilitates the coagulation for particles with size in the molecular range. This effect is taken into account by modelling the interaction potential between two particles with Hamaker's theory using London dispersion forces (Alam, 1987; Sceats, 1989).
The final coagulation rate $\beta_{v,v'}$ is dominated by Brownian diffusion and a coalescence enhancement factor due to Van der Wall's forces, that ranges between 1 and 5.
If we define the ratio of the radii of the two colliding particles as

$$f_a = \frac{a_i}{a_j}, \quad a_i \geq a_j, \tag{2.55}$$

then the Brownian diffusion is proportional to f_a, while the coalescence factor is inversely proportional to it. Since the rate coefficient is dominated by Brownian diffusion in the free-molecular regime, the rate is minimum when $f_a = 1$. This makes large grains in the ejecta very effective in coagulating with small grains, while particles very close in size will not efficiently coagulate. Typical values for $\beta_{v,v'}$ are in the range 10^{-9} - 10^{-4} cm^{-3} s^{-1}.
Equation 2.54 is solved in a semi-implicit way such that volume is conserved and dust grains maintain a spherical structure. Different volumes are modelled as discrete bins, with the first bin corresponding to the volume of the gas-phase cluster used as seed for the grains. This formalism is incorporated into the chemical kinetic model of the gas-phase, so that at each time step both gas phase abundances and dust grain sizes are calculated simultaneously. For our study we consider four dust species: forsterite, alumina, carbon and silicon carbide, with seeds $Mg_4Si_2O_8$, Al_4O_6, C_{28} and $(SiC)_2$, respectively.

We follow the gas-phase chemistry coupled to the dust condensation for 4000 days and derive a size distribution for a number density enhancement of 200 and 2000, as shown in figures 2.11 and 2.12. Forsterite and alumina form prevalently in zone 2 (see Table 2.1), with a small contribution to forsterite from zone 1b, while carbon and silicon carbide form in the outer zone 4a.

The grains are generally small, with a maximum size of a few hundreds angstroms for a number density enhancement of 200, and of around one thousand angstroms for an

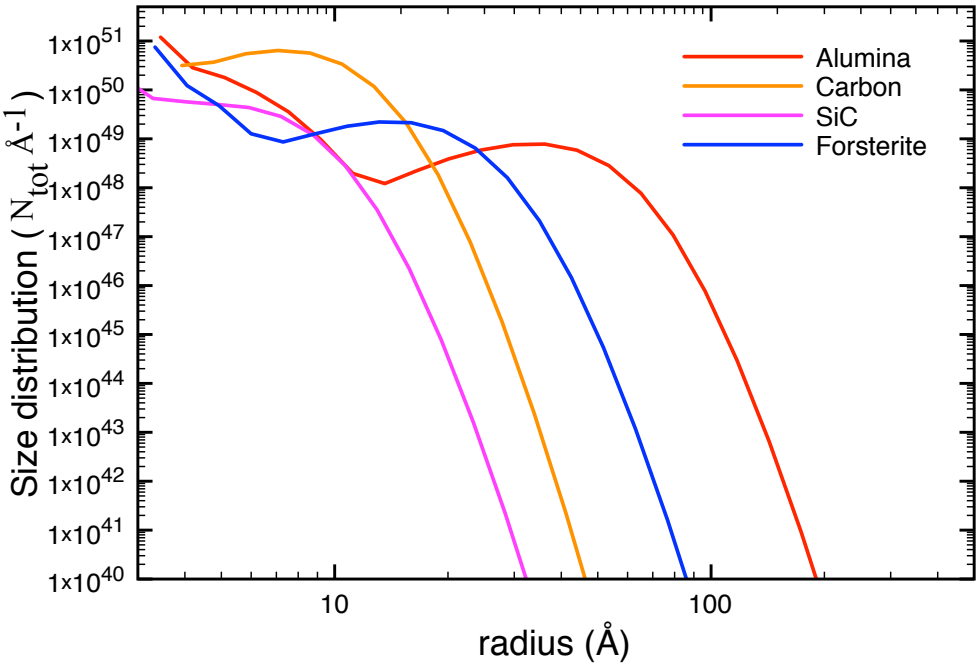

Figure 2.11: Total number of dust grains at 4000 days post explosion as a function of their radius for an ejecta gas number density enhanced by a factor 200.

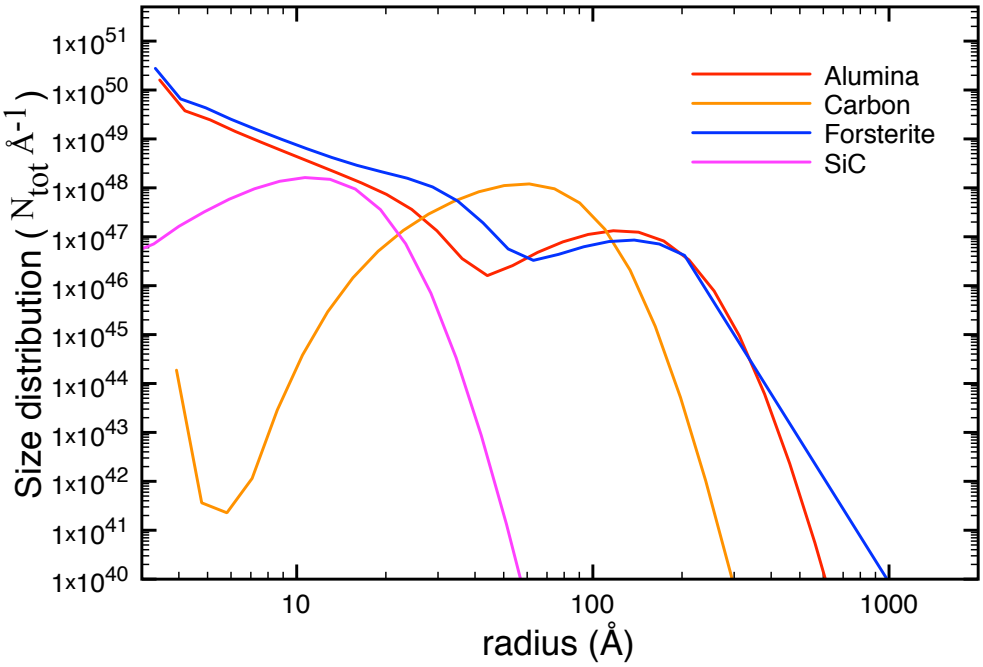

Figure 2.12: Total number of dust grains at 4000 days post-explosion as a function of their radius for an ejecta gas number density enhanced by a factor 2000.

enhancement of 2000. Alumina and forsterite form larger grains with respect to carbon and silicon carbide, owing to the delay in the formation of the latter dust species due to helium presence in the outer zones.

The derived dust masses and the dust seeds radii are shown in Table 2.7.

Dust species	Radius	Total mass	
		x200	x2000
Forsterite	3.33	3.1×10^{-3}	1.1×10^{-2}
Alumina	3.45	1.7×10^{-2}	1.4×10^{-2}
Carbon	3.93	7.0×10^{-3}	7.1×10^{-3}
Silicon Carbide	2.70	3.1×10^{-4}	9.1×10^{-5}

Table 2.7: Masses in $M_\odot$ and dust seeds radii in Å for the dust species considered. The columns x200, x2000 indicate the masses derived considering the whole ejecta in clumps with a number density enhancement of 200 or 2000, respectively.

3. Study of the reverse shock in Cas A

3.1 The reverse shock models

As shown in the previous section, dense clumps are necessary to form an appreciable amount of molecules and dust clusters in the ejecta and thus trigger efficient dust condensation. The presence of over-densities also helps dust to survive the impact of the reverse shock (RS): the shock slows down by a factor of $\sqrt{\chi}$, where $\chi = n_c/n_{ic}$ is the ratio of the number density of the clump n_c and the number density of the interclump medium n_{ic}. This relation comes from the conservation of momentum, which can be written as

$$n_{ic}v_{ic}^2 + P_{ic} = n_c v_c^2 + P_c, \tag{3.1}$$

where v is the shock velocity and P is the pressure, and the subscripts ic and c refer to the interclump medium and the clump, respectively. This relation can be rewritten as

$$\frac{v_c}{v_{ic}} \simeq (\sqrt{\chi})^{-1} \times \sqrt{F}, \tag{3.2}$$

where $F = P_{ic}/P_c$ is geometry dependent and ranges from a value of 1 for a planar shock to a maximum value less than 3 (Klein et al., 1994; Sutherland & Dopita, 1995). The deceleration of the shock is of particular importance for SN type IIb: due to their thin hydrogen envelope and high expansion velocity of the ejecta, the reverse shock is faster and impacts on the expanding ejecta at earlier times than in a type IIP SN (Nozawa et al., 2010). As a consequence, type IIb SN have less time to form molecules and dust grains before the ejecta is reprocessed by the reverse shock.
Fast moving knots (FMK) have been observed by Fesen et al. (2001) in the optical. Docenko & Sunyaev (2010), from their analysis of fine-structure far-IR atomic line, derived the reverse shock velocity in oxygen rich clumps to be $\sim$ 200 km s^{-1}, for an unshocked clump gas number density of 100 cm^{-3}.
We want to assess the fate of the chemical species, including molecules and dust clusters, within ejecta clumps that are processed by the RS. We thus investigate various RS velocities, derive the time-variation of the post-RS gas parameters, based on existing shock models, and apply our chemical kinetic formalism to study the post-RS chemistry.
Figure 3.4 shows a schematic representation of the conditions we considered after the passage of the reverse shock, as well as the different possible shock velocities in the clump. These velocities are derived from clump conditions derived from our SN ejecta model.
If we consider the oxygen rich zones in the ejecta, assuming an ejecta velocity of 4000 km s^{-1}, we can calculate the volume of the homogeneous ejected material at t days after the explosion

$$V(t) = \frac{4 \times \pi}{3} \times (v_{ej} \times t \times 8.64 \times 10^4)^3, \tag{3.3}$$

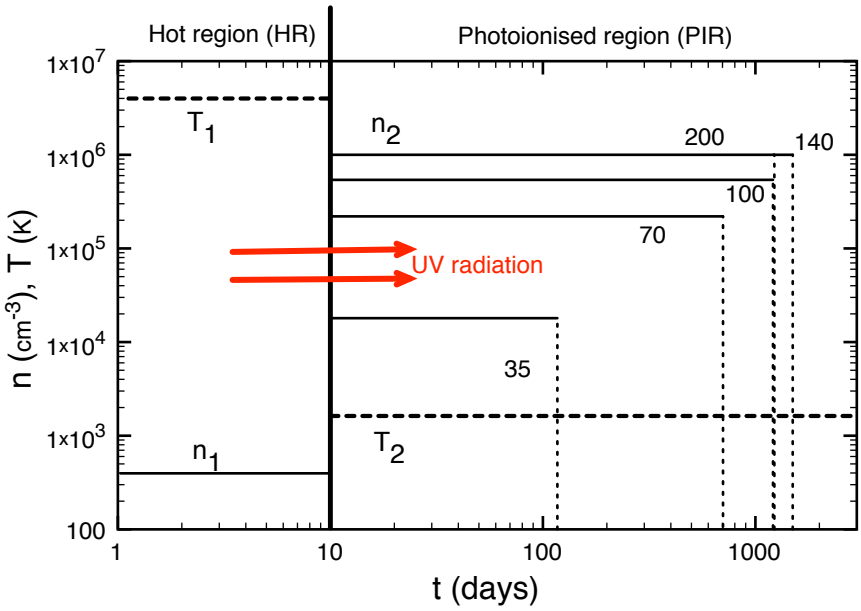

Figure 3.1: Schematic post-reverse shock structure including the cooling hot region (HR) and photoionised region (PIR). The shock is a t = 0 and moving to the left, gas temperature (dashed line) and number density (solid line) are given in Table 3.1. (Biscaro & Cherchneff, 2014).

where we assumed spherical expansion and v_{ej} is the ejecta velocity. This expression yields a value at 100 days equals to V(100) = 1.7 × 10^{47} cm^3. To assess how much of this volume is occupied we used a filling factor, which is defined as the fraction of the volume of the ejecta occupied by gas. Values for the clump filling factor, f_c, derived from radiative transfer studies of the dust emission in SN ejecta typically range from 0.05 to 0.2 (Gallagher et al., 2012). Assuming $f_c = 0.05$, we derive that the total volume in the form of clumps in the SN ejecta is

$$V_{tot,c}(100) = f_c \times V(100), \tag{3.4}$$

which yields a value of 8.6 × 10^{45} cm^3.
For our proposed Cas A ejecta mass of 3.94 $M_\odot$ (see Section 2.1), we derive a typical clump mass ranging from 10^{-3} $M_\odot$ to 3 × 10^{-3} $M_\odot$, where the number of clumps N_c is 3000 and 1000, respectively. These N_c values are usually used in radiative transfer models. Our derived clump mass is also consistent with values obtained from 3D hydrodynamic models of SN explosion (Hammer et al., 2010). The number density of one oxygen-rich clump at day 100 post explosion is then given by

$$n_c(100) = \frac{M_c}{V_{tot,c}(100)/N_c}, \tag{3.5}$$

with $n_c(100)$ = 3.4 × 10^{10} cm^{-3} for N_c = 1000. This gas number density is roughly a factor of 200 larger than the values listed in Table 2.2 for the O-rich zones.
Docenko & Sunyaev (2010) inferred a gas number density of 100 cm^{-3} for a non-shocked clump at the present time, i.e. ∼ 330 years post explosion.
Using Eq. 2.2 we derive a gas number density of 20 cm^{-3} for our 200 times denser ejecta, which is compatible with this value. A better match is possible if we consider a clump filling factor ∼ 0.01. This leads to a gas number density of 98 cm^{-3} after 330 years,

but requires an additional increase of one order of magnitude in gas number density compared to the values for an homogeneous ejecta. We consider clumps with an increase in gas number density with respect to the homogeneous ejecta of 200, derived from clump filling factors, and 2000, since this compatible with the densities inferred by Docenko & Sunyaev (2010) and is similar to the gas number density of a type IIP SN.Following Nozawa et al. (2010) we assume an inter-clump number density of 1 cm^{-3} or 0.1 cm^{-3}. This leads to a clump/inter-clump density contrast χ between 20 and 200, respectively.

Ratio clump/interclump	Reverse shock velocity (km/s)				
	1000	1500	2000	3000	4000
1	1000	1500	2000	3000	4000
20	224	335	447	671	894
50	141	212	283	424	565
100	100	150	200	300	400
1000	32	47	63	95	126
10'000	10	15	20	30	40

Figure 3.2: Attenuated reverse shock velocities in the clump in km s^{-1} as a function of the ratio clump/inter-clump and the unattenuated reverse shock velocity. The green cells represent the range of velocity derived for Cas A. The orange cells denote marginally compatible values.

Figure 3.2 shows the possible attenuated reverse shock velocities, as a function of unattenuated reverse shock velocities and χ. For a range of unattenuated initial reverse shock speeds of 1000 - 2000 km s^{-1}, and $20 \leq \chi \leq 100$, corresponding to an inter-clump number density of 1 cm^{-3}, possible reverse shock attenuated speeds range from 100 km s^{-1} to ∼200 km s^{-1}. If we consider an inter-clump number density of 0.1 cm^{-3}, with $\chi = 1000$, the attenuated reverse shock speeds range from ∼ 30 to ∼ 60 km s^{-1}. This range of reverse shock velocities has been modelled by Borkowski & Shull (1990), so we use their result together with the values derived by Docenko & Sunyaev (2010) for the 200 km s^{-1} shock.

In their paper, Borkowski & Shull (1990) model steady state radiative shocks including transport of energy by electrons. They consider a pure oxygen gas and compute photo-ionization up to O VI, as well as the recombination spectrum of the ions.

This treatment permits them to calculate emergent ultra violet fluxes for each shock velocity. They found high electron temperatures in the post-shock hot region (HR), in which the compression induces an equilibration between ions and electron which draw their temperature together via Coulomb collisions with ions. This high temperature leads to collisional ionization and rapid cooling. As a result, recombination lags behind cooling, leading to a constant ionization in the hot post-shock region, induced by the collisional ionization by electrons behind the shock front. This changes suddenly when the gas cools down, contracts and recombines rapidly, to be then heated again when the neutral oxygen is re-ionized by UV photons coming from the hot post-shock region. This leads to an extended photoionization zone (PIR) in which the temperature stays constant and around a few thousands degrees.

Borkowski & Shull calculated, for each shock velocity, the temperatures, ionizations and total oxygen column density in the two regions. Column density is defined as the number of a substance per unit area integrated along a path. An example of their derived temperatures and ionizations for a shock velocity of 140 km s^{-1} is shown in Figure 3.3. Table 3.1 lists the parameters we used for the various reverse shock speeds. We assume

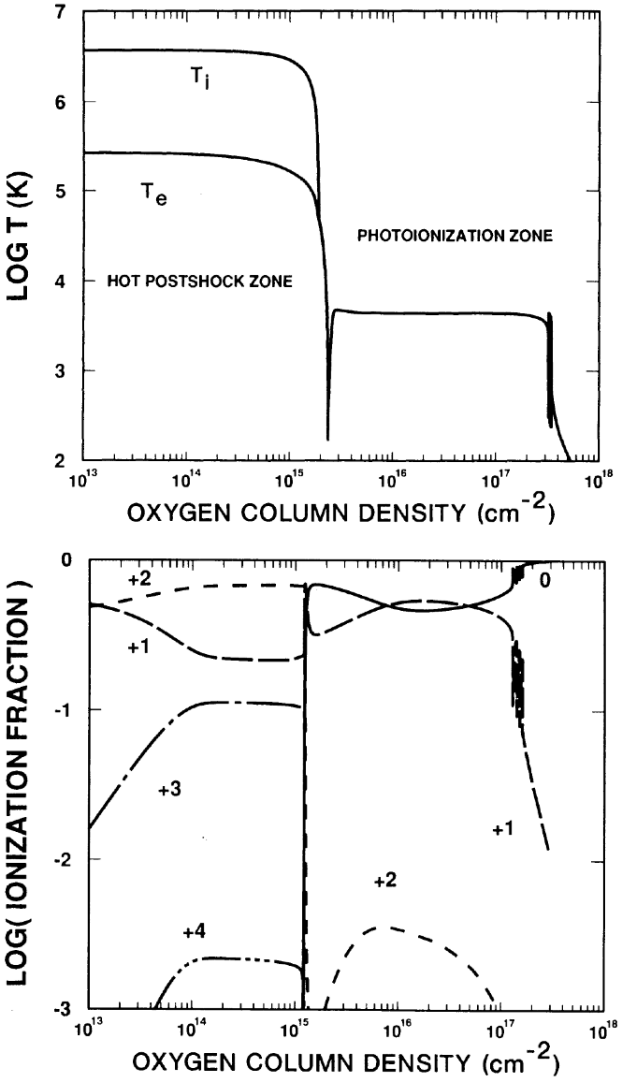

Figure 3.3: Top: Ion and electron temperatures as a function of oxygen column density for a 140 km s^{-1} shock model. Bottom: ionization fractions as a function of oxygen column density for the same model. From Borkowski & Shull (1990).

five velocities for the shock relative to the clump, an initial pre-shock gas number density in the clump of $n_0 = 100$ cm^{-3} .

The PIR length is not well constrained. Models of oxygen rich clumps crossed by shocks (Borkowski & Shull, 1990; Itoh, 1986, 1988) derived PIR lengths from their model which are not consistent with observed permitted OI lines. This forces them to truncate their derived length to match the observations.Sutherland & Dopita (1995) look at oxygen rich blobs interactions with the supernova remnant medium, and try to reproduce optical and UV spectrum with a bow shock structure in the clump. This approach however is not able to correctly reproduce Cas A observations, as shown in their Figure 13c, due to the contribution of high density material to the spectra. We use a PIR length $L_{PIR} = 2 \times 10^{11}$ cm for all models, as derived by Docenko & Sunyaev (2010). We use this value as it is derived by analysis of Cas A observations and is more relevant to our application.

In the PIR, we assume the oxygen column densities listed in Table 10 of Borkowski & Shull (1990) for the various shock speeds listed in Table 3.1.

V_s (km s^{-1})	Log$N(O)$ (cm^{-2})	n_2 (cm^{-3})	T_2 (K)	v_2 (m s^{-1})	t_{PIR} (years/days)
35	15.6	1.8×10^4	182	194.5	0.33/120
70	16.6	2.2×10^5	1500	31.8	1.98/723
100	17.0	5.4×10^5	1500	18.5	3.4/1241
140	17.3	1×10^6	1500	14.0	4.21/1537
200	17.0	1×10^6	1500	20.0	3.17/1157

Table 3.1: Reverse shock parameters as a function of attenuated RS velocity. The pre-shock number density n_0 and the PIR length L_{PIR} for all PIR models are 100 cm^{-3} and $2{\times}10^{11}$ cm, respectively. The T value for the 35 km s^{-1} shock is from Borkowski & Shull (1990) while other temperature values are derived from Docenko & Sunyaev (2010). Values for the column density $N(O)$ are taken from the shock models with conduction (70, 100, 140 km s^{-1}) and without conduction (35 km s^{-1}) of Borkowski & Shull (1990) except for the 200 km s^{-1} case. (Biscaro & Cherchneff, 2014).

The time length of the PIR is derived assuming the conservation of momentum through the shock front and is given by

$$t_{PIR} = \frac{N(O)}{n_2 \times v_2} = \frac{N(O)}{n_0 \times V_s}, \tag{3.6}$$

where $N(O)$ is the oxygen column density, V_s is the shock velocity, and v_2 the gas velocity in the PIR. The gas number density in the PIR n_2 is derived from the definition of the PIR length L_{PIR} given by

$$L_{PIR} = v_2 \times t_{PIR} = \frac{n_0}{n_2} \times V_s \times t_{PIR}. \tag{3.7}$$

The temperature proposed for the PIR regions is different in the two papers: we use the temperature T = 1500 K, proposed by Docenko & Sunyaev (2010) for high velocity shocks, while Borkowski & Shull (1990) propose a higher temperature of 4500 K. We test both temperatures (see Section 3.2 for details), but the results are not significantly different, so we use 1500 K for all shocks except the very slow one at 35 km s^{-1}. For this last case we use a low temperature (182 K) as derived by Borkowski & Shull (1990).
The hot post-shock region is a high temperature, high ionization region, and emits a flux of UV photons in the pre-shock medium, as well as in the photoionised region (Borkowski & Shull, 1990).These UV photons partially sustain the level of ionisation in the PIR via the photoionisation of oxygen. Borkowski & Shull (1990) estimate the photon fluxes emergent from the HR as a function of the shock velocity and energy band.
We include the effect of this UV flux in our chemistry as a non-thermal process that will ionise oxygen in various levels of O^+, involving UV photons with energy from between 13.62 and 35.12 eV as the main source of electrons in the PIR. We use this range as both the UV flux and the oxygen photoionisation cross section (taken from Angel & Samson (1988)) are larger than in other bands. In particular, the photoionisation cross section of oxygen reaches its maximum in a plateau between the energies of $\sim$ 17 to $\sim$ 25 eV, with steep decline before and after (see Fig. 3 of Angel & Samson (1988)). UV flux values are listed in Table 5 of Borkowski & Shull (1990) for the shock speeds considered in this study.
The unattenuated photoionisation rate for oxygen $\zeta_{0,\nu}$ at frequency ν is given by

$$\zeta_{0,\nu} = \int_\nu \sigma_\nu \times 4\pi \frac{J_\nu}{h\nu} \times d\nu, \tag{3.8}$$

where $4\pi J_\nu$ is the radiation intensity averaged over the solid angle and σ_ν is the photoionisation cross section of oxygen at the frequency ν. As the UV photons photoionise oxygen, they are gradually attenuated and degraded.
We estimate the unattenuated rate for the various frequency bands k and the integrated fluxes given in Tables 3 and 5 of Borkowski & Shull (1990), respectively, and calculate the frequency-dependent optical depth τ_k for each frequency band k, which is given by

$$\tau_k(t) = \sigma_k \times v_2 \times t \times n_2, \tag{3.9}$$

where t is the time in the PIR. The total attenuated photoionisation rate at time t in the PIR is then given by

$$\zeta(t) = \sum_k \zeta_{0,k} \times exp[-\tau_k(t)], \tag{3.10}$$

where $\zeta_{0,k}$ is the unattenuated photoionisation rate in the frequency band k. We add the photoionisation of oxygen as a non-thermal process in the chemical model discussed in section 2.1, with starting rate given by Eq. 3.9. The attenuated rate is calculated at each integration time step according to Equation 3.10.
Other non-thermal processes, such as Compton electron destruction, are not active anymore at the time of the crossing of the reverse shock, and are thus eliminated from the model.

3.2 Oxygen rich clump

Fast moving knots are observed in Cas A close or on the revershe shock location, and show optical and near-infrared lines of oxygen, sulphur, neon, argon and iron (Chevalier & Kirshner, 1979; Hurford & Fesen, 1996; Morse et al., 2004). This composition is similar to the one we used to model the oxygen rich zones of the SN ejecta. We consider a clump with the same composition of our ejecta zone 2 (see Table 2.1) with preshock number density 100 cm^{-3}, and postshocks conditions from Table 3.1 for the different shock speeds considered. We want to follow the chemistry of the gas, and track abundances of molecules and dust clusters as a function of time, so we apply to this case the same formalism we used to the study of SN ejecta, described in Section 2.1.
Following Fig 3.3, we start just after the shock with all the atoms in their ionised form in the hot post-shock region. The high temperature ($\geq 10^6$ K) and the UV flux irradiating from this region to the still unshocked gas ensure that all atoms are ionised and all molecules and dust clusters are destroyed (Borkowski & Shull, 1990; Docenko & Sunyaev, 2010).

Abundances for the prevalent molecules that form in the PIR are shown in Figure 3.4 for a 200 km s^{-1} shock. Molecules reform immediately in the cooling photoionised region. The gas number density in this region, at 10^6 cm^{-3}, is lower than in the SN ejecta, making bimolecular and termolecular processes not efficient. The low temperature (1500 K) also means most reactions with activation barriers are slowed down and do not contribute to molecule formation.
The main formation processes for all molecules are radiative associations:

$$C + O \longrightarrow CO + h\nu, \tag{3.11}$$

$$O + O \longrightarrow O_2 + h\nu, \tag{3.12}$$

$$Si + S \longrightarrow SiS + h\nu, \tag{3.13}$$

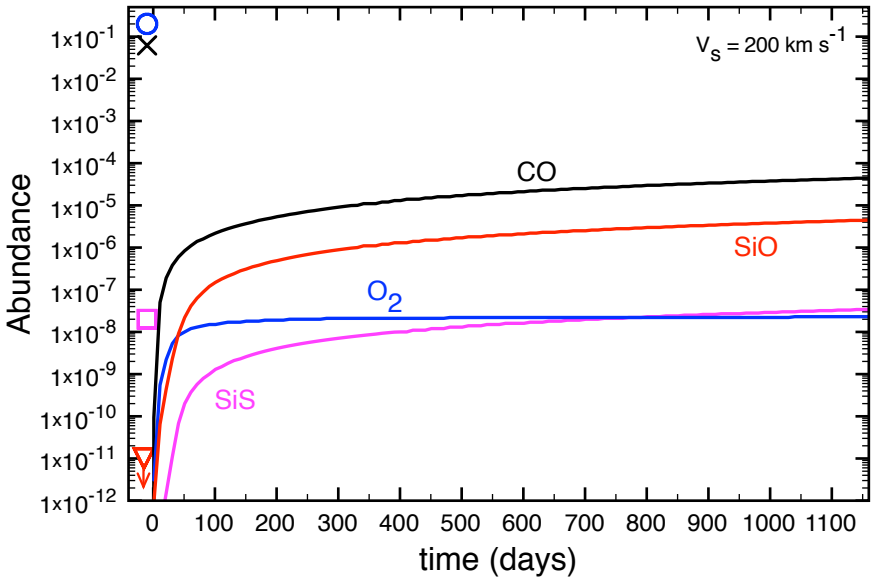

Figure 3.4: Molecules abundances in the PIR (with respect to total gas number density) for the 200 km s^{-1} shock model. The plotted symbols at $t = 0$ are abundances of molecules at 3000 days post-explosion for a number density increase of 200 (blue circle: O_2; black cross CO; pink square: SiS; red triangle: SiO). The SiO pre-shock abundance value is 1×10^{-17}. (Biscaro & Cherchneff 2014)

$$\mathrm{Si} + \mathrm{O} \longrightarrow \mathrm{SiO} + h\nu. \tag{3.14}$$

Final abundances for CO, O_2 and SiS are lower by a factor ≥ 1000 with respect to the abundances in the unshocked clump, for an increase of 200 in the ejecta gas number density.
SiO is instead at a higher abundance after the shock than before the shock, when its final abundance was around 10^{-17}. The pre-shock gas has a higher initial gas number density and temperature, and SiO is quickly depleted into clusters as soon as 500-600 days post-explosion for the 200 times enhanced number density (see Fig. 2.9), and after 1500 days for the standard density (see Fig 2.5). Figure 3.5 shows the abundances of atoms and ions for the model with a shock speed of 200 km s^{-1}. All atoms start as ions, and the only source of additional ionisation comes from oxygen photoionisation from the UV photons from the hot post-shock region. Oxygen is kept at high ionization for $\sim$ 200 days before it recombines rapidly via recombination and charge exchange reactions. The main charge exchange reactions are with with magnesium, followed by aluminium and iron. These elements keep the ionization in the PIR at ~ 0.03, owing mainly to Mg^+. We checked the importance of temperature by running the chemistry for a 200 km s^{-1} shock with a temperature of 4500 K, and the results are shown in Figure 3.6. Solid lines are the result for a temperature of 4500 K, as proposed by Borkowski & Shull (1990), while dotted lines are for our chosen temperature of 1500 K, as comparison.No major differences are present, except for a slower growth of molecules in the first days that is more pronounced in the case of O_2. This is due to recombination reactions for the main ions: for example for the carbon ion, the reaction

$$\mathrm{C}^+ + e^- \longrightarrow \mathrm{C} \tag{3.15}$$

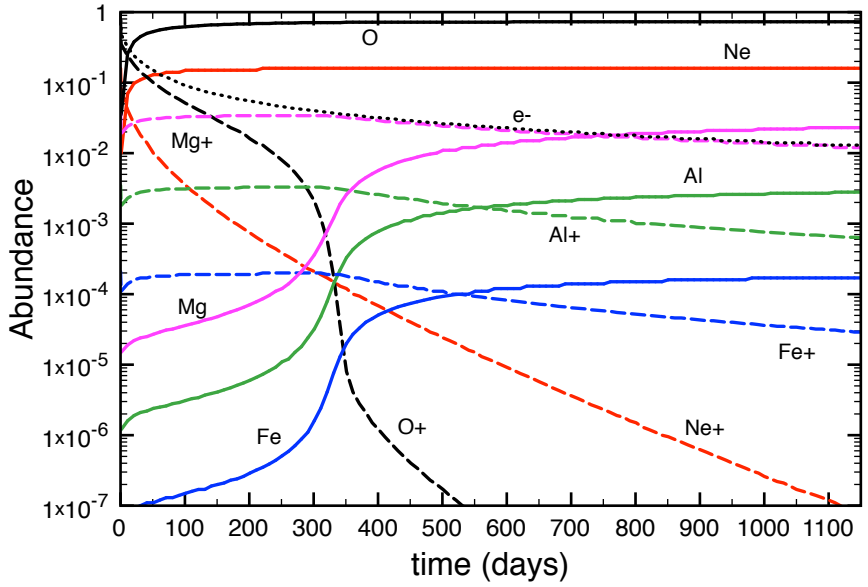

Figure 3.5: Atoms and ions abundances in the PIR (with respect to total gas number density) for the 200 km s^{-1} shock model. (Biscaro & Cherchneff 2014)

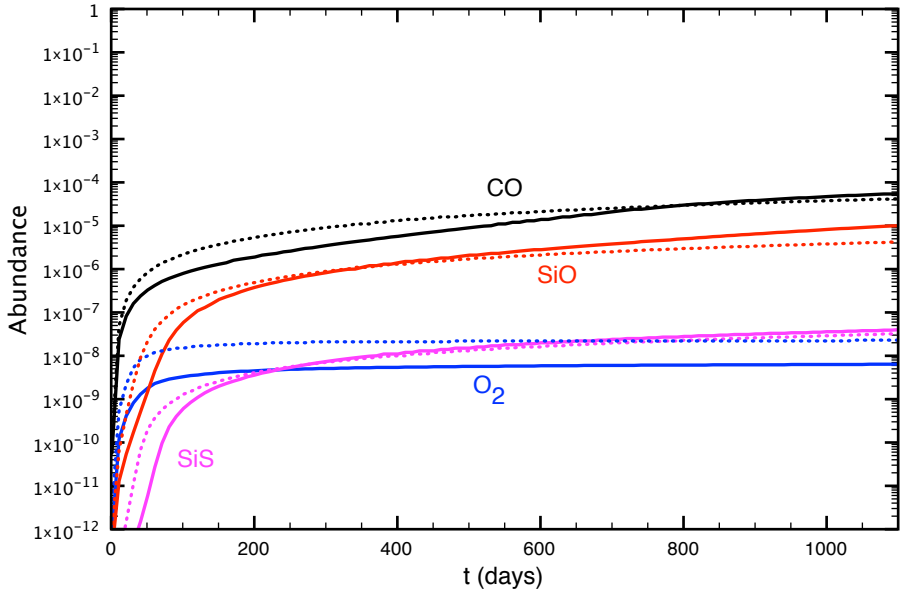

Figure 3.6: Comparison of molecules abundance for a temperature of 4500 K (solid lines) and 1500 K (dotted lines). The shock speed is 200 km s^{-1}

has a temperature dependence that makes its rate smaller at high temperatures. The presence of more carbon ions makes the ion-molecule destruction reaction with O_2 more important

$$C^+ + O_2 \longrightarrow C + CO, \tag{3.16}$$

leading to a slower growth of the O_2 molecules in the first days, when the ionization is

at its maximum. Similar reactions are efficient for CO, since the reduced rate of oxygen ions recombination

$$O^+ + e^- \longrightarrow O \tag{3.17}$$

leads to more charge exchange in the form of

$$O^+ + CO \longrightarrow CO^+ + O. \tag{3.18}$$

The final molecule abundances at the end of the PIR region are anyway very similar, and also their time dependence follows very similar curves, so we choose to use only the temperature of 1500 K for all the high velocity shocks.

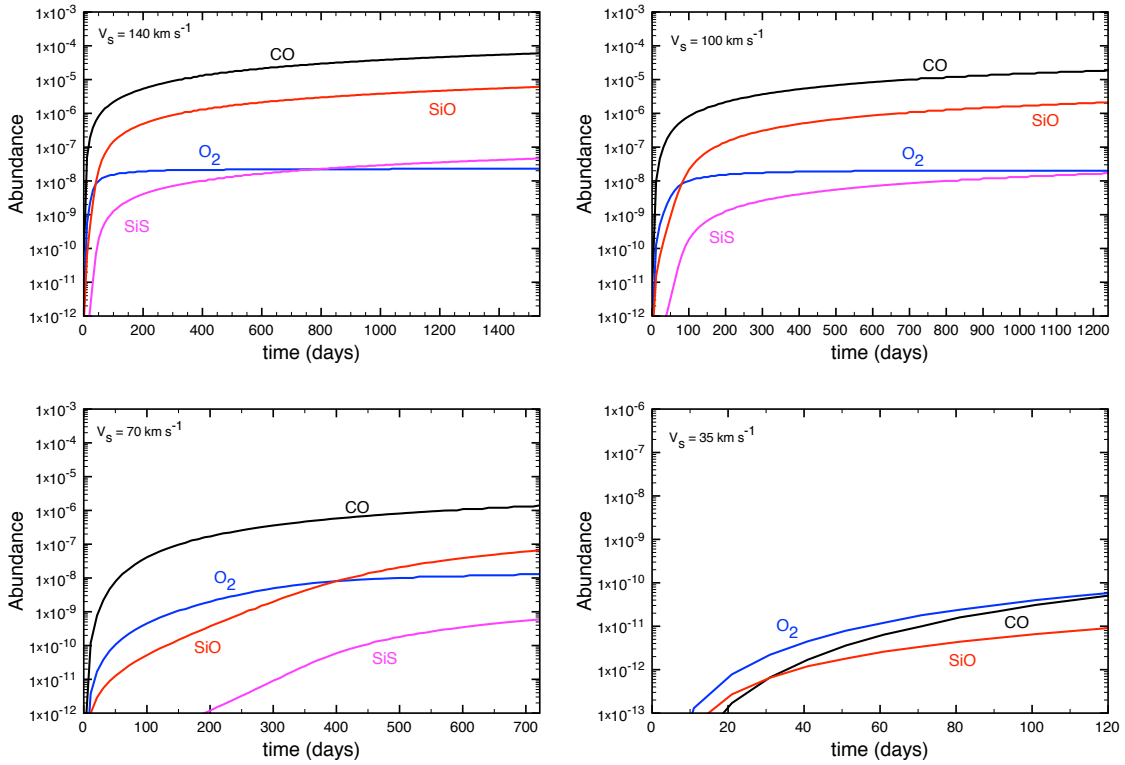

Figure 3.7: Molecules abundances in the PIR (with respect to total gas number density) for various shock velocities. Top left: 140 km s^{-1}; Top right: 100 km s^{-1}; Bottom left: 70 km s^{-1}; Bottom right: 35 km s^{-1}. (Biscaro & Cherchneff 2014)

Molecules abundances for the other shock velocities are shown in Figure 3.7. From Eq. 3.6 and Table 3.1 we derive the PIR duration that we used in our models, with slower shocks leading to a shorter duration of the PIR region. From Eq. 3.7 we derive that the gas number density is lower for slower shocks. The models with shock velocity of 140 km s^{-1} or 100 km s^{-1} have gas number density and duration similar to the 200 km s^{-1} one, with results that exhibit similar trends.
CO is always the most abundant molecule to form, followed by SiO and O_2, with the exception of the slower shock, at 35 km s^{-1} that forms very low abundances of CO and O_2 with the same abundances. The main formation processes are the same as in the 200 km s^{-1} case, with molecules formed by radiative association reactions and destroyed by charge exchanges and ion-molecule reactions. As for the SN ejecta case, a higher gas num-

ber density leads to a greater chemical complexity.

It is of interest to check the possibility of reforming dust from the gas phase after the passage of the shock. The gas in the photoionised region is re-heated by the shocks and contracts to relatively high density after it starts to cool down. This activates again an active gas chemistry, but for dust to condense, dust clusters need to emerge from the gas phase chemistry. In all our post-shock models, dust clusters are able to reform only in negligible quantities, with abundances $\leq 10^{20}$, because of the low gas number density in the PIR and the relatively short duration of the PIR. We explore the possibility of

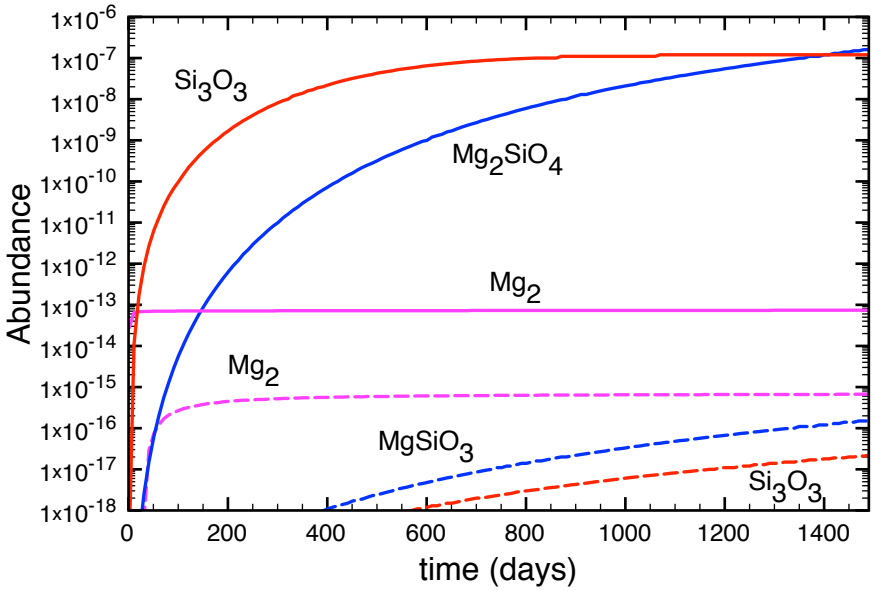

Figure 3.8: Abundances of dust clusters in the PIR (with respect to total gas number density) for the 140 km s^{-1} reverse shock. Dashed lines and full lines are for a gas number density of 10^7 cm^{-3} and 10^9 cm^{-3}, respectively. (Biscaro & Cherchneff 2014)

synthesising dust clusters by artificially increasing the gas number density in the PIR for the 140 km s^{-1} model. We consider two PIR enhanced densities, 10^7 cm^{-3} and 10^9 cm^{-3}, and results are presented in Figure 3.8.
For a number density increase of one order of magnitude, to 10^7 cm^{-3}, only small quantities of enstatite and (SiO) trimers form from the gas phase. Their abundances are very low, $\sim 10^{-16}$ and $\sim 10^{-17}$, respectively. Mg_2 is the most abundant cluster, with an abundance of $\sim 10^{-15}$. Increasing the gas number density of a further two orders of magnitude, to 10^9 cm^{-3}, leads to the formation of forsterite and of larger amounts of (SiO) trimers and Mg dimers. These abundances are $\leq 10^{-7}$, and not high enough to permit dust condensation from the gas phase dust clusters.
The PIR corresponds to a region where both the gas temperature and number density are high compared with values characterising the pre-shock gas in the clump and non-shocked gas in the remnant. This environment is thus more conducive to dust cluster formation from the gas phase. If dust clusters are unable to form from the gas phase in this region, we can then anticipate that the dust grains destroyed by the reverse shock crossing dense gas clumps are unable to reform in the remnant from the gas phase.

In Figure 3.9 we investigate whether the duration of the photoionised zone has any impact on molecule and dust cluster formation. The characteristic time for a shock to

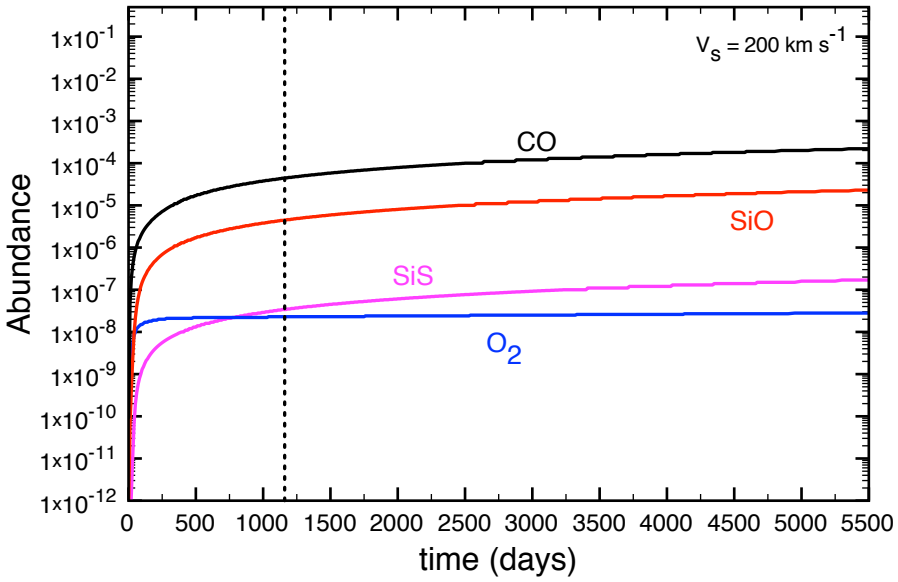

Figure 3.9: Abundances of molecules (with respect to total gas number density) as a function of time in the post-shock region of the 200 km s^{-1} RS. The vertical dotted line indicates $t = t_{PIR}$. (Biscaro & Cherchneff 2014)

cross the clump is

$$\tau_{cc} = \frac{\chi^{1/2}}{v_{shock}}, \tag{3.19}$$

where the time τ_{cc} is called cloud-crushing time, v_{shock} is the shock velocity and χ the density contrast between clump and interclump material (Klein et al., 1994). Typical cloud-crushing times for χ between 100 and 1000 and shocks velocities in the interclump gas between 1000 and 5000 km s^{-1} range from 6 to 100 years (Silvia et al., 2010). After $\sim 3 \times \tau_{cc}$, the clump will be completely disrupted and the molecules and dust will be released into the hot interclump gas (Silvia et al., 2010). We thus consider the reverse shock model with $v_{shock} = 200$ km s^{-1}, keep the PIR number density constant over a period of ~ 15 years, and decrease the gas temperature to 300 K to account for radiative cooling. The abundances of the prevalent molecules are shown in Figure 3.9. Most molecules slowly keep forming from radiative association processes while dust clusters abundances stay below 10^{-20}. The final abundance values for molecules at τ_{cc} remain all below 10^{-3} for $6 < \tau_{cc} < 100$ years. Only CO reaches 10^{-4}, while the other molecules are at least an order of magnitude less abundant.

We can thus conclude that molecules quickly reform in the dense and warm PIR region and continue forming in the post-reverse shock gas till $t = \tau_{cc}$. We also confirm that dust clusters are unable to form from the gas phase in the PIR and at later times in the shocked clump.

For all the shock velocities considered, our chemical kinetic models of the gas phase are unable to reform dust clusters. Since dust condensation needs a non negligible abundance of dust clusters to act as seeds, not dust grains are able to reform in the post-shock gas in oxygen rich clumps, even at increased densities. We thus conclude that the dust budget of the remnant relies entirely on the dust formed in the ejecta, and on its ability to survive the passage of the reverse shock.

4. Observations of shocked gas in Cas A with *Herschel*

4.1 An overview of the space telescope *Herschel*

The Herschel Space Observatory is a space observatory, active from 2009 to 2013, specifically designed to observations in the far infrared and submm wavelengths. As such, it is particularly useful in observing cold and/or dusty objects, and as a result in investigating molecular chemistry.
Herschel is equipped with a 3.5 m mirror made of sintered silicon carbide and three detectors: PACS (Photodetecting Array Camera and Spectrometer), SPIRE (Spectral and Photometric Imaging Receiver) and HIFI (Heterodyne Instrument for the Far Infrared). The detectors are cooled with liquid helium in order to be kept at their operational temperature, giving the spacecraft a lifetime limit of three to four years.

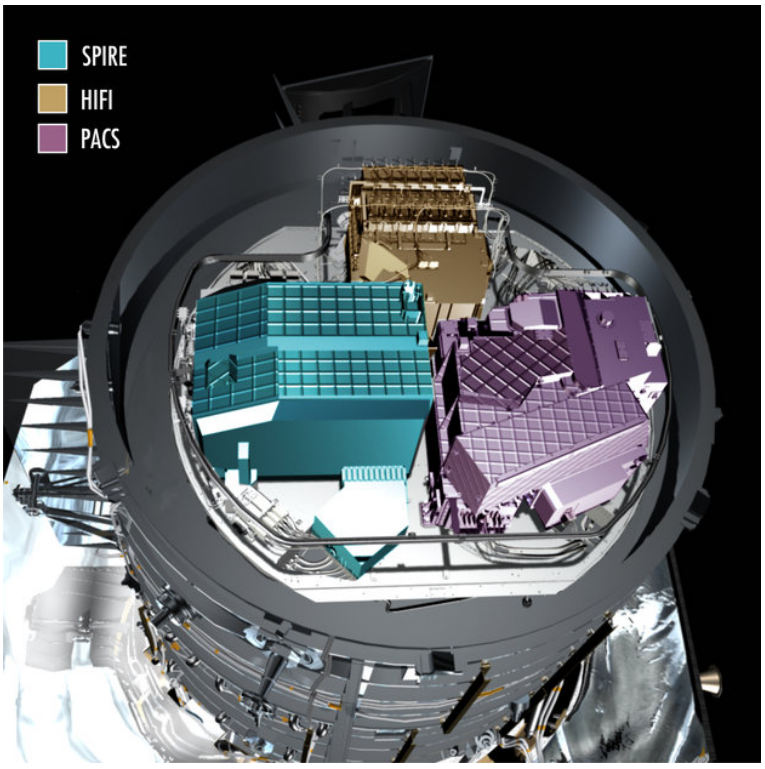

Figure 4.1: Diagram of Herschel instrument inside the spacecraft. From esa.int

PACS is a low resolution imaging spectrometer and operates in the range 55-210 μm. It can operate as a photometer in two colours, or as a spectrometer. In photometry mode, it can measure fluxes over a field of view of $\sim$ 1.75' x 3.5', in two bands simultaneously,

60-85 μm or 85-125 μm and 125-210μm. In spectroscopy mode it can capture spectra in a field 47" x 47" with a spectral resolution of 175 km s^{-1}. SPIRE also consist of a camera and an imaging spectrometer, but covers wavelengths in the range 194-672 μm. It is designed to study star formation history. HIFI is a high resolution spectrometer, and covers two bands: 157-212 μm and 240-620 μm. Its main objective were the study of comets, planetary atmospheres, star formation and galaxy development.
For this observation we used the Photodetector Array Camera and Spectrometer (PACS, Poglitsch et al. (2010)), which consists of a 5x5 array of spatial pixels (spaxels), each in size 9.4"x 9.4", with a detection limit of a few millijanskys. The data were taken on June 11th, 2002, using short range spectroscopy scans with high spectral resolutions, with the aim to observe a single knot in the northwest part of Cas A (see Figure 4.2). We targeted seven CO rotational transitions, between J=14 and 38, using short range spectroscopy scan with high spectral resolution.

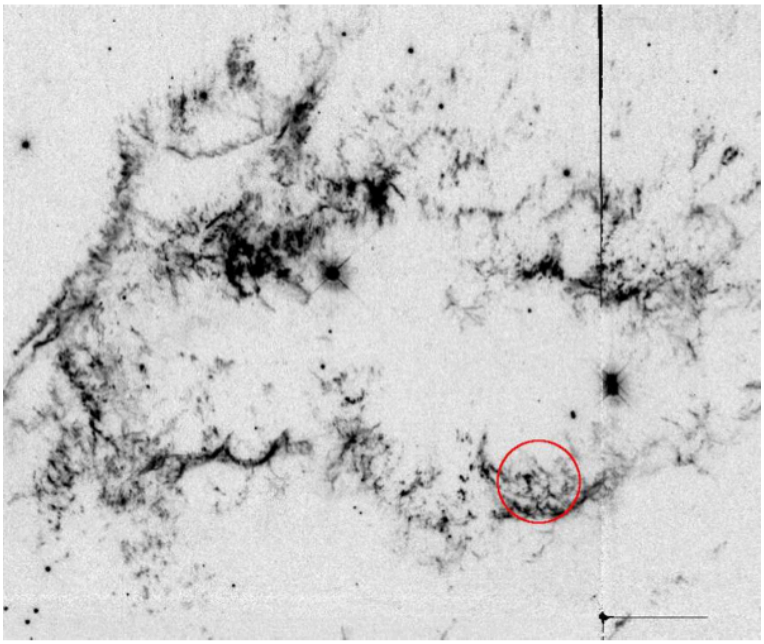

Figure 4.2: HST O III-filter image of the northern part of Cas A, the targeted position is shown with a red 9.4" circle.

4.2 CO line emission in Cas A clumps

The Herschel PACS instrument detected 6 CO lines and a bright OIII line, between 67 and 211 μm. All the targeted lines were detected, but the J=38-37 spectrum was discarded due to a presence of an artifact in the detected flux.
The assumed knot dimension is 0.5", derived from Fesen et al. (2001), which suggest a knot size between 0.2" and 0.6", and Rho et al. (2009a), which put an upper limit of 0.8" from near-IR roto-vibrational CO source.
These data are reproduced in Figure 4.3, already reduced, and were then analysed for an estimation the column density and the excitation temperature. The column density is defined as the number of a substance per unit area integrated along a path, according to the equation

$$N = \int nds. \tag{4.1}$$

The excitation temperature T_{ex} is the temperature that appears in the Boltzmann equation

$$\frac{n_u}{n_0} = \frac{g_u}{g_0} exp(-\Delta E/kT_{ex}), \tag{4.2}$$

where n_u and n_0 are the number of particles in the upper and lower state, respectively, and g_u and g_0 their statistical weights.

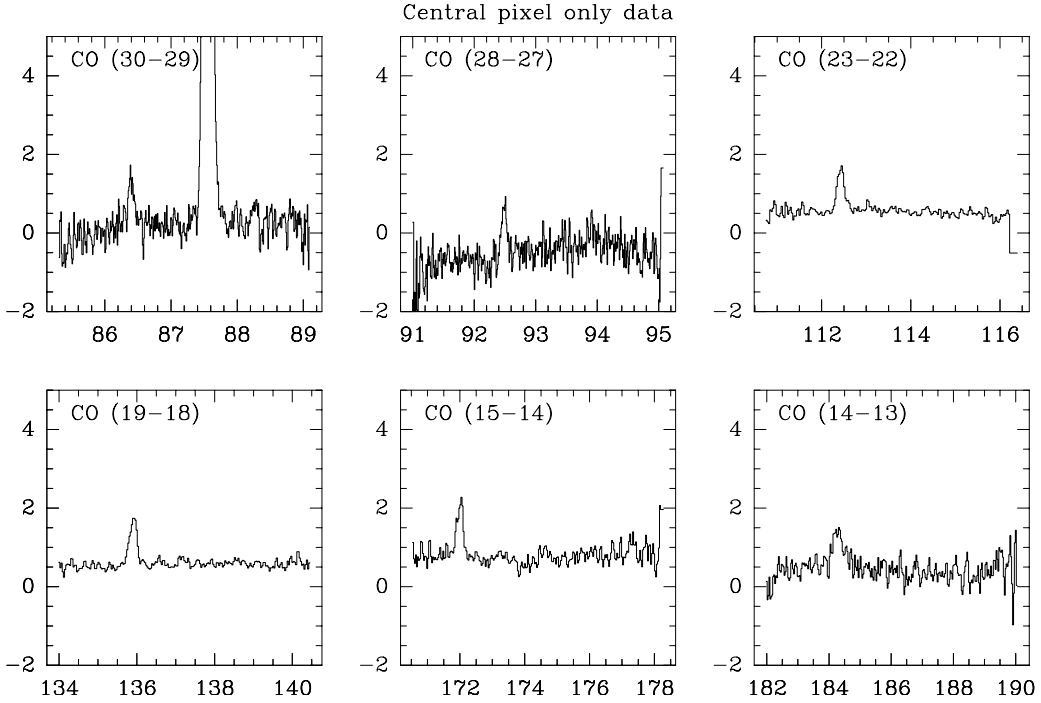

Figure 4.3: Original data from the central pixel, continuum subtracted. The bright line around 88μm is O III. The y axis is in Jy/pixel.

For deriving the total column density and the excitation temperature we first fit each line with a Gaussian profile: this gives for each line the intensity I, the frequency of the line ν and the full width half maximum of the line.
The results of our fits are reported in the table 4.1 for all the six CO lines, while the fits of the velocity profiles are showed in Figure 4.4 The intensity then scales with the column density of the upper level, N_u, according to:

$$I = \frac{A_{ul} N_u h \nu_{ul}}{4\pi}, \tag{4.3}$$

where A_{ij} are the Einstein coefficient for the transition ij, ν_{ij} is the frequency of the transition, and h is the Plank constant. Once obtained the column density, is then possible to use the Boltzmann equation in the form:

$$\frac{N_u}{N_0} = \frac{g_u}{g_0} exp(-E_u/kT_{ex}), \tag{4.4}$$

Transition	Wavelength (μm)	v (km s^{-1})	δv (km s^{-1})	$\int$Flux dv (Jy/pix km s^{-1})
14-13	186.00	-2882(370)	661(63)	555(49)
15-14	173.63	-2814(362)	336(24)	447(38)
19-18	137.20	-2814(336)	409(19)	562(23)
23-22	113.46	-2716(309)	372(19)	366(24)
28-27	93.35	-2765(105)	292(32)	594(33)
30-29	87.19	-2733(470)	418(46)	663(52)
O III	88.36	-2701(100)	341(7)	11615(176)

Table 4.1: Central pixel only, gauss-fits to the lines. v is the radial velocity of the line, and δv the velocity full width at half maximum. Errors are given in parentheses.

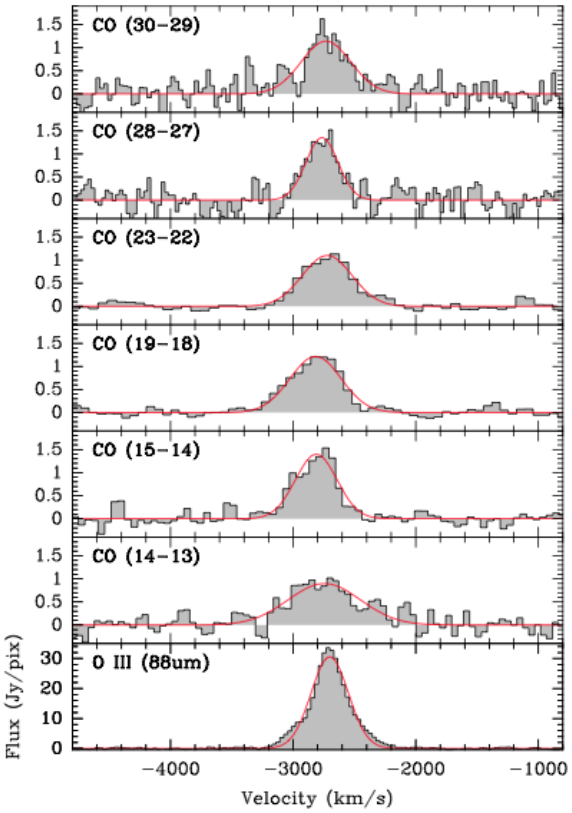

Figure 4.4: CO, and O III, emission lines in velocity, with gauss fits, extracted from the central PACS spaxel. (Wallström et al., 2013)

where N_0 is the column density in the lower level and T_{ex} is the excitation temperature. We can then plot the column density versus the energy and derive N_0 and T_{ex} from the intercept and the slope of the fit, respectively. The total column density is then obtained using:

$$N_{tot} = N_0 \frac{kT_{ex}}{hcB}, \tag{4.5}$$

where k is the Boltzmann constant, c is the speed of light and B is the rotational constant for the molecule considered, defined as

$$B = \frac{h}{8\pi^2 cI}, \tag{4.6}$$

where $I = \Sigma_i m_i r^2$ is the moment of inertia of the molecule. The factor $\frac{kT_{ex}}{hcB}$ is an approximation of the partition function $Q(T_{ex})$, defined as

$$Q(T_{ex}) = \Sigma_i g_i exp(-E_i/kT_{ex}), \tag{4.7}$$

and counts the weighted number of states a system can occupy.

Figure 4.5 (Wallström et al., 2013) is the resulting rotational diagram for the detected CO lines, which gives as result a total column density of $4.12 \pm 0.32 \times 10^{17} cm^{-2}$ and an excitation temperature of $560 \pm 18K$. From the definition of column density is possible

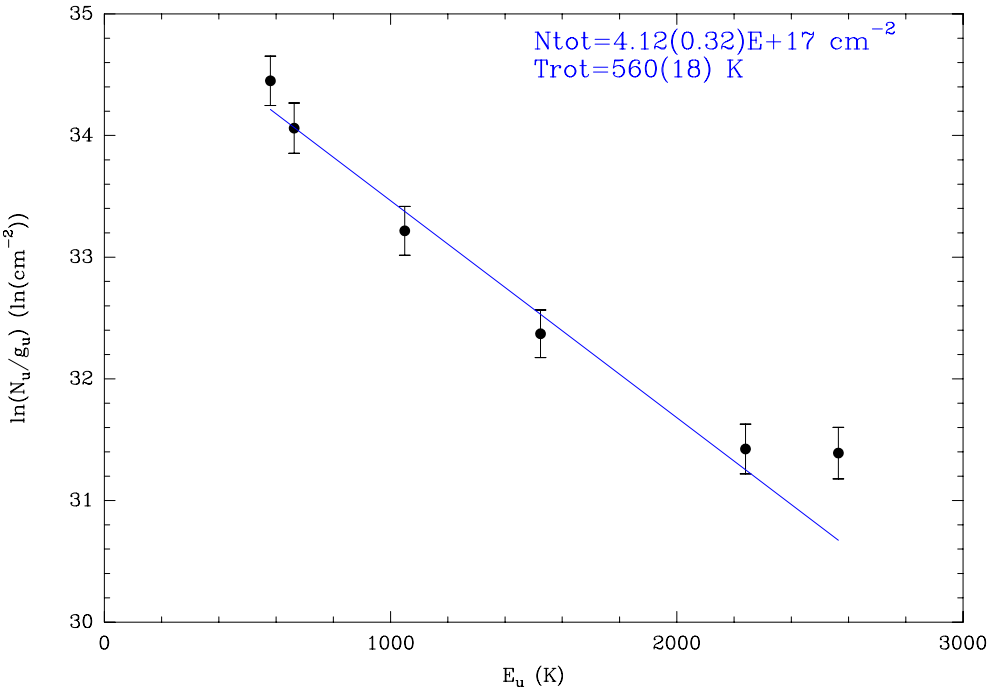

Figure 4.5: Example of the rotational diagram obtained with CO lines detected in Cas A

to calculate the mass of CO observed if the area of the observed region is know. The definition of column density is N_{tot}= number of atoms(molecules)/area. Since we have the angle under which the source is observed, from trigonometry we have

$$tg(\alpha) = z/x, \tag{4.8}$$

where α is the angle, z and x are the dimension and the distance of the source, respectively. In our case the distance is the distance of CasA, estimated of 3.4 kpc, and α is the knot dimension of 0.5". Is then straightforward to calculate the area, and then use the definition of column density to have

$$M_{CO} = N_{CO} A m_{CO}, \tag{4.9}$$

where M_{CO} is the total CO mass, N_{CO} is the CO column density, A is the area of the source and m_{CO} is the mass of a single CO molecule. With the column density calculated

above, we obtain a mass of $\sim 5 \times 10^{-6} M_{\odot}$ for the CO in the knot.
The results obtained with the rotational diagram are valid in LTE (Local Thermal Equilibrium), which assumes that the level populations are governed by the Boltzmann equation and are independent of the radiation field. This is probably not the case here, since the observed knot is located in a region which is being traversed by the reverse shock, requiring a non-LTE analysis. We carried out this investigation with the non-LTE transfer code RADEX (van der Tak et al., 2007), assuming a constant density, temperature and abundance in the region of interest.
Due to the presence of a bright oxygen line and multiple CO lines, the knot is supposed to be rich in oxygen, which will then be the main collision partner in the transfer code. However, there are no studies that provide collisional rates of CO with oxygen, so we used H, H_2 and H_2O as collision partner. The RADEX non-LTE analysis is in substantial agreement with the rotational diagram, with a resulting column density for CO, $N_{CO} \sim 10^{17} \mathrm{cm}^{-2}$ and two temperature components, one at 400 K, the other at $\sim$ 2000 K. This additional hot component is needed to fit all the observed rotational lines, as well as other observed ro-vibrational CO lines from the same region (Rho et al., 2009a, 2012). Result of the fit are showed in Figure 4.6 (Wallström et al., 2013).

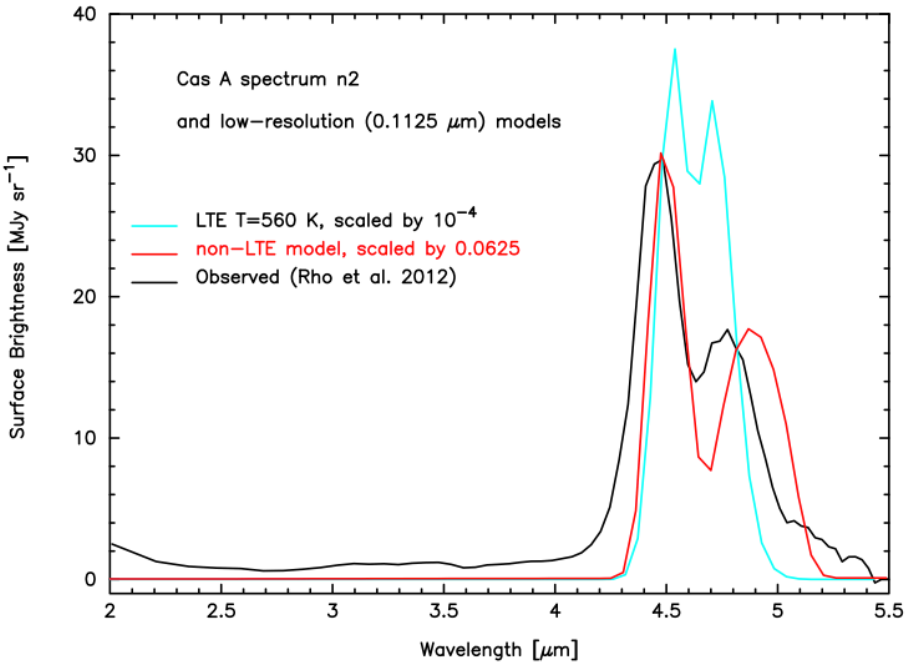

Figure 4.6: The mid-IR AKARI spectrum reported by (Rho et al., 2012) for knot n2 in Cas A is compared with a LTE and non-LTE models. The computed spectra include more than 4000 vibration-rotation lines, each of which has a width of 415 kms^{-1}. (Wallström et al., 2013)

The densities and temperatures found after the non-LTE analysis are in agreement with the framework of a clump that is being shocked by the reverse shock, and thus has high density and two different temperatures, corresponding to the freshly shocked material (high temperature) and the cooled-down, recombined clump some times after the shock, as described in Section 3.

5. Dust processing by the reverse shock

Dust destruction plays an important role in SNRs. The dust formed in the ejecta is processed by the remnant reverse shock, causing grain destruction both by thermal and non-thermal processes. There are several possible processes that are active on dust grains: grain disruption and destruction processes (Jones et al., 1996). Grain disruption is caused by shattering due to grain-grain collisions. This process reduces the size of a grain but does return material from the grain to the dust phase.
Grain destruction processes include vaporization and sputtering. Vaporization is the total destruction of a grain after a collision with another grain. Sputtering is instead caused by impacts between grain and gas, and leads to the removal of atoms or molecules from the surface of the grain. Sputtering may be thermal, i.e. caused by the thermal motion of the hot gas, or non thermal, i.e. caused by high relative velocity between gas and dust grains. Since the number density of dust grains in the post-reverse shock is small, the processes that involve grain-grain encounters are suppressed, and can be ignored. In this model, we concentrate on non-thermal and thermal sputtering, which are the most important processes in the context of fast, non radiative shocks, such as the reverse shocks in SNRs.

5.1 Sputtering theory and model

The sputtering yield is defined as the average number of sputtered atoms per incident projectile particle, and it can be derived following different approaches. One method applies the Monte Carlo code for the transport of ions in matter (TRIM, and its more recent version SRIM, Ziegler et al. (1985)). The code follows the trajectory of an energetic ion penetrating in a solid, traces the collisions and the recoils atoms, whose paths are also followed until their energy is lower than the surface binding energy or they escape the solid. This method is used by Jurac et al. (1998) and by Serra Díaz-Cano & Jones (2008) to model impacts of helium and hydrogen ions on carbon. They underline a fundamental difference in the sputtering of graphite and amorphous carbon, with the latter having sputtering yields up to three times higher the ones for graphite. There are however no specific studies on the other dust species that we are considering in the ejecta of Cas A.
Another method uses a formula for the yield at normal incidence and is derived by Sigmund (1969) using cascade theory, which follows the energy deposited in the form of recoiling atoms in the grain as well as their velocity distribution and surface transport and can be written as

$$Y(E,\mu) = \frac{0.042\alpha(\mu)S(E)\zeta(\mu,E)}{U_0}, \tag{5.1}$$

where α is an energy independent function of the ratio between target and projectile, μ, $S(E)$ is the nuclear stopping power, U_0 is the surface binding energy and ζ is a correction

factor for the energy dependence of the sputtering. For sputtering of heavy ions with energy above the threshold energy, ζ =1. Several author investigated different choices for ζ and for the sputtering threshold of various grains (Burke & Silk, 1974; Draine & Salpeter, 1979a; Dwek & Scalo, 1980; Seab & Shull, 1983). Semiempirical sputtering theories have been proposed by Bohdansky (1980); Yamamura et al. (1983).
We follow the studies of Tielens et al. (1994) and Nozawa et al. (2006). They consider sputtering by normally incident gas particles impacting on the dust grains and use the functional form of ζ and the threshold energy proposed by Bohdansky (1984). They also use experimental data for the fit of sputtering yields. For backward sputtering the sputtering yield at normal incidence $Y_i(E)$ caused by a projectile i with energy E is (Bohdansky, 1984)

$$Y_i(E) = 4.2 \times 10^{14} \frac{S_i(E)}{U_0} \frac{\alpha_i(\mu_i)}{K\mu_i + 1} \left[1 - \left(\frac{E_{th}}{E}\right)^{2/3}\right] \left(1 - \frac{E_{th}}{E}\right)^2, \tag{5.2}$$

in atoms per ion.
U_0 is the surface binding energy in units of eV, $\mu_i = M_d/M_i$ where M_d and M_i are the mass number of the target atom and of the incident ion, respectively.
The threshold energies E_{th} are approximately given by (Andersen & Bay, 1981; Bohdansky, 1984)

$$E_{th} = \begin{cases} \frac{U_0}{g_i(1-g_i)} & \text{for } M_i/M_d \leq 0.3 \\ \\ 8U_0 \left(\frac{M_i}{M_d}\right)^{1/3} & \text{for } M_i/M_d > 0.3 \end{cases}$$

where $g_i = 4M_iM_d/(M_i + M_d)^2$ is the maximum fractional energy transfer in a head-on elastic collision. $S_i(E)$ is the nuclear stopping cross section in units of ergs cm^2 and is given by Sigmund (1981)

$$S_i(E) = 4\pi a_{sc} Z_i Z_d e^2 \frac{M_i}{M_i + M_d} s_i(\epsilon_i), \tag{5.3}$$

where e is the elementary charge, Z_i and Z_d the atomic number of the incident ion and the target atom, respectively. The screening length a_{sc} for the interaction between the nuclei and is expressed as

$$a_{sc} = 0.885 a_0 (Z_i^{2/3} + Z_d^{2/3})^{-1/2}, \tag{5.4}$$

where $a_0 = 0.529$ Å is the Bohr radius. The function $s_i(\epsilon_i)$ can be approximated by Matsunami et al. (1980)

$$s_i(\epsilon_i) = \frac{3.441\sqrt{\epsilon_i} ln(\epsilon_i + 2.718)}{1 + 6.35\sqrt{\epsilon_i} + \epsilon_i(6.882\sqrt{\epsilon_i} - 1.708)}. \tag{5.5}$$

The reduced energy ϵ_i is given by

$$\epsilon_i = \frac{M_d}{M_i + M_d} \frac{a_{sc}}{Z_i Z_d e^2} E. \tag{5.6}$$

The value of $\alpha_i(\mu_i)$ depends on the approximation of the distribution of energy deposited in the target. From the first approximations made in Sigmund (1969) and Bohdansky (1984), Nozawa et al. (2006) derive a more precise formula from comparison with sputtering data for $0.3 \leq \mu_i \leq 56$

$$\alpha_i = \begin{cases} 0.2 & \text{for } \mu_i \leq 0.5 \\ 0.1\mu_i^{-1} + 0.25(\mu_i - 0.5)^2 & \text{for } 0.5 < \mu_i \leq 1 \\ 0.3(\mu_i - 0.6)^{2/3} & \text{for } 1 < \mu_i \end{cases}$$

The value of K is determined by Nozawa et al. (2006) and Tielens et al. (1994) by

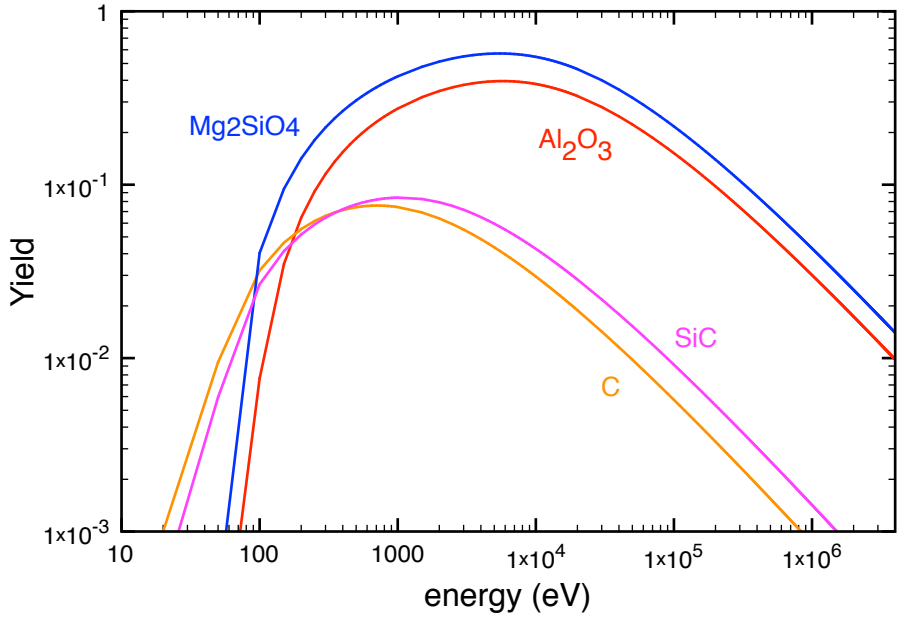

Figure 5.1: Yields for the dust species considered. Forsterite and alumina are for impact by O^+, Carbon and Silicon Carbide for impacts by He^+

fitting experimental data for the sputtering yield of the gas species, when available, and by fitting simulated data for the grains for which no yield data were available. For alumina, carbon and silicon carbide, experimental data are available and used in the fitting (see Table 5.1).

Dust Species	U_0(eV)	M_d	Z_d	K	References
Mg_2SiO_4	5.7	20	10	0.1	8
Al_2O_3	8.5	20.4	10	0.08	3, 6, 7
SiC	6.3	20	10	0.3	1, 9, 3
C	4.0	12	6	0.61	1, 2, 3, 4, 5

Table 5.1: Parameters used in the Yield formula. REFERENCES: (1) Bohdansky et al. (1978); (2) Roth et al. (1976); (3) Roth et al. (1979); (4) Rosenberg & Wehner (1962); (5) Hechtl et al. (1981); (6) Bach (1970); (7) Nenadović et al. (1990); (8) Tielens et al. (1994); (9) Behrisch et al. (1976)

Forsterite has no sputtering data available in the literature, so we followed the approach of Tielens et al. (1994). In their study, they assume a fitting constant K equal to 0.1, as calculated for SiO_2, and considered representative of silicates in general. The binding energy is an average adopted in studies of sputtering of interstellar silicates (Jones et al., 1994).

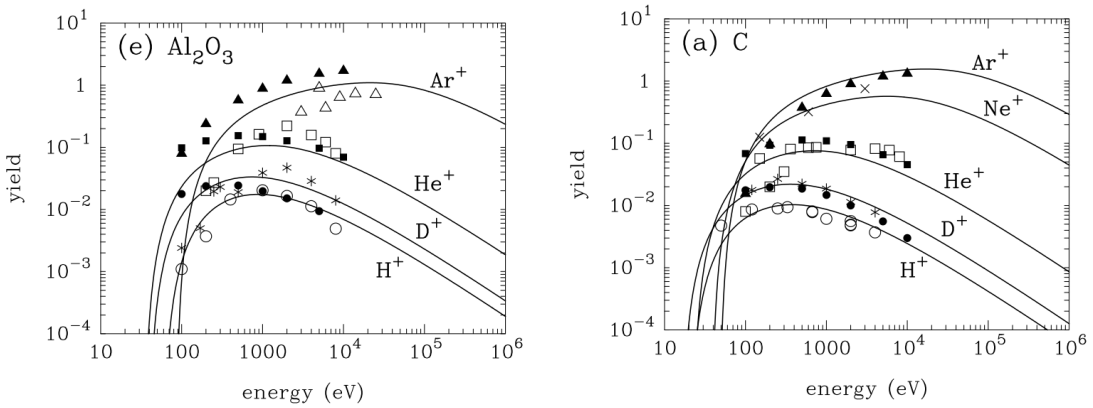

Figure 5.2: Comparison of calculated sputtering yields and experimental values for Al_2O_3 and C. Nozawa et al. (2006)

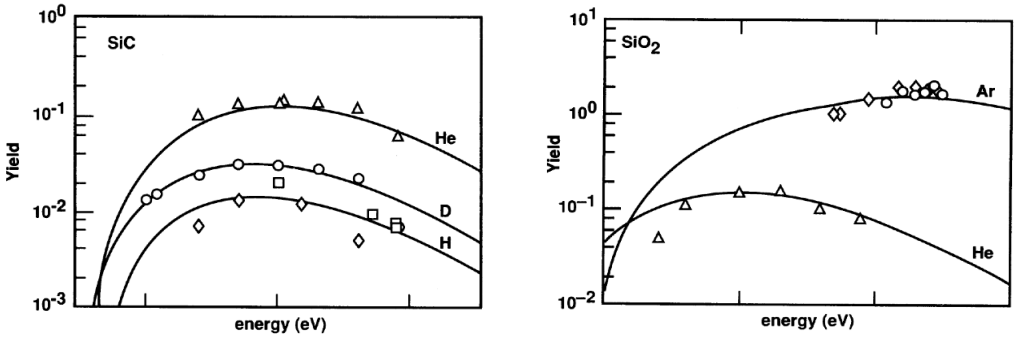

Figure 5.3: Comparison of calculated sputtering yields and experimental values for SiC and SiO_2. Tielens et al. (1994)

The yields for the species considered are plotted in Figure 5.1. We choose the impacting ion according to the chemical composition of the zone where the dust grains form. Forsterite and alumina form in the oxygen rich zones, where the most abundant ion is O^+, followed by Mg^+, while carbon and silicon carbide form in the outer zone, which is rich in He^+.

5.1.1 Non-thermal sputtering

Non-thermal sputtering becomes important when the relative velocity of the dust grains with respect to the gas is ≥ 100 km s^{-1} (see Figure 5.4). Thus, this case applies to the immediate postshock region after the passage of the reverse shock in the SNR, since the shock velocity is ≥ 200 km s^{-1} and the initial velocity relative to gas is $v_d \simeq 3/4V_{sh}$, where V_{sh} is the shock velocity. The relative velocity of dust grains with respect to gas arises because dust grains move ballistically behind the shock, while gas is decelerated owing to the conservation of mass flux, expressed as $v_g = 1/4V_{sh}$, where v_g is the gas velocity and 1/4 is ratio of the densities before and after a strong shock. A fast grain travelling through the highly-ionized postshock gas will thus be eroded and slowed down, until eventually its relative velocity will approach zero and the non-thermal sputtering will cease to affect the grains.
If we assume that all the gas species are at the same temperature and the dust grain is spherical with radius a, then the deceleration rate is given by (Draine & Salpeter, 1979b)

$$\frac{dv_d}{dt} = -\frac{3nkT}{2a\rho_d} \sum_i A_i G_i(s_i), \tag{5.7}$$

where n is the number density of the gas, k the Boltzmann constant, T the gas temperature, ρ_d the bulk density of the grain, and A_i the number abundance of gas species i relative to the gas. The quantity s_i is expressed as

$$s_i^2 = \frac{m_i v_d^2}{2kT}, \tag{5.8}$$

where m_i is the mass of gas species i. We use the analytical approximation for $G_i(s_i)$ proposed by Draine & Salpeter (1979b)

$$G_i(s_i) \approx \frac{8s_i}{3\sqrt{\pi}} \left(1 + \frac{9\pi}{64} s_i^2\right)^{1/2}. \tag{5.9}$$

This approximation is accurate within 1% for 0<s< ∞ and it's derived assuming the grain radius is negligible compared to the mean free path of gas particles, collisions are completely inelastic, and Coulomb focusing of ions may be neglected

The erosion rate of grains is given by the angle-averaged sputtering yield

$$\langle Y_i(E) \rangle_\theta = 2Y_i(E), \tag{5.10}$$

and can be written as (Dwek et al., 1996)

$$\frac{da}{dt} = -\frac{m_{sp}}{2\rho_d} n \sum_i A_i \left(\frac{8kT}{\pi m_i}\right)^{1/2} \frac{e^{-s_i^2}}{2s_i} \int \sqrt{\epsilon_i} e^{-\epsilon_i} sinh(2s_i\sqrt{\epsilon_i}) Y_i(\epsilon_i) d\epsilon_i, \tag{5.11}$$

where $\epsilon_i = E_i/kT$ and m_{sp} is the average mass of the sputtered atoms.

The erosion rate for a hypersonic grain eroded by non-thermal sputtering can be simplified as (Dwek & Arendt, 1992; Tielens et al., 1994)

$$\frac{1}{n}\frac{da}{dt} = -\frac{m_{sp} v_d}{2\rho_d} \sum_i A_i Y_i (E = 0.5 m_i v_d^2). \tag{5.12}$$

Figure 5.4 shows the erosion rates for our dust species from Eq. 5.12 in units of μm yr^{-1}

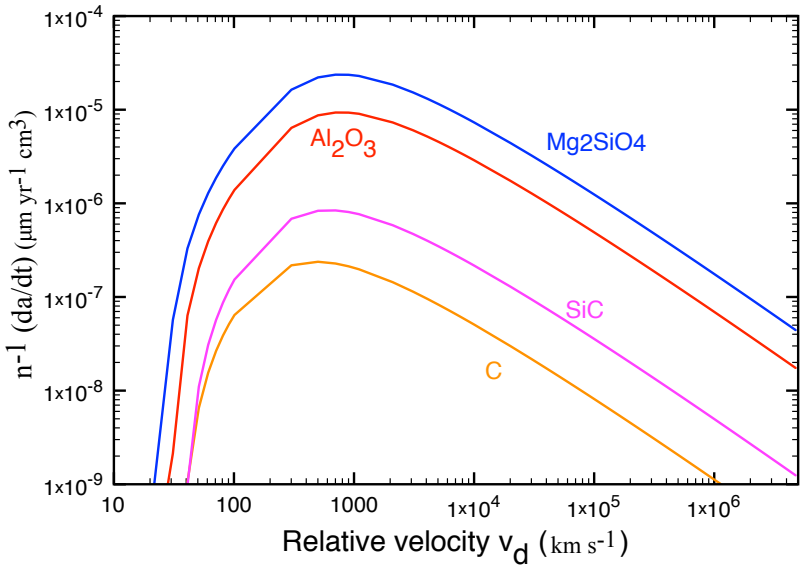

Figure 5.4: Erosion rate of dust species by non-thermal sputtering.

cm^3 as a function of relative velocity v_d.
Each dust species is eroded according to the chemical composition of the zone from which it originates, with the most abundant element(s) taken as the main sputtering gas species. Carbon and SiC form in the external layer, and are thus eroded by He^+, while forsterite and alumina, which form in the oxygen-rich zone, are eroded by O^+ and Mg^+.
Of the dust species considered, carbon and silicon carbide have the lowest erosion rates, owing to their lower sputtering yields and their sputtering by He^+, which is lighter compared to O^+. Forsterite has the highest erosion rate, due to its material fragility and the impact with heavy ions. The highest erosion rate for all species is for a relative velocity comprises between ∼200 km s^{-1} and ∼ 800 km s^{-1}, with a steep decrease for higher and lower velocities. Non-thermal sputtering becomes negligible for relative velocities lower than 50 km s^{-1}.

5.1.2 Thermal sputtering

Thermal sputtering becomes important as the gas temperature exceeds $\geq 10^5$ K (see Figure 5.5). Temperatures between 10^5 and 10^6 K are only reached for ∼ 10 days in the hot postshock region, where the low gas number density (∼ 4 cm^{-3}) makes sputtering negligible. Dust grains in clumps are thus only sputtered by non-thermal processes. Hydrodynamical simulations of shocked clumps in SRNs show that a reverse shock with velocity between 1000 and 5000 km s^{-1} is able to disrupt clumps with an overdensity factor of 100 or 1000 in a time scale of the order of ∼ 3 $\times\tau_{cc}$, where τ_{cc} is the cloud crushing time defined in Eq. 3.19 (Silvia et al., 2010, 2012).
The eventual clump disruption releases dust grains into the less dense but hotter shocked

ejecta. We model the thermal sputtering of grains in the interclump medium as a way to assess the reprocessing of grains after the clump disruption.

The erosion rate for a stationary grain eroded by thermal sputtering is derived from eq.(5.11) as (Dwek & Arendt, 1992; Tielens et al., 1994)

$$\frac{1}{n}\frac{da}{dt} = -\frac{m_{sp}}{2\rho_d}\sum_i A_i \left(\frac{8kT}{\pi m_i}\right)^{1/2} \int \epsilon_i e^{-\epsilon_i} Y_i(\epsilon_i) d\epsilon_i. \tag{5.13}$$

Figure 5.5 shows the erosion rates for the dust species we consider, as a function of the gas

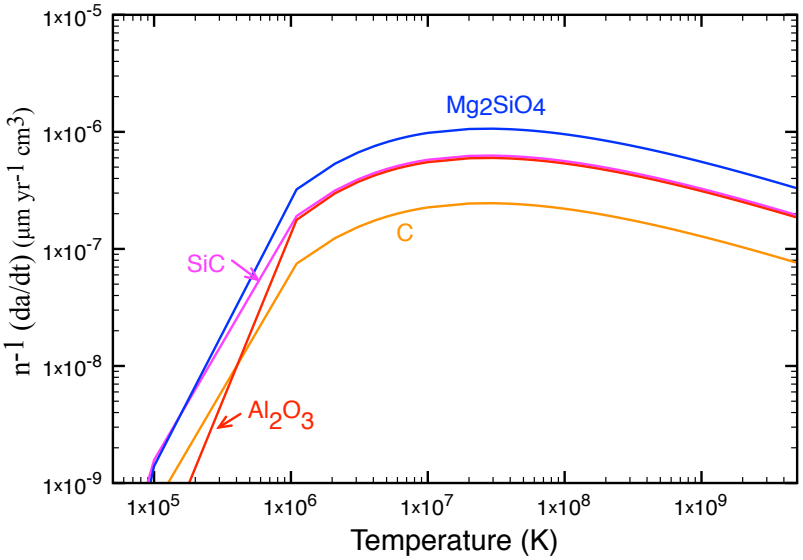

Figure 5.5: Erosion rate of dust species by thermal sputtering.

temperature T. As for non-thermal sputtering, the composition of the zone determines which sputtering gas species are used. As for non-thermal erosion rates, carbon is the species with the lowest erosion rates, apart from temperature lower than $\sim 3 \times 10^5$ K where its rate is similar or slightly higher than alumina. Forsterite is the species with the higher non-thermal erosion rate at all velocities, due to a combination of its material characteristics and of its impacts with the heavy oxygen ions. All erosion rates reach a maximum around $\sim 3 \times 10^7$K, with a fairly flat plateaux from $\sim 10^6$ K to 10^9 K where the rates are high. Below 10^6 K, thermal sputtering erosion rates decline steeply and become negligible for temperatures below 10^5 K.

5.2 Sputtering of dust in Cas A

We apply the framework above to the concrete case of clumps in Cas A. In this model, clumps are crossed by a reverse shock with velocities 200 km s^{-1}, 140 km s^{-1} and 100 km s^{-1}, and subsequently disrupted.

The grains are then released in the hot surrounding medium, while the remnant continues its expansion and the gas number density decreases according to Eq. 2.2. The gas number density influences linearly the thermal sputtering rate, so when, after $\sim$ 4000 years, its value drops below 10^{-4} cm^{-3}, the effect of sputtering on dust grains becomes negligible. This value is also consistent with the end of the Sedov-Taylor phase of the remnant, when

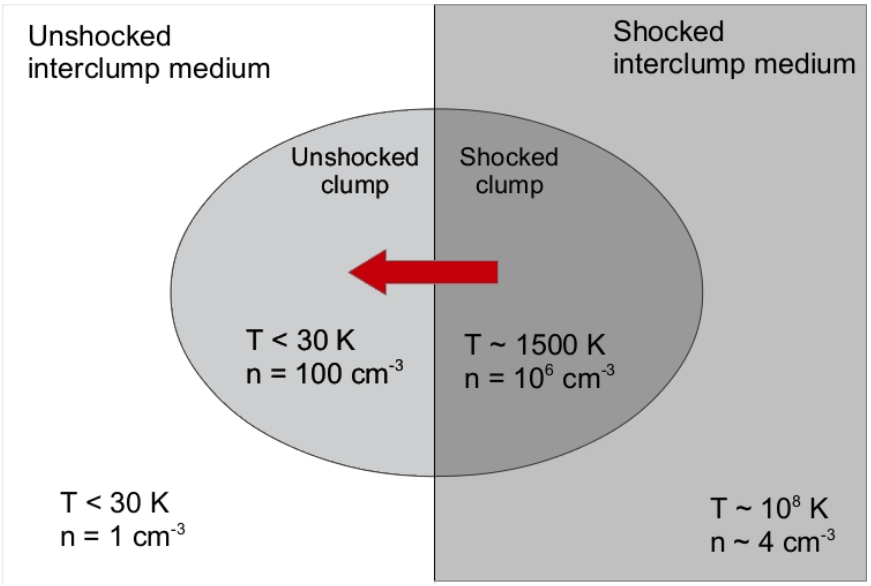

Figure 5.6: Schematic representation of a shocked clump. The reverse shock is represented by the black line at the centre of the diagram, and it is moving from right to left.

Shock velocity	Clump			Inter clump		
	Density (cm^{-3})	Temperature (K)	Duration (days)	Density (cm^{-3})	Temperature (K)	Duration (years)
200 km s^{-1}	10^6	1500	1157	4 – 10^{-4}	1×10^6 1×10^7 3×10^7 1×10^8	4000
140 km s^{-1}	10^6	1500	1537	4 – 10^{-4}	1×10^6 1×10^7 3×10^7 1×10^8	4000
100 km s^{-1}	5×10^5	1500	1241	4 – 10^{-4}	1×10^6 1×10^7 3×10^7 1×10^8	4000

Table 5.2: Parameters used in the sputtering calculations

radiative cooling becomes important and the interclump gas begins to cool down.
Dust grains in the clumps are eroded by non-thermal sputtering until the disruption of the clump. The exact amount of time necessary to destroy the clump and release the dust amounts to $\sim 3 \times \tau_{cc}$, but does not impact the results significantly. The temperature in the interclump medium stays high ($\geq 10^5$ K) for over 10^5 years (Nozawa et al., 2010), so the only sputtering parameter that is affected from changing the cloud-crushing time τ_{cc} is the number density of the interclump medium. This density is decreasing as the remnant expands, slowly decreasing the sputtering rate for several thousands years before its value becomes too low and sputtering ceases. This thousands years-long timescale for thermal sputtering means that the exact value of τ_{cc}, which is model dependent, does not result in significant changes in the final grain radii, so we assumed that the clump is disrupted after 400 years for both oxygen and carbon rich clumps, and for all shock velocities.

Hwang & Laming (2012), using CHANDRA x-ray data from Cas A, derive a temperature between 10^7 K and 3×10^7 K for the reverse shock zone. Theoretical models on the other hand predict different interclump temperatures. Silvia et al. (2010) derive an interclump temperature $\sim 10^6$ K from their hydrodynamical models of clump destruction by fast shocks. Nozawa et al. (2010) also use a similar temperature for their homogeneous model of Cas A ejecta. Micelotta & Dwek (2013) use a temperature of 10^8 K for their interclump medium in their clumpy model of sputtering in Cas A. To assess the impact of the interclump gas temperature on the results, we use temperatures between 10^6 K and 10^8 K, with a focus on 10^7 K and 3×10^7 K, since these temperatures are derived from Cas A observations. We consider two possible over-densities for clumps, as outlined in Section 3: 200 (hereafter x200) and 2000 (hereafter x2000). Both these over-densities are with respect to a homogeneous ejecta, and are both compatible with a ratio of clump/interclump number densities $20 < \chi < 200$.

5.2.1 Results of sputtering for an oxygen rich clump

We consider a clump with the chemical composition of the oxygen-rich zones that characterise the SN ejecta that led to Cas A (zones 1b and 2 of Table 2.1). Zone 3a and 3b are also oxygen rich, but their contribution to the formation of forsterite and alumina dust is several orders of magnitude lower than that of zones 1b and 2, and they are not considered here. We use as initial conditions the dust size distributions derived in Section 2.4 for a clump with a gas number density enhanced by a factor of 200 and 2000 compared with the homogeneous ejecta. We consider non-thermal sputtering in the clump for three different shock velocities and thermal sputtering in the interclump medium for four different temperatures once the clump has been disrupted by the reverse shock. The case parameters are listed in Table 5.2.

Forsterite

Figure 5.7 shows the size distribution of forsterite dust grains before and after sputtering for different shock velocities and interclump medium temperatures, for a clump with a number density enhancement of 200 with respect to a homogeneous ejecta. The plot on

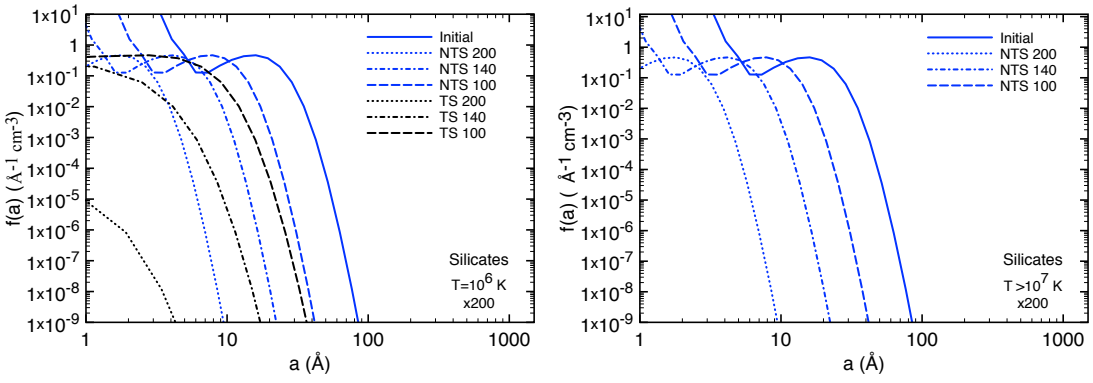

Figure 5.7: Forsterite dust grains size distribution for an interclump temperature of 10^6 K (left) and $\geq 10^7$ K (right) and shock velocities of 200 km s^{-1} (dotted lines), 140 km s^{-1} (dotted-dashed lines), 100 km s^{-1} (dashed lines) for a x200 clump. The initial size distribution is plotted with a full blue line, non-thermal sputtering with blue lines and thermal sputtering with black lines.

the left-hand side shows the change in size distribution for an interclump temperature of

10^6 K for the three considered shock velocities of 200 km s^{-1}, 140 km s^{-1} and 100 km s^{-1}. Size distributions after non-thermal sputtering are plotted with blue lines, with a different line pattern for each shock velocity, while the initial size distrubution is plotted as a full blue line. As expected, faster shocks result in more non-thermal sputtering within the clump, and a population of small grains prevails in the 200 km s^{-1} shock case compared to shocks with smaller velocities. The initial size distribution present a peak at radius $\sim$ 25 Å, while after non-thermal sputtering in the clump the peak radius decreases to $\sim$ 10 Å for a 100 km s^{-1} shock, $\sim$ 5 Å for a 140 km s^{-1} shock, and only $\sim$ 2 Å for a 200 km s^{-1} shock. The size distributions resulting from non-thermal sputtering in the clump are then used as input to the thermal sputtering in the interclump medium, which is independent on grain sizes in our formalism for thermal sputtering. Small grains are easily sputtered, while large grains are more resistant and withstand higher temperature with respect to small grains. In the case of forsterite grains in an interclump gas at 10^6 K, thermal sputtering efficiently erodes the grains, leaving just a small fraction of very small grains for the fastest 200 km s^{-1} shock. More grains are able to survive for slower shocks, because the size distributions resulting from non-thermal sputtering are skewed towards larger grains.

The plot on the right hand side of Figure 5.7 shows the same size distributions for non-

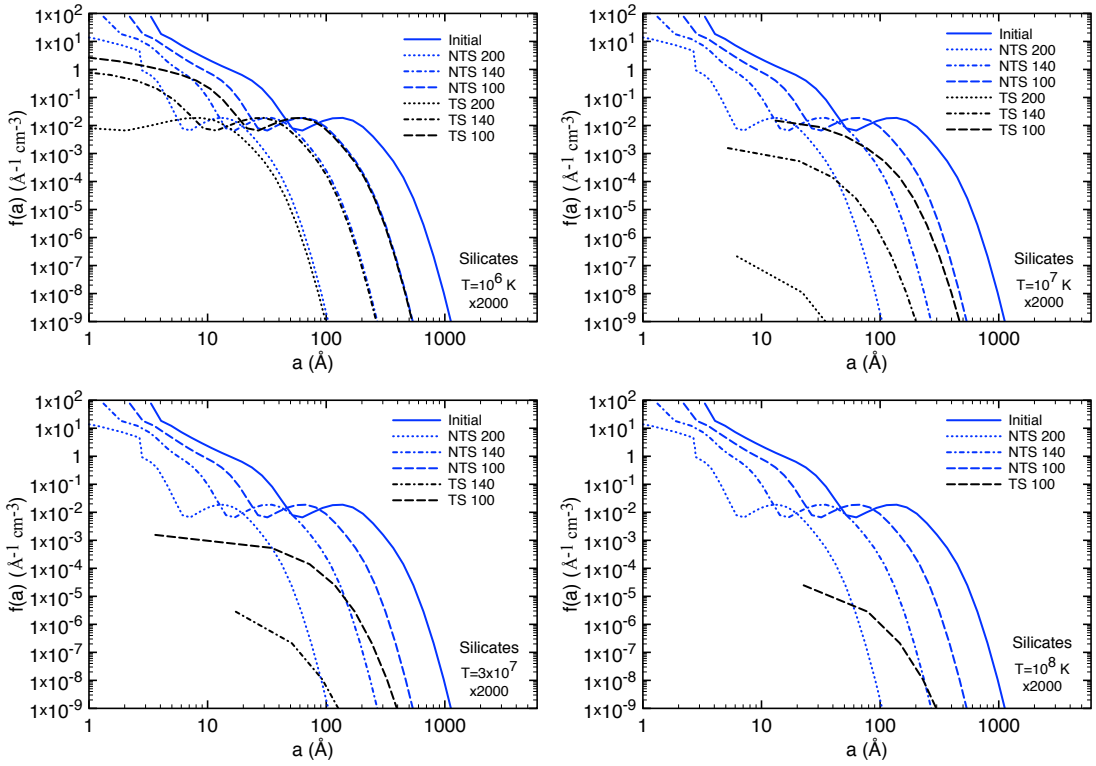

Figure 5.8: Forsterite dust grains size distribution for an interclump temperature of 10^6 K (top-left), 10^7 K (top-right), 3×10^7 K (bottom-left) and 10^8 K (bottom right); and shock velocities of 200 km s^{-1} (dotted lines), 140 km s^{-1} (dotted-dashed lines), 100 km s^{-1} (dashed lines) for a x2000 clump. The initial size distribution is plotted with a full blue line, non-thermal sputtering with blue lines and thermal sputtering with black lines.

thermal sputtering, but the temperature of the interclump medium is raised to 10^7 K. In these conditions, and for all temperatures greater than 10^7 K, no grains survive after 4000 years of thermal sputtering in the interclump medium, as the thermal sputtering erosion

rate reaches its maximum temperatures between 10^7 K and 10^8 K (see Fig 5.5).
Figure 5.8 shows the size distribution of forsterite grains for a clump with number density enhancement of 2000 with respect to a homogeneous ejecta, for the four different interclump temperatures and three different shock velocities we consider. Due to the higher gas density, large grains are present in the initial size distribution, which peaks around 150 Å. This difference permits a better survival of the grains at all temperatures and for all shocks velocities with respect to the previous case. For the lowest temperature of 10^6 K (plot on the top-left), thermal sputtering does not erode grains larger than $\sim$ 200 Å, while still destroying efficiently smaller grains. As the thermal erosion rates increases with higher temperature, grain survival decreases. For interclump temperatures above 10^7 K, grains already sputtered by the fast 200 km s^{-1} shock do not survive, and are completely destroyed. Some grains survive in case of slower shocks, but their abundances are negligible, even for the slowest shock of 100 km s^{-1}. This study shows that forsterite grains are efficiently eroded by both non-thermal and thermal sputtering, owing to their high sputtering yields and the composition of the ejecta zone where they form. The abundant and heavy O^+ and Mg^+ ions sputter and destroy efficiently the grains for all shocks velocities for the clump number densities considered for Cas A and for for temperatures of the interclump medium in the range 10^7 K - 3 $\times 10^7$ K, which characterise the Cas A remnant (Hwang & Laming, 2012).

Alumina

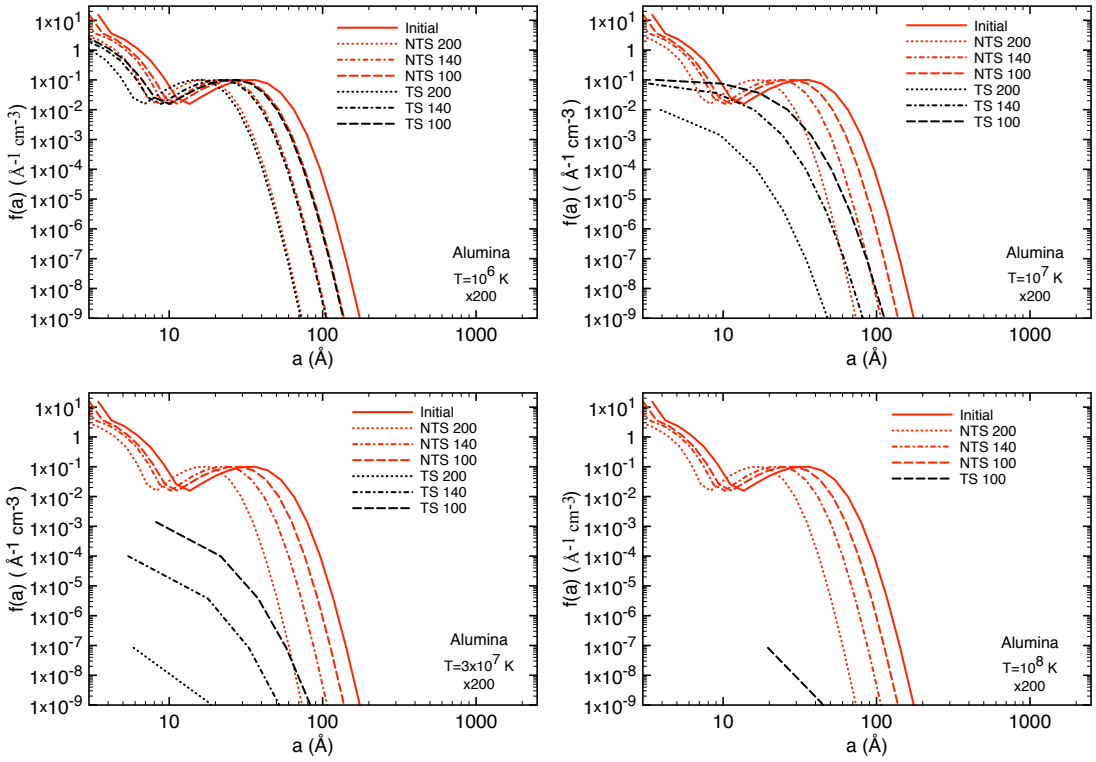

Figure 5.9: Alumina dust grains size distribution for an interclump temperature of 10^6 K (top-left), 10^7 K (top-right), 3 $\times$ 10^7 K (bottom-left) and 10^8 K (bottom right); and shock velocities of 200 km s^{-1} (dotted lines), 140 km s^{-1} (dotted-dashed lines), 100 km s^{-1} (dashed lines) for a x200 clump. The initial size distribution is plotted with a full red line, non-thermal sputtering with red lines and thermal sputtering with black lines.

Figure 5.9 shows the alumina grain size distributions for similar shock parameters and interclump temperatures as in Figure 5.7.
Alumina grains are larger than forsterite grains at the same density, reaching a peak at $\sim$ 40 Å in radius. This, combined with its lower sputtering yield, makes alumina grains more resistant to sputtering with respect to forsterite grains. The effect of the non-thermal sputtering are less pronounced than for forsterite grains, with a change in the peak radius from $\sim$ 30 Å for the slowest shock at 100 km s^{-1} to $\sim$ 20 Å for the fastest 200 km s^{-1} shock. For comparison, forsterite grains are eroded by non-thermal sputtering until their peak radius is less than 2 Å by the 200 km s^{-1} shock.
The larger grains survive thermal sputtering with almost no change in radius for the lowest interclump temperature of 10^6 K (Fig 5.9, plot on the top-left), and the sputtering affects the grains with a radius smaller than 10 Å for the 200 km s^{-1} case. When the interclump temperature increases to 10^7 K, most alumina grains are efficiently sputtered and completely destroyed, leaving only small abundances of small grains. Alumina grains size distribution for interclump temperatures $\geq 10^7$ K do not have a peak; the size distribution is flat and skewed towards small grains due to the bigger impact of thermal sputtering. For an interclump temperature of 3×10^7 K this effect is more pronounced, with all grains smaller than $\sim$ 5 Å completely destroyed, and small quantities of larger grains left. For the maximum temperature of 10^8 K, almost no alumina grains survive, at all shock velocities.

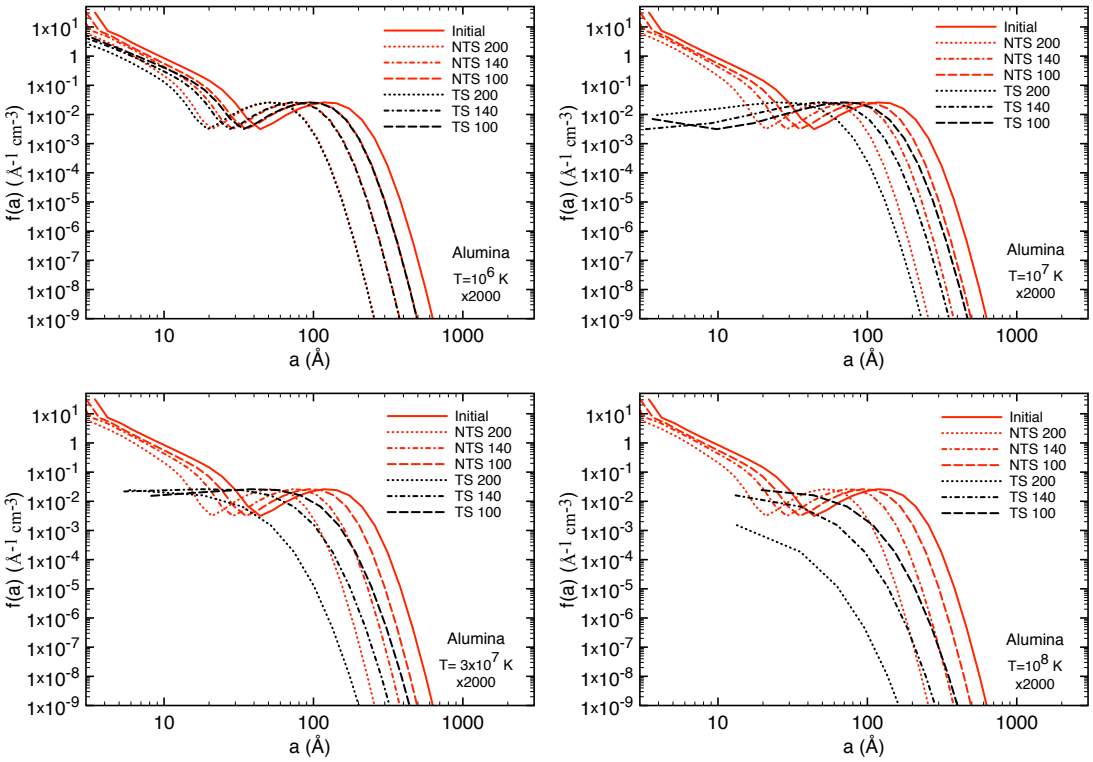

Figure 5.10: Same as Figure 5.9, but for a x2000 clump.

Alumina grains are more resilient than forsterite ones, but are anyway sputtered heavily, especially at high interclump temperatures, for x200 clumps. Some grains survive for temperatures $\leq 3 \times 10^7$ K, consistent with the temperatures observed in Cas A.

The size distribution for a clump with an ejecta gas number density enhancement of

2000 is shown in Figure 5.10. The higher density permits the formation of larger grains, with a peak radius of $\sim$ 150 Å. Non-thermal sputtering in the clump leaves the grains smaller, with a flat size distribution for all interclump temperatures except for the lowest one at 10^6 K. The presence of larger radii with respect to the x200 case helps the grain to survive thermal sputtering: at 10^6 K the size distributions before and after thermal sputtering are substantially unchanged, apart from the population of very small grains with radius $\leq$ 10 Å. At higher interclump temperatures, thermal sputtering is important, and grains are efficiently eroded even if they are not completely destroyed. Some large grains survive, with maximum final radii over 100 Å even at the highest interclump temperatures.

Oxygen rich clumps whose chemical compositions correspond to SN ejecta with gas density increased by factors of 200 and 2000 are both able to efficiently form dust. How much of these grains survive the passage of the reverse shock and the subsequent clump disruption depends on the size of the grains, the shock velocity in the clump and the temperature of the interclump medium. For slow shocks and interclump temperatures less than 10^7 K, both forsterite and alumina grains survive, even if forsterite grains are smaller than alumina ones. However, for higher interclump temperatures, both forsterite and alumina grains suffer heavy thermal sputtering. Low abundances of forsterite and alumina grains survive in the temperature range 10^7 K - 3×10^7 K, if the shock speed is $\leq$ 140 km s^{-1}. For the highest temperature of 10^8 K and the fastest shock of 200 km s^{-1} almost no dust grains formed in the SN ejecta survive.

5.2.2 Results of sputtering for a carbon rich clump

Carbon-rich clumps are not observed in Cas A. Observed clumps are divided in "fast-moving knots" (FMKs, with velocity $\sim$ 5000 km s^{-1}) and "quasi-stationary flocculi" (QFS, with velocity $\sim$ 0-400 km s^{-1}). Observed FMKs present strong lines of sulphur, oxygen and argon, while QFS show lines of nitrogen, helium and oxygen (Hurford & Fesen, 1996). Carbon chains forms in our ejecta model for the highest densities (see Figure 2.8) and carbon and silicon carbide dust condense for x200 and x2000 knots in non-negligible abundance (see Figures 2.11 and 2.12). Since these dust grains condense in a helium-rich, oxygen-poor zone, it is of interest to compare sputtering in different zones by different ions.
We decide to investigate sputtering in a knot with the composition of zone 4 of the ejecta (Table 2.1) and consider carbon and silicon carbide dust grains with sputtering by He^+. As for the oxygen-rich clump, we first consider non-thermal sputtering in an overdense knot, x200 or x2000, and thermal sputtering in the interclump medium after the clump disruption (Table 5.2). The carbon-rich zone has a smaller mass than the oxygen-rich zone, and forms smaller grains on average, silicon carbide grains in particular having the smaller peak radii. Nonetheless, the dust in this region still survives sputtering. Helium ions are less massive than oxygen ions, leading to less sputtering, and carbon and silicon carbide grains have a lower sputtering yield with respect to alumina and forsterite grains (see Fig. 5.1).

Silicon Carbide

Figure 5.11 shows the size distribution of silicon carbide grains for a x200 clump for the shock velocities and interclump temperatures shown in Table 5.2. In the x200 case, silicon

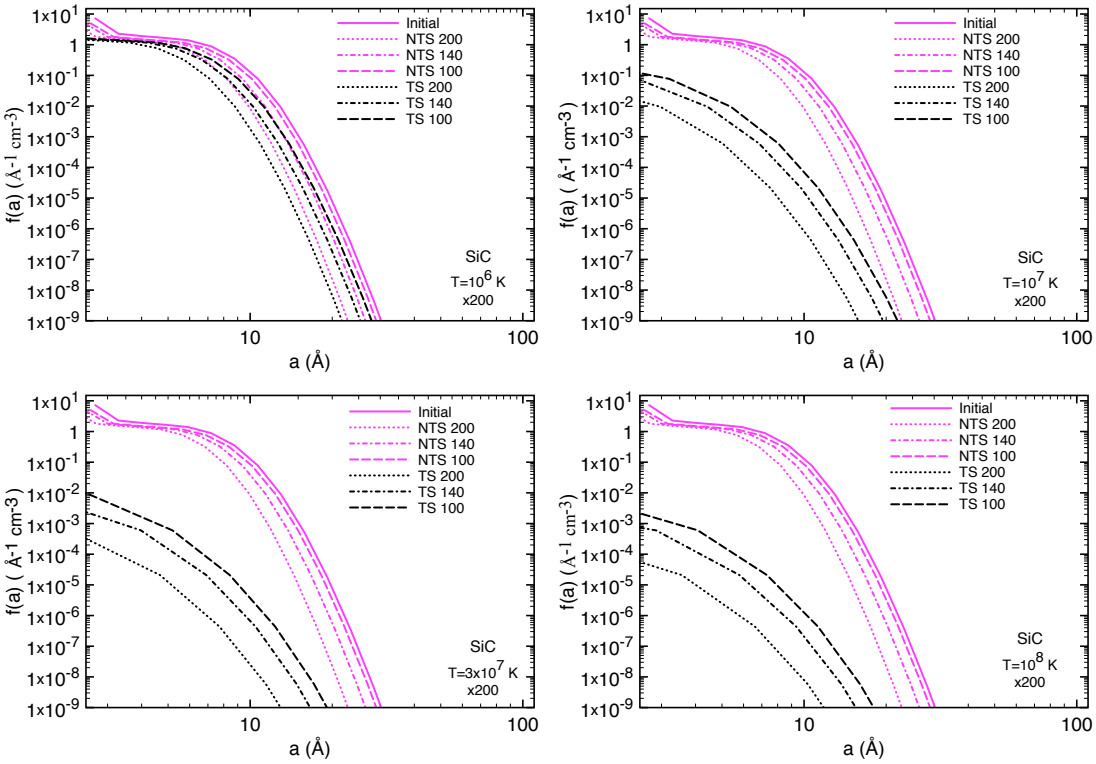

Figure 5.11: Silicon carbide dust grains size distribution for an interclump temperature of 10^6 K (top-left), 10^7 K (top-right), 3×10^7 K (bottom-left) and 10^8 K (bottom right); and shock velocities of 200 km s^{-1} (dotted lines), 140 km s^{-1} (dotted-dashed lines), 100 km s^{-1} (dashed lines) for a x200 clump. The initial size distribution is plotted with a full magenta line, non-thermal sputtering with magenta lines and thermal sputtering with black lines.

carbide grains are the smallest grains of all the dust grains considered, with a peak radius at $\sim$ 10 Å. Silicon carbide grains are characterized by a low erosion rate for non-thermal sputtering (see Figure 5.4), while their erosion rate for thermal sputtering is similar to the that for alumina (see Figure 5.5). As such, non-thermal sputtering in the clump is inefficient and the SiC grain size distribution is unaltered, even for the high shock velocity of 200 km s^{-1}. In contrast, thermal sputtering is quite efficient at eroding the grains, and at temperatures $\geq 10^7$ K heavy thermal sputtering decreases both grains abundance and radius. There is no well defined peak in the final grain size distributions, but most of the grains are smaller than 10 Å.

The case of a clump with number density enhancement of 2000 with respect to a homogeneous ejecta is shown in Figure 5.12. Grains are larger with respect to the x200 case, but still only $\sim$ 15 Å as peak size, making them the smallest grains at this density. Silicon carbide grains are still very resistant to non-thermal sputtering, and instead eroded efficiently by thermal sputtering for a interclump temperature $> 10^7$ K. Final grain radii are small, but they survive at every shock velocity and interclump temperature considered.

Silicon carbide grains are the smaller grains of all the dust types considered, for both

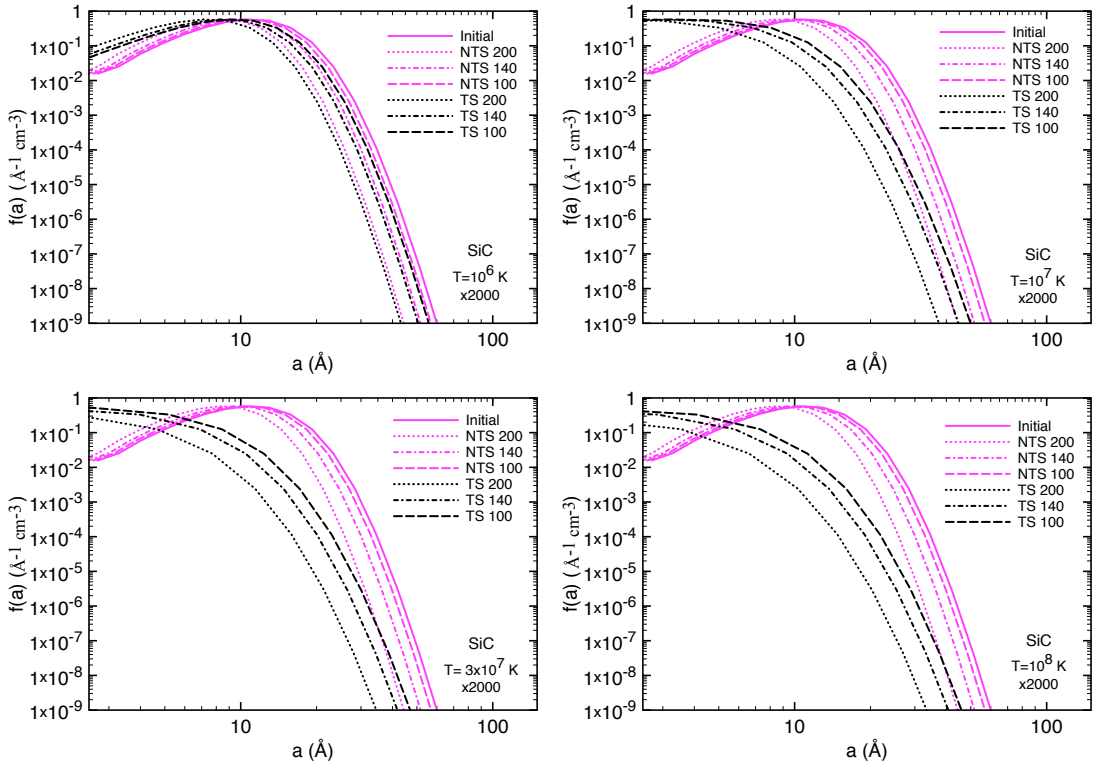

Figure 5.12: Same as Figure 5.11, but for a x2000 clump.

x200 and x2000 clumps. Even if small in radius, silicon carbide grains have a low non-thermal sputtering erosion rate, with non-thermal sputtering impacting just marginally their size for all shock velocities. Thermal sputtering on the other hand is quite efficient, with a thermal erosion rate similar to that of alumina grains. Small grains are efficiently destroyed by thermal sputtering at interclump temperatures $\geq 10^7$K (see top-right and bottom plots in Figures 5.11 and 5.12). This effect is more pronounced for the x200 clump, with just low abundances of grains surviving at high temperature. A better surivival is possible for the relatively larger grains present in the x2000 clump.

Carbon

The last dust grains we consider is carbon, whose size distribution is plotted in Figure 5.13 for a clump with an overdensity factor of 200 with respect to a homogeneous ejecta. Due to the relatively low amount of carbon formed in the ejecta at a density enhanced by a factor 200, carbon dust grows slowly and the peak radius of the grains is small, at $\sim$ 10 Å. Even with this low size, carbon grains are the most resilient dust grains, with the lowest erosion rates for both non-thermal and thermal sputtering (see Figures 5.4 and 5.5). For an interclump temperature of 10^6 K, the size distribution is almost unaffected (see top-left panel in Figure 5.13), while at interclump temperatures larger than 10^7 K some thermal sputtering some thermal sputtering operates for grains with radii less than 20 Å in radius.
The size distribution shape does not change with interclump temperature, and most of the grains survive both non-thermal and thermal sputtering at all interclump temperatures and all shock velocities. Figure 5.14 shows the size distribution of carbon grains for a clump with an overdensity factor of 2000 with respect to a homogeneous ejecta. Larger

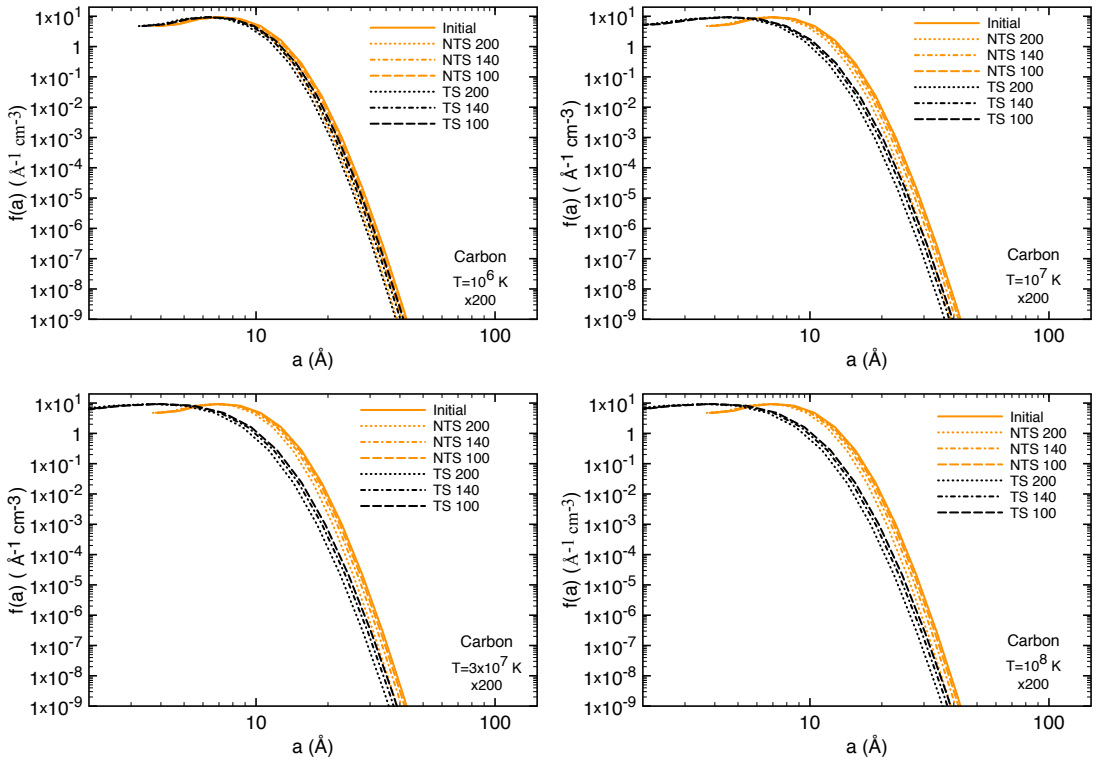

Figure 5.13: Carbon dust grains size distribution for an interclump temperature of 10^6 K (top-left), 10^7 K (top-right), 3×10^7 K (bottom-left) and 10^8 K (bottom right); and shock velocities of 200 km s^{-1} (dotted lines), 140 km s^{-1} (dotted-dashed lines), 100 km s^{-1} (dashed lines) for a x200 clump. The initial size distribution is plotted with a full orange line, non-thermal sputtering with orange lines and thermal sputtering with black lines.

grains are formed with respect to the x200 case, with a prominent peak distribution at radius ~ 70 Å. Consequently, the grains with radius ≥ 50 Å are almost unaffected by both non-thermal sputtering in the clump and thermal sputtering in the interclump medium, and their final radii are weakly dependent on the shock velocity or the temperature of the interclump gas. Some thermal sputtering is present for interclump temperatures $\geq 10^7$ K for the grains with radius smaller than 30 Å.

Carbon grains are the most resilient dust grains we consider in this study, with grains that survive both non-thermal sputtering in the clump and thermal sputtering in the interclump gas. Their initial grain sizes are not large compared with grains of other chemical type, e.g., alumina and forsterite, but their material characteristics result in low erosion rates for both non-thermal and thermal sputtering, and in an higher survival rate.

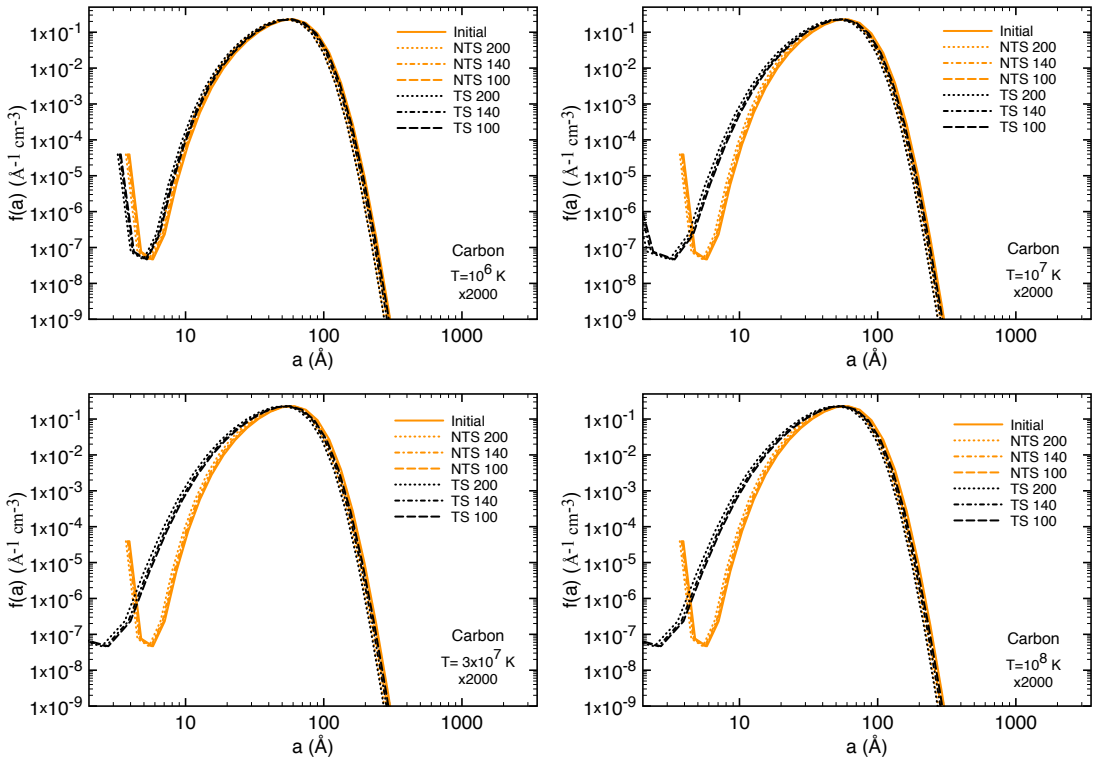

Figure 5.14: Same as Figure 5.13, but for a x2000 clump.

Dust grains formed in the carbon-rich clump survive better to both non-thermal and thermal sputtering with respect to dust grains formed in the oxygen rich zones. The lower mass of the carbon rich zone yields smaller grains on average, but their material characteristics as well as sputtering by the light ion He^+ lower their yields and erosion rates. In contrast to what we derive for an oxygen-rich clump, dust grains are able to survive for every shock velocity and interclump temperature we consider in a shocked, carbon-rich clump.

5.2.3 Limitations of the classical sputtering scheme

The classical sputtering scheme used in the present study has been shown to be a valid approximation for large dust grains, while its application to smaller particles may be disputed.
Jurac et al. (1998) and Serra Díaz-Cano & Jones (2008) use a Monte Carlo code (TRIM) for the transport of ions in matter that follows the trajectory of the colliding ion penetrating in a solid, and traces the collisions. By using this method, the sputtering yield is significantly enhanced with respect to classical sputtering when the grain radius approaches the mean penetration depth of the ion at normal incidence. The reason for this increased yield is that sputtering occurs from the entire particle surface and not just at the implantation site, as described by classical sputtering. Therefore, thermal sputtering for small particle radius ($\lesssim$ 10 Å) could be underestimated in the classical formulation. This approach is computational expensive and time consuming, and has not been carried out for any material except for carbon. Is thus difficult to compare results with the classical approach. Moreover, the TRIM code requires as input also the displacement

energy and the lattice binding energy of the target. Uncertainties in these parameters significantly affect the calculation of sputtering yields, which can differ from experimental values (Bianchi & Ferrara, 2005; May et al., 2000).

The effect of thermal sputtering on polycyclic hydrocarbon molecules/hydrocarbon nano-particles at the molecular level was studied by Bocchio et al. (2012); Micelotta et al. (2010a,b). Their sputtering treatment focuses on nuclear stopping and electronic stopping. Nuclear stopping refers to binary collision between an incoming ion and a single atom in the molecule. Electronic stopping refers to the energy transfer from the incoming ion to the whole molecule, resulting in either photon emission or fragmentation via the loss of an H atom or a C_2H_n molecule. These effects are neglected in the classical sputtering approach, where incoming atoms are always assumed to implant in the target grain, but they become more important as the grain size decreases. This molecular treatment is thus more appropriate for dust particles with dimension comparable to molecules, i.e. with radii below some 10 Å. In this study we use only the classical approach for all dust grains radii, with a possible loss of precision for the smallest particles. However, it is at the moment not possible to quantify this imprecision, as detailed calculations have been performed only for hydrocarbonaceous particles. Further complications arise in the molecular treatment because of the strong dependence of sputtering yields on the values chosen for the nuclear threshold energy and the electronic dissociation energy. The nuclear threshold energy is the energy required for an impacting ion to cause ejection of C atoms, while the electronic dissociation energy is the binding energy of C_2 fragments ejected from the molecule. These quantities are not well constrained and are thus source of significant uncertainties.

We choose to use the classical approach for the case of supernova dust sputtering because of its easy application to different dust types. We are interested mainly in grains larger than 10 Å, where most of the dust mass resides, in order to assess how much dust is produced in SNe and survives the SNR phase. We therefore believe that the use of the classical approach in the present study is well justified, despite the limitations explained above.

5.3 Discussion

In order to better assess dust yields and percentage of survival to non-thermal and thermal sputtering, we calculate the total masses before sputtering, after non-thermal sputtering in the clump, and after 4000 years of thermal sputtering in the interclump medium. Masses of dust species i, as a function of the grain radius r are calculated according to the formula

$$m_i(r) = N_i(r) \times \rho_i \times \frac{4}{3}\pi r^3, \tag{5.14}$$

where $m_i(r)$ is the mass, $N_i(r)$ the total number of grains of radius r for dust grains of chemical type i, and ρ_i is the bulk density of grains of type i. Spherical symmetry is assumed for all grains. To assess the percentage of dust grains that survive each stage of sputtering for each dust type, we sum up the masses for all the grain radii that are larger than the radius of the dust cluster used as seed for that grain (see Table 2.7).
Grains with smaller radii are considered to be back to the gas phase as molecules and do not contribute to the final dust mass budget.

Forsterite								
T(K)	x200				x2000			
	Initial	Non-thermal	Thermal	% surv.	Initial	Non-thermal	Thermal	%surv.
1×10^6	3.1×10^{-3}	4.5×10^{-7}	4.5×10^{-14}	∼0	1.1×10^{-2}	1.2×10^{-5}	9.8×10^{-6}	0.1
1×10^7			-	0			1.7×10^{-12}	∼0
3×10^7			-	0			1.7×10^{-17}	∼0
1×10^8			-	0			2.7×10^{-22}	∼0
Alumina								
T(K)	x200				x2000			
	Initial	Non-thermal	Thermal	% surv.	Initial	Non-thermal	Thermal	%surv.
1×10^6	1.7×10^{-2}	2.0×10^{-3}	1.4×10^{-3}	8.5	1.4×10^{-2}	1.1×10^{-3}	1.0×10^{-3}	7.3
1×10^7			1.5×10^{-6}	∼0			2.8×10^{-4}	1.8
3×10^7			1.6×10^{-11}	∼0			2.8×10^{-5}	0.2
1×10^8			1.2×10^{-18}	∼0			6.6×10^{-7}	∼0
Carbon								
T(K)	x200				x2000			
	Initial	Non-thermal	Thermal	% surv.	Initial	Non-thermal	Thermal	%surv.
1×10^6	7.0×10^{-3}	5.5×10^{-3}	4.6×10^{-3}	66.1	7.1×10^{-3}	5.4×10^{-3}	5.2×10^{-3}	73.6
1×10^7			2.1×10^{-3}	30.1			4.8×10^{-3}	67.5
3×10^7			1.5×10^{-3}	21.8			4.7×10^{-3}	65.5
1×10^8			1.5×10^{-3}	21.2			4.6×10^{-3}	65.4
Silicon Carbide								
T(K)	x200				x2000			
	Initial	Non-thermal	Thermal	% surv.	Initial	Non-thermal	Thermal	%surv.
1×10^6	3.1×10^{-4}	1.4×10^{-4}	6.2×10^{-5}	19.8	9.1×10^{-5}	4.6×10^{-5}	2.9×10^{-5}	31.8
1×10^7			8.2×10^{-8}	∼0			2.8×10^{-6}	3.0
3×10^7			5.7×10^{-10}	∼0			5.3×10^{-7}	0.6
1×10^8			2.6×10^{-10}	∼0			3.0×10^{-7}	0.3

Table 5.3: Total masses of dust grains as a function of dust type, in $M_\odot$. The masses corresponding to the initial grain size distribution,the masses corresponding to the size distributions altered by non-thermal sputtering in the clump and thermal sputtering in the interclump medium are given for a 200 km s^{-1} shock, for x200 and x2000 clumps. The column "% surv." indicates the percentage of dust mass that survives the whole sputtering process.

Tables 5.3, 5.4 and 5.5 show the initial and final masses for shock velocities of 200 km s^{-1}, 140 km s^{-1} and 100 km s^{-1}, respectively, for clumps with overdensity factors of 200 and 2000 with respect to an homogeneous ejecta. These results show once again the importance of gas temperature in the interclump medium and initial dust size distribution for dust survival to sputtering. If the interclump gas temperature is low (10^6 K), at least

Forsterite								
T(K)	x200				x2000			
	Initial	Non-thermal	Thermal	% surv.	Initial	Non-thermal	Thermal	%surv.
1×10^6	3.1×10^{-3}	4.7×10^{-5}	1.2×10^{-7}	∼0	1.1×10^{-2}	2.0×10^{-4}	1.1×10^{-4}	1.0
1×10^7			4.2×10^{-30}	∼0			1.8×10^{-7}	∼0
3×10^7			-	0			3.5×10^{-10}	∼0
1×10^8			-	0			3.6×10^{-13}	∼0
Alumina								
T(K)	x200				x2000			
	Initial	Non-thermal	Thermal	% surv.	Initial	Non-thermal	Thermal	%surv.
1×10^6	1.7×10^{-2}	4.9×10^{-3}	4.0×10^{-3}	23.5	1.4×10^{-2}	3.3×10^{-3}	3.1×10^{-3}	22.4
1×10^7			6.0×10^{-5}	0.4			1.3×10^{-3}	9.1
3×10^7			2.6×10^{-8}	∼0			3.0×10^{-4}	2.2
1×10^8			2.1×10^{-12}	∼0			3.9×10^{-5}	0.3
Carbon								
T(K)	x200				x2000			
	Initial	Non-thermal	Thermal	% surv.	Initial	Non-thermal	Thermal	%surv.
1×10^6	7.0×10^{-3}	6.1×10^{-3}	5.1×10^{-3}	74.1	7.1×10^{-3}	6.1×10^{-3}	6.0×10^{-3}	84.3
1×10^7			2.3×10^{-3}	33.5			5.5×10^{-3}	77.6
3×10^7			1.6×10^{-3}	22.9			5.4×10^{-3}	75.3
1×10^8			1.5×10^{-3}	22.5			5.3×10^{-3}	75.0
Silicon Carbide								
T(K)	x200				x2000			
	Initial	Non-thermal	Thermal	% surv.	Initial	Non-thermal	Thermal	%surv.
1×10^6	3.1×10^{-4}	2.0×10^{-4}	9.7×10^{-5}	31.2	9.1×10^{-5}	6.1×10^{-5}	4.6×10^{-5}	50.3
1×10^7			2.5×10^{-7}	0.1			6.4×10^{-6}	7.0
3×10^7			1.1×10^{-8}	∼0			1.9×10^{-6}	2.0
1×10^8			4.5×10^{-9}	∼0			1.1×10^{-6}	1.2

Table 5.4: Same as Table 5.3, but for a 140 km s^{-1} shock

Forsterite								
T(K)	x200				x2000			
	Initial	Non-thermal	Thermal	% surv.	Initial	Non-thermal	Thermal	%surv.
1×10^6	3.1×10^{-3}	3.3×10^{-4}	3.1×10^{-5}	1.0	1.1×10^{-2}	1.3×10^{-3}	1.0×10^{-3}	8.9
1×10^7			2.1×10^{-21}	∼0			4.8×10^{-5}	0.4
3×10^7			-	0			1.0×10^{-6}	∼0
1×10^8			-	0			1.6×10^{-8}	∼0
Alumina								
T(K)	x200				x2000			
	Initial	Non-thermal	Thermal	% surv.	Initial	Non-thermal	Thermal	%surv.
1×10^6	1.7×10^{-2}	8.8×10^{-3}	7.4×10^{-3}	43.7	1.4×10^{-2}	7.0×10^{-3}	6.7×10^{-3}	47.6
1×10^7			3.5×10^{-4}	2.0			3.4×10^{-3}	24.1
3×10^7			1.3×10^{-6}	∼0			1.3×10^{-3}	9.4
1×10^8			4.8×10^{-10}	∼0			3.0×10^{-4}	2.1
Carbon								
T(K)	x200				x2000			
	Initial	Non-thermal	Thermal	% surv.	Initial	Non-thermal	Thermal	%surv.
1×10^6	7.0×10^{-3}	6.6×10^{-3}	5.6×10^{-3}	79.3	7.1×10^{-3}	6.7×10^{-3}	6.6×10^{-3}	92.1
1×10^7			2.6×10^{-3}	36.6			6.1×10^{-3}	85.0
3×10^7			2.0×10^{-3}	28.1			5.9×10^{-3}	82.6
1×10^8			1.9×10^{-3}	27.5			5.9×10^{-3}	82.5
Silicon Carbide								
T(K)	x200				x2000			
	Initial	Non-thermal	Thermal	% surv.	Initial	Non-thermal	Thermal	%surv.
1×10^6	3.1×10^{-4}	2.5×10^{-4}	1.3×10^{-4}	42.6	9.1×10^{-5}	7.9×10^{-5}	6.0×10^{-5}	65.9
1×10^7			1.0×10^{-6}	0.3			1.0×10^{-5}	11.5
3×10^7			2.4×10^{-8}	∼0			3.4×10^{-6}	3.7
1×10^8			1.2×10^{-8}	∼0			2.2×10^{-6}	2.4

Table 5.5: Same as Table 5.3, but for a 100 km s^{-1} shock

some dust survives for each dust type both for a x200 and a x2000 clump, while for the highest interclump temperature (10^8 K) all dust grains apart from carbon are destroyed

almost completely. Increasing the number density of the clump does not bring a dramatic difference in the in the final mass of surviving dust, but yields larger surviving grains on average, by making them more resilient to thermal sputtering. The survival percentage increases at every interclump temperature as a result. A slower shock reduces significantly the non-thermal sputtering in the clump, leading to higher survival percentages for all dust grains.
Forsterite grains do not survive for interclump temperatures higher than 10^6 K (for the x200 clump) or 10^7 K (for the x2000 clump). It seems that size distribution with larger grains are required to avoid efficient sputtering. Silicon carbide grains, being the dust grains with the smaller radius on average, are also efficiently sputtered even at lower shock velocities. Carbon grains are the only dust type that survive with little sputtering up to the highest interclump temperature of 10^8 K.
Overall, Cas A may need knots with several different overdensity factors with respect to an homogeneous ejecta, and that some of them are possibly much denser, up to a factor of 10 000 or more. The exact velocity of the reverse shock also plays an important role: while the results are plotted here for 200, 140 and 100 km s^{-1}, a much dense knot will have a correspondent lower shock velocity. Figure 5.4 shows that non-thermal sputtering becomes negligible for a relative velocity between dust and gas lower than $\sim$ 30 km s^{-1}, i.e. for a reverse shock velocity $\lesssim$ 50 km s^{-1}. To have a shock velocity in the clump $\leq$ 50 km s^{-1}, the clump filling factor (i.e. the fraction of volume of the ejecta occupied by gas) must be less than 5×10^{-4}. If we perform the same calculations as in Section 3, we obtain clumps with an overdensity of $\sim 2 \times 10^4$ with respect to a homogeneus ejecta. This translates to a clump/interclump ratio $\chi \sim 2000$ if the interclump medium has number density 1 cm^{-3}. Such a small filling factor is not compatible with radiative studies of SNe ejecta (Gallagher et al., 2012).

Barlow et al. (2010) find 0.08 $M_\odot$ of cool (35 K) silicates dust in the centre of Cas A. This is over an order of magnitude higher than the initial forsterite mass in Table 5.3, but we did not consider other sources of silicate dust, such as iron-bearing silicates.
Rho et al. (2008) find dust with various compositions and temperatures and a mass between 0.02 and 0.05 $M_\odot$. This mass is obtained via a fit of several spectra (21 μm peak, weak 21 μm peak, featureless) with several possible dust compositions, including alumina, forsterite, enstatite, glass, magnesium protosilicate, iron oxyde.
The masses found by Rho et al. (2008) for alumina and magnesium silicates are $\sim 8.2 \times 10^{-4}$ $M_\odot$ and $\sim 8\times 10^{-5}$ $M_\odot$, respectively. The mass of carbon dust is $\sim 2\times 10^{-3}$ $M_\odot$. These results are for warm dust, i.e. dust that it's already been heated and reprocessed by the reverse shock. If we compare these values to the ones in Tables 5.3, 5.4 and 5.5 for forsterite, alumina and carbon grains, we see that the observed mass is lower than our calculated mass after non-thermal sputtering in the clump, but higher than after thermal sputtering in the interclump medium. This points to a scenario in which Cas A dust grains are being heated and reprocessed by the reverse shock both by non-thermal sputtering in clumps and by thermal sputtering in the interclump medium.

5.3.1 High density clumps

Studies on the composition of presolar grains, i.e. single grains extracted from carbonaceous meteorites, find micron sized silicate inclusions (Nagashima et al., 2004; Zinner, 2014). This is incompatible with our results, since forsterite is the most fragile dust type and forsterite grains are efficiently sputtered and destroyed, with grains that do not reach

the micron size.
Cassiopeia A, as a SN type IIb, is characterised by lower gas densities in the ejecta compared to SN type IIP or IIn. This lower gas densities are caused by the thin hydrogen envelope that characterizes Type IIb SNe. Without a thick hydrogen envelope, most of the explosion energy is deposited into the helium core, and leads to higher ejecta expansion velocities. The resulting gas density in the core is about three orders of magnitude lower in a SN Type IIb with respect to a Type IIP (Nozawa et al., 2010). To assess the effect of a denser clump and lower reverse shock velocities, we calculate the size distribution for forsterite for clumps with an overdensity factor of 2×10^4 and 2×10^5 with respect to a homogeneous ejecta (hereafter x2e4 and x2e5, respectively).
We also consider the size distribution calculated for a clumpy model of SN1987A by Sarangi & Cherchneff (accepted).

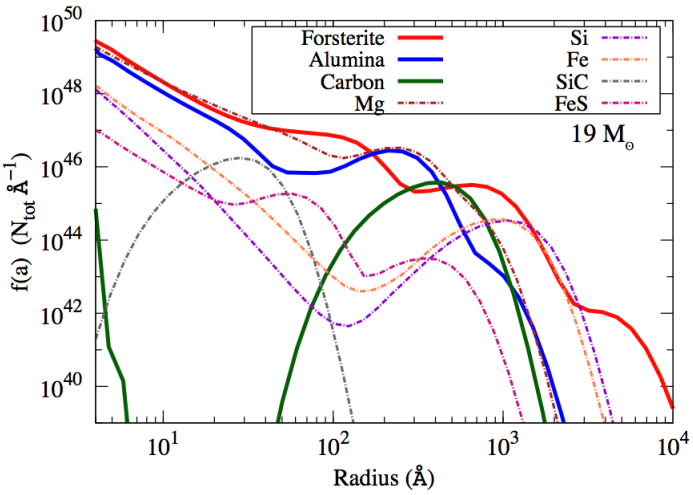

Figure 5.15: Total number of dust grains as a function of radius for a clumpy model of SN1987A. From Sarangi & Cherchneff (accepted).

This model uses realistic filling factors for each zone of the ejecta in order to reproduce the density observed in SN1987A and other massive Type II-P SNe with progenitor stellar mass around 19 $M_\odot$. The derived total numbers of dust grains for various dust types are reproduced in Figure 5.15. The grains formed in this model have radii that reach the micron size, and the higher density both in the interclump medium and in the clumps is able to slow down the shock significantly, making non-thermal sputtering negligible.
In Table 5.6 we reported the final masses of forsterite dust for the x2e4 and x2e5 clumps.

The larger average radius of the grains and the ineffectiveness of non-thermal sputtering at the lower shock velocities for x2e4 and x2e5 clumps permit a high degree of survival across all possible interclump temperatures. In particular, forsterite grains with large radius are preserved almost completely, in agreement with observation.
In Figure 5.16 we show the results for the thermal sputtering calculation for this size distribution of forsterite grains taken Sarangi & Cherchneff (accepted).

After 4000 years of thermal sputtering in the interclump medium, the large grains with radius around one micron remain unchanged in size. Grains smaller than $\sim 2 \times 10^3$ Å suffer some erosion by thermal sputtering, especially at high interclump temperatures. These results are consistent with the observation of large silicate inclusions in presolar

Forsterite						
T(K)	x2e4			x2e5		
	Initial	Thermal	% surv.	Initial	Thermal	%surv.
1×10^6	5.4×10^{-3}	5.3×10^{-3}	98.7	3.9×10^{-2}	3.4×10^{-2}	99.7
1×10^7		4.7×10^{-3}	86.2		3.7×10^{-2}	96.4
3×10^7		4.1×10^{-3}	75.7		3.6×10^{-2}	93.0
1×10^8		3.6×10^{-3}	65.7		3.5×10^{-2}	89.1

Table 5.6: Forsterite masses in $M_\odot$ after 4000 years of thermal sputtering for x2e4 and x2e5 clumps. Non-thermal sputtering is negligible at this gas density in the clump since the reverse shock is decelerated under 50 km s^{-1}.

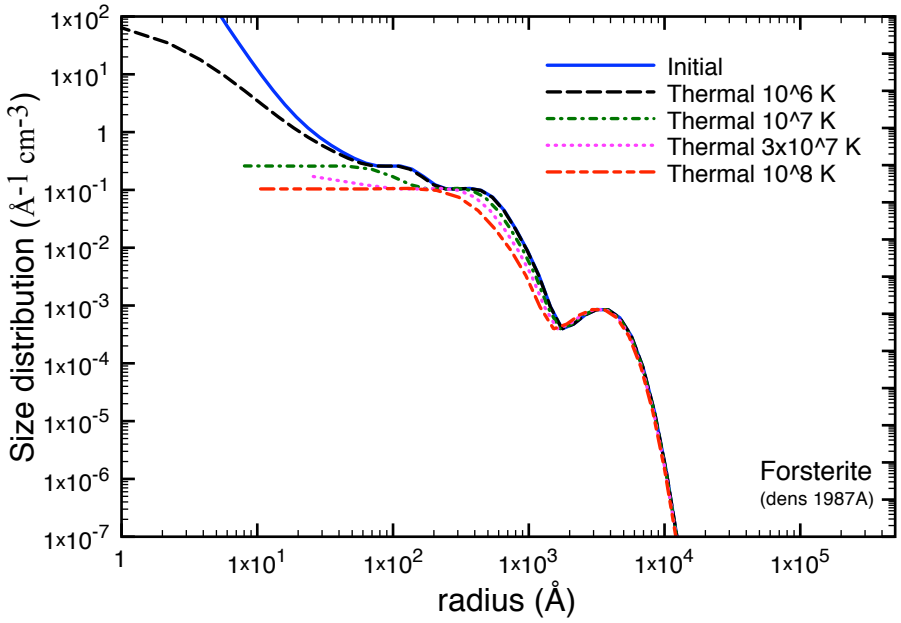

Figure 5.16: Forsterite size distribution, before sputtering (full blue line), and after 4000 years of thermal sputtering for interclump temperatures of 10^6 K (black long-dashed line), 10^7 K (green dot-dashed line), 3×10^7 K (magenta dotted line), and 10^8K (short-long-dashed red line).

grains of supernova origin. Only the large forsterite grains formed in the clumpy ejecta of Type II supernovae can survive the non-thermal sputtering in shocked, dense ejecta clumps, and the harsh thermal sputtering in the interclump medium, once clumps have been disrupted by the passage of the reverse shock in the SN remnant. The mass of warm forsterite observed in Cas A by Rho et al. (2008) is $\sim 8 \times 10^{-5}$, two orders of magnitude lower than the one calculated for x2e4 and x2e5 clumps. Such dense clumps in Cas A are not favoured by observations. This points to the low dust survival rate and small dust grain size in Cas A and Type IIb SNe, and to their inefficiency as dust providers in the universe with respect to other SNe Type, in particular Type IIP and Type IIn.

6. Conclusions

6.1 Ejecta

The main results of this study point to the importance of density in the formation processes of molecules and dust in SNe and their remnants. In the homogeneous ejecta of a Type IIb SN, we find that no molecular cluster precursors to dust could form at the low gas density involved. This points to the complexity of the dust formation processes at a microscopic scale, and the fact that dust nucleation is driven by non-equilibrium chemistry in the gas-phase. Existing studies based on the CNT formalism ignore the dust nucleation bottleneck and indicate fairly large masses of grains formed in Type IIb SNe (e.g., Nozawa et al. (2010)). Our present results are in contrast with these studies and show that the formation of dust is extremely gas density-dependent. This dependency does not pertain to the condensation phase of dust clusters but to their formation phase, i.e., nucleation out of the gas-phase. Increase in gas density by a factor of $200 - 2000$ permits an efficient nucleation of dust grains and indicates the need for non-homogenous, Type IIb SN ejecta in the form of clumps or knots.

The chemical complexity of the dust grains that form in SN ejecta is also density-dependent and grows with increasing gas density. In particular, carbon dust only forms at high gas number densities and traces the densest SN ejecta conditions. In Cas A, the IR spectra measured by Spitzer indicate a variety of spectral signatures ascribed to warm dust which vary according to position and observed atomic lines in the remnant (Arendt et al., 2014; Rho et al., 2008). These grains include silicates, alumina, pure metals, carbides, iron sulphide, and amorphous carbon and have been processed by the RS, but they originate from the SN ejecta that led to Cas A. According to our results, the SN ejecta gas must be in the form of dense clumps, with density contrast of at least 200 compared to the homogeneous Type IIb SN ejecta, to properly account for the dust chemical diversity in Cas A inferred from the IR data. More generally, the chemical type of dust detected in SNe and SNRs can be used as a tracer of the physical conditions of the dust birthplace, a denser gas leading to dust grains of greater chemical variety.

6.2 Reverse shock

Recent observations with Herschel of high excitation energy rotational lines of CO in one region of Cas A where CO was already detected at the RS position with Spitzer have brought evidence of hot and dense gas in the remnant (Wallström et al., 2013). According to the line analysis, this O/CO-rich region is characterised by warm and dense gas ($n_{gas} \sim 10^6$ cm^{-3}), and probably corresponds to post-RS gas. Such conditions are found in the wake of our 200 and 140 km s^{-1} RS crossing a dense clump where CO reforms on a time scale of ~ 100 days. These observations therefore support the present model results which indicate that molecules, including CO and SiO, reform after the RS passage in sufficient amount to warrant detection. The molecular content of Cas A should then include two components reflecting various evolutionary phases of the remnant. A

cold component would comprise species formed in the SN clumpy ejecta (e.g., SiS, CO, O_2, and SO), that have not yet been processed by the RS and have large abundances. Such a cool component has been confirmed in SN1987A by the detection of low excitation rotational lines of CO with ALMA (Kamenetzky et al., 2013). A warm/hot component would coincide with shocked clumps and newly reformed molecules (e.g., CO, SiO) in the post-reverse shock gas, as seen in Cas A with Herschel. The warm CO component should have a lower abundance than its cold counterpart. The amount of reformed molecules depends on the shock strength, the faster shocks producing larger quantities of chemical species in the post-shock gas. For all shock speeds, dust clusters are unable to reform in sufficient quantities in the post-shock gas to guarantee a viable dust formation pathway from the gas phase in SN remnants.

6.3 Dust sputtering

Our study of dust sputtering in Cas A underlies the importance of dense clumps. Dust clusters form with higher abundances and chemical complexity in a dense clump, which result in more efficient condensation of dust grains with larger radii. Dense clumps protect the grains from the fast reverse shock both by decelerating the incoming shock wave and by keeping the gas temperature low. A lower relative velocity of the grains with respect to the gas inhibits non-thermal sputtering, while lower gas temperatures inhibit thermal sputtering in the clump. When the clump is disrupted by the reverse shock, and grains are sputtered by the hot interclump gas, small grain are efficiently eroded in a short time and completely returned to the gas phase. Temperature in the hot interclump medium is an important factor in thermal sputtering, both because temperature enters as $T^{1/2}$ in the thermal sputtering calculation and because of the thousands of years required for the gas to cool down.
Another important factor in grain survival is their composition: carbon and silicon carbide have lower sputtering yields with respect to alumina and forsterite, and survive longer and with less erosion to both non-thermal and thermal sputtering. Forsterite grains in particular, as the most fragile of the dust types considered, are efficiently destroyed for all the shock velocities considered. The choice of the impacting ion also plays a large role: dust grains in oxygen rich knots are sputtered by heavy oxygen ions, while grains in carbon rich knots are sputtered by lighter helium ions.
Due to the combination of all these factors, of the dust types considered, carbon is the most resilient. Carbon grains survive for all the shock velocities in the clump, the interclump gas temperatures, and the clump densities considered. Alumina and silicon carbide survive in small quantities for temperatures $> 10^6$ K and shock velocities $\leqslant 140$ km s^{-1}. For the highest shock velocity considered in the clump (200 km s^{-1}) and the highest interclump temperature (10^8 K), no grains of alumina or silicon carbide survive. Forsterite grains are the most destroyed between the dust types considered. Only a small amount of forsterite grains survive for the lowest shock velocity of 100 km s^{-1} and for the lowest interclump temperature of 10^6 K. These results point to the inability of Type IIb SN to produce dust that can survive the remnant phase. This is caused by the low density of the ejecta, that leads both to small dust grains condensed in the ejecta and to fast reverse shock in the SNR. Better dust survival is achieved by considering micron size grains, such as the ones produced in Type IIP SN such as SN1987A.

Our results differ significantly from previous studies of Cas A (Nozawa et al., 2010). The effect of a clumpy ejecta points to the importance of modelling inhomogeneities in

SNe and SNRs, and on the fundamental impact of density in molecule and dust formation. Our use of chemical kinetics points to the complicated and active chemistry present in SNe ejecta, and to the role of dust clusters in the nucleation phase of dust. The derived grains size distribution is different from the ones derived by Nozawa et al. (2007, 2010) and used by Silvia et al. (2010, 2012), with grains smaller on average and a different size distribution shape. Clumps are again a main factor in reverse shock models. They slow down the fast reverse shock, keep the gas cool and help reduce dust grains erosion.

The results in this thesis add insight in the contribution of SNe Type IIb to the dust budget of galaxies and the universe. Due mainly to their thin hydrogen envelope and fast reverse shock crossing a rarefied ejecta, this Type of SNe and SNRs are not efficient dust producers. Even with a clumpy model of the ejecta, dust grains form with a small average radius, and do not grow to the micron size. Oxide grains are almost totally destroyed, while a fraction of carbon-rich dust grains survives. Our study of dust sputtering in dense clumps in SNe Type II-P points to them as more efficient dust contributors to the universe. In our model, a SNe Type II-P with a progenitor mass of ~ 20 $M_{\odot}$ produces large grains, up to the micron size, that survive unscathed the passage of the reverse shock. This point to SNe as potentially important contributors to dust enrichment in galaxies.

Bibliography

Alam, M. K. 1987, Aerosol Science and Technology, 6, 41

Andersen, H. H., & Bay, H. L. 1981, Sputtering yield measurements, ed. R. Behrisch, 145

Andrews, J. E., Gallagher, J. S., Clayton, G. C., et al. 2010, ApJ, 715, 541

Andrews, J. E., Sugerman, B. E. K., Clayton, G. C., et al. 2011, ApJ, 731, 47

Angel, G. C., & Samson, J. A. R. 1988, Physical Review A, 38, 5578

Arendt, R. G., Dwek, E., Kober, G., Rho, J., & Hwang, U. 2014, ApJ, 786, 55

Arendt, R. G., Dwek, E., & Moseley, S. H. 1999, ApJ, 521, 234

Bach, H. 1970, Nuclear Instruments and Methods, 84, 4

Barlow, M. J., Krause, O., Swinyard, B. M., et al. 2010, A&A, 518, L138

Begemann, B., Dorschner, J., Henning, T., Mutschke, H., & Thamm, E. 1994, The Astrophysical Journal Letters, 423, L71

Behrisch, R., Bohdansky, J., Oetjen, G. H., et al. 1976, Journal of Nuclear Materials, 60, 321

Bianchi, S., & Ferrara, A. 2005, MNRAS, 358, 379

Bianchi, S., & Schneider, R. 2007, MNRAS, 378, 973

Biscaro, C., & Cherchneff, I. 2014, A&A, 564, A25

Blair, W. P., Ghavamian, P., Long, K. S., et al. 2007, ApJ, 662, 998

Blair, W. P., Morse, J. A., Raymond, J. C., et al. 2000, ApJ, 537, 667

Bocchio, M., Micelotta, E. R., Gautier, A.-L., & Jones, A. P. 2012, A&A, 545, A124

Bohdansky, J. 1980, Journal of Nuclear Materials, 93, 44

—. 1984, Nuclear Instruments and Methods in Physics Research B, 2, 587

Bohdansky, J., Bay, H. L., & Ottenberger, W. 1978, Journal of Nuclear Materials, 76, 163

Borghesi, A., Bussoletti, E., Colangeli, L., Orofino, V., & Guido, M. 1986, Infrared Physics, 26, 37

Borkowski, K. J., & Shull, J. M. 1990, ApJ, 348, 169

Borkowski, K. J., Williams, B. J., Reynolds, S. P., et al. 2006, The Astrophysical Journal Letters, 642, L141

Bouchet, P., De Buizer, J. M., Suntzeff, N. B., et al. 2004, ApJ, 611, 394

Burke, J. R., & Silk, J. 1974, ApJ, 190, 1

Catchpole, R. M., Whitelock, P. A., Feast, M. W., et al. 1988, MNRAS, 231, 75P

Cherchneff, I., & Dwek, E. 2009, ApJ, 703, 642

—. 2010, ApJ, 713, 1

Chevalier, R. A. 2005, in Astronomical Society of the Pacific Conference Series, Vol. 342, 1604-2004: Supernovae as Cosmological Lighthouses, ed. M. Turatto, S. Benetti, L. Zampieri, & W. Shea, 422

Chevalier, R. A. 2006, ArXiv Astrophysics e-prints, astro-ph/0607422

Chevalier, R. A., & Kirshner, R. P. 1979, ApJ, 233, 154

Chihara, H., Koike, C., Tsuchiyama, A., Tachibana, S., & Sakamoto, D. 2002, A&A, 391, 267

Clayton, D. D., Deneault, E. A.-N., & Meyer, B. S. 2001, ApJ, 562, 480

Clayton, D. D., Liu, W., & Dalgarno, A. 1999, Science, 283, 1290

Colangeli, L., Mennella, V., Palumbo, P., Rotundi, A., & Bussoletti, E. 1995, A& AS, 113, 561

Dalgarno, A., Yan, M., & Liu, W. 1999, ApJS, 125, 237

Danziger, I. J., Lucy, L. B., Bouchet, P., & Gouiffes, C. 1991, in Supernovae, ed. S. E. Woosley, 69

DeLaney, T., Rudnick, L., Stage, M. D., et al. 2010, ApJ, 725, 2038

Docenko, D., & Sunyaev, R. A. 2010, A&A, 509, A59

Dorschner, J., Begemann, B., Henning, T., Jaeger, C., & Mutschke, H. 1995, A&A, 300, 503

Douvion, T., Lagage, P. O., & Pantin, E. 2001, A&A, 369, 589

Draine, B. T. 1984, The Astrophysical Journal Letters, 277, L71

Draine, B. T., & Salpeter, E. E. 1979a, ApJ, 231, 438

—. 1979b, ApJ, 231, 77

Dunne, L., Eales, S., Ivison, R., Morgan, H., & Edmunds, M. 2003, Nature, 424, 285

Dunne, L., Maddox, S. J., Ivison, R. J., et al. 2009, MNRAS, 394, 1307

Dwek, E., & Arendt, R. G. 1992, Annual Review of Astronomy and Astrophysics, 30, 11

Dwek, E., Foster, S. M., & Vancura, O. 1996, ApJ, 457, 244

Dwek, E., Galliano, F., & Jones, A. P. 2007, ApJ, 662, 927

Dwek, E., Moseley, S. H., Glaccum, W., et al. 1992, The Astrophysical Journal Letters, 389, L21

Dwek, E., & Scalo, J. M. 1980, ApJ, 239, 193

Elmhamdi, A., Danziger, I. J., Chugai, N., et al. 2003, MNRAS, 338, 939

Ercolano, B., Barlow, M. J., & Sugerman, B. E. K. 2007, MNRAS, 375, 753

Fabian, D., Jäger, C., Henning, T., Dorschner, J., & Mutschke, H. 2000, A&A, 364, 282

Fabian, D., Posch, T., Mutschke, H., Kerschbaum, F., & Dorschner, J. 2001, A&A, 373, 1125

Fassia, A., Meikle, W. P. S., Chugai, N., et al. 2001, MNRAS, 325, 907

Feder, J., Russell, K. C., Lothe, J., & Pound, G. M. 1966, Advances in Physics, 15, 111

Fesen, R. A., Morse, J. A., Chevalier, R. A., et al. 2001, Astronomical Journal, 122, 2644

Fesen, R. A., Hammell, M. C., Morse, J., et al. 2006, ApJ, 645, 283

Gall, C., Hjorth, J., & Andersen, A. C. 2011, A & A Review, 19, 43

Gallagher, J. S., Sugerman, B. E. K., Clayton, G. C., et al. 2012, ApJ, 753, 109

Gear, C. W. 1971, IEEE Transactions on Circuit Theory, 18, 89

Gehrz, R. 1989, in IAU Symposium, Vol. 135, Interstellar Dust, ed. L. J. Allamandola & A. G. G. M. Tielens, 445

Gerardy, C. L., Fesen, R. A., Nomoto, K., et al. 2002, Pub. Astr. Soc. Japan, 54, 905

Gomez, H. L., Dunne, L., Ivison, R. J., et al. 2009, MNRAS, 397, 1621

Gotthelf, E. V., Koralesky, B., Rudnick, L., et al. 2001, The Astrophysical Journal Letters, 552, L39

Goumans, T. P. M., & Bromley, S. T. 2012, MNRAS, 420, 3344

Green, D. A., Tuffs, R. J., & Popescu, C. C. 2004, MNRAS, 355, 1315

Hammer, N. J., Janka, H.-T., & Müller, E. 2010, ApJ, 714, 1371

Hechtl, E., Bohdansky, J., & Roth, J. 1981, Journal of Nuclear Materials, 103, 333

Heger, A., Fryer, C. L., Woosley, S. E., Langer, N., & Hartmann, D. H. 2003, ApJ, 591, 288

Henning, T., Begemann, B., Mutschke, H., & Dorschner, J. 1995, A& AS, 112, 143

Hindmarsh, A. C. 1983, Scientific Computing, R. S. Stepleman et al. (eds.), North-Holland, Amsterdam, 1, 55

Hines, D. C., Krause, O., Rieke, G. H., et al. 2006, The Astrophysical Journal Letters, 641, L85

Hines, D. C., Rieke, G. H., Gordon, K. D., et al. 2004, ApJS, 154, 290

Hofmeister, A. M., Keppel, E., & Speck, A. K. 2003, MNRAS, 345, 16

Hurford, A. P., & Fesen, R. A. 1996, ApJ, 469, 246

Hwang, U., & Laming, J. M. 2012, ApJ, 746, 130

Hwang, U., Laming, J. M., Badenes, C., et al. 2004, The Astrophysical Journal Letters, 615, L117

Indebetouw, R., Matsuura, M., Dwek, E., et al. 2014, The Astrophysical Journal Letters, 782, L2

Inserra, C., Turatto, M., Pastorello, A., et al. 2011, MNRAS, 417, 261

Itoh, H. 1986, Pub. Astr. Soc. Japan, 38, 717

—. 1988, Pub. Astr. Soc. Japan, 40, 673

Jacobson, M. 2005, Fundamentals of Atmospheric Modeling (Cambridge)

Jones, A. P., Tielens, A. G. G. M., & Hollenbach, D. J. 1996, ApJ, 469, 740

Jones, A. P., Tielens, A. G. G. M., Hollenbach, D. J., & McKee, C. F. 1994, ApJ, 433, 797

Jurac, S., Johnson, R. E., & Donn, B. 1998, ApJ, 503, 247

Kamenetzky, J., McCray, R., Indebetouw, R., et al. 2013, The Astrophysical Journal Letters, 773, L34

Kemper, F., Jäger, C., Waters, L. B. F. M., et al. 2002, Nature, 415, 295

Kitaura, F. S., Janka, H.-T., & Hillebrandt, W. 2006, A&A, 450, 345

Klein, R. I., McKee, C. F., & Colella, P. 1994, ApJ, 420, 213

Koide, T., Shidara, T., Fukutani, H., et al. 1990, Phys. Rev. B, 42, 4979

Koike, C., Chihara, H., Tsuchiyama, A., et al. 2003, A&A, 399, 1101

Koike, C., Hasegawa, H., Asada, N., & Hattori, T. 1981, Astrophysics and Space Science, 79, 77

Koike, C., Kaito, C., Yamamoto, T., et al. 1995a, Icarus, 114, 203

Koike, C., Kimura, S., Kaito, C., et al. 1995b, ApJ, 446, 902

Kotak, R. 2008, in IAU Symposium, Vol. 250, IAU Symposium, ed. F. Bresolin, P. A. Crowther, & J. Puls, 437–442

Kotak, R., Meikle, P., van Dyk, S. D., Höflich, P. A., & Mattila, S. 2005, The Astrophysical Journal Letters, 628, L123

Kotak, R., Meikle, P., Pozzo, M., et al. 2006, The Astrophysical Journal Letters, 651, L117

Kotak, R., Meikle, W. P. S., Farrah, D., et al. 2009, ApJ, 704, 306

Kozasa, T., Hasegawa, H., & Nomoto, K. 1991, A&A, 249, 474

Kozma, C., & Fransson, C. 1992, ApJ, 390, 602

Krause, O., Birkmann, S. M., Rieke, G. H., et al. 2004, Nature, 432, 596

Krause, O., Birkmann, S. M., Usuda, T., et al. 2008, Science, 320, 1195

Liu, W., & Dalgarno, A. 1994, ApJ, 428, 769

—. 1995, ApJ, 454, 472

Lu, W. C., Wang, C. Z., Nguyen, V., et al. 2003, J. Phys. Chem., 107, 6936

Lucy, L. B., Danziger, I. J., Gouiffes, C., & Bouchet, P. 1989, in Lecture Notes in Physics, Berlin Springer Verlag, Vol. 350, IAU Colloq. 120: Structure and Dynamics of the Interstellar Medium, ed. G. Tenorio-Tagle, M. Moles, & J. Melnick, 164

Maeder, A. 2009, Physics, Formation and Evolution of Rotating Stars (Maeder, A.)

Maguire, K., Di Carlo, E., Smartt, S. J., et al. 2010, MNRAS, 404, 981

Maíz-Apellániz, J., Bond, H. E., Siegel, M. H., et al. 2004, The Astrophysical Journal Letters, 615, L113

Matheson, T., Filippenko, A. V., Barth, A. J., et al. 2000, Astronomical Journal, 120, 1487

Matsunami, N., Yamamura, Y., Itakawa, W., et al. 1980, Radiation Effects, 57, 15

Matsuura, M., Dwek, E., Meixner, M., et al. 2011, Science, 333, 1258

Mattila, S., Meikle, W. P. S., Lundqvist, P., et al. 2008, MNRAS, 389, 141

May, P. W., Pineau des Forêts, G., Flower, D. R., et al. 2000, MNRAS, 318, 809

Meikle, W. P. S., Mattila, S., Pastorello, A., et al. 2007, ApJ, 665, 608

Meikle, W. P. S., Kotak, R., Farrah, D., et al. 2011, ApJ, 732, 109

Micelotta, E., & Dwek, E. 2013, in Proceedings of The Life Cycle of Dust in the Universe: Observations, Theory, and Laboratory Experiments (LCDU2013). 18-22 November, 2013. Taipei, Taiwan.

Micelotta, E. R., Jones, A. P., & Tielens, A. G. G. M. 2010a, A&A, 510, A37

—. 2010b, A&A, 510, A36

Morse, J. A., Fesen, R. A., Chevalier, R. A., et al. 2004, ApJ, 614, 727

Mutschke, H., Andersen, A. C., Clément, D., Henning, T., & Peiter, G. 1999, A&A, 345, 187

Nagashima, K., Krot, A. N., & Yurimoto, H. 2004, Nature, 428, 921

Nenadović, T., Perraillon, B., Bogdanov, Ž., Djordjević, Z., & Milić, M. 1990, Nuclear Instruments and Methods in Physics Research B, 48, 538

Nomoto, K., Sugimoto, D., Sparks, W. M., et al. 1982, Nature, 299, 803

Nomoto, K., Suzuki, T., Shigeyama, T., et al. 1993, Nature, 364, 507

Nozawa, T., Kozasa, T., & Habe, A. 2006, ApJ, 648, 435

Nozawa, T., Kozasa, T., Habe, A., et al. 2007, ApJ, 666, 955

Nozawa, T., Kozasa, T., Tominaga, N., et al. 2010, ApJ, 713, 356

Nozawa, T., Kozasa, T., Umeda, H., Maeda, K., & Nomoto, K. 2003, ApJ, 598, 785

Ordal, M. A., Bell, R. J., Alexander, Jr., R. W., Newquist, L. A., & Querry, M. R. 1988, Appl. Opt., 27, 1203

Patnaude, D. J., & Fesen, R. A. 2007, Astronomical Journal, 133, 147

Pegourie, B. 1988, A&A, 194, 335

Pei, Y. C., Fall, S. M., & Bechtold, J. 1991, ApJ, 378, 6

Poglitsch, A., Waelkens, C., Geis, N., et al. 2010, A&A, 518, L2

Posch, T., Baier, A., Mutschke, H., & Henning, T. 2007, ApJ, 668, 993

Pozzo, M., Meikle, W. P. S., Fassia, A., et al. 2004, MNRAS, 352, 457

Rauscher, T., Heger, A., Hoffman, R. D., & Woosley, S. E. 2002, ApJ, 576, 323

Reed, J. E., Hester, J. J., Fabian, A. C., & Winkler, P. F. 1995, ApJ, 440, 706

Reynolds, S. P. 1985, in The Crab Nebula and Related Supernova Remnants, ed. M. C. Kafatos & R. B. C. Henry, 159–163

Reynolds, S. P., Borkowski, K. J., Hwang, U., et al. 2007, The Astrophysical Journal Letters, 668, L135

Rho, J., Jarrett, T. H., Reach, W. T., Gomez, H., & Andersen, M. 2009a, The Astrophysical Journal Letters, 693, L39

Rho, J., Onaka, T., Cami, J., & Reach, W. T. 2012, The Astrophysical Journal Letters, 747, L6

Rho, J., Reach, W. T., Tappe, A., et al. 2009b, ApJ, 700, 579

Rho, J., Kozasa, T., Reach, W. T., et al. 2008, ApJ, 673, 271

Roche, P. F., Aitken, D. K., & Smith, C. H. 1991, MNRAS, 252, 39P

Rosenberg, D., & Wehner, G. K. 1962, Journal of Applied Physics, 33, 1842

Rosswog, S. 2007, Introduction to High Energy Astrophysics (Cambridge)

Roth, J., Bohdansky, J., & Ottenberg, W. 1979, Rpt. IPP. 9/26 (MPI Plasmaphysik, Garching)

Roth, J., Bohdansky, J., Poschenrieder, W., & Sinha, M. K. 1976, Journal of Nuclear Materials, 63, 222

Sakon, I., Onaka, T., Wada, T., et al. 2009, ApJ, 692, 546

Sarangi, A., & Cherchneff, C. accepted, A&A

Sarangi, A., & Cherchneff, I. 2013, ApJ, 776, 107

Sceats, M. G. 1989, Journal of Colloid and Interface Science, 129, 105

Seab, C. G., & Shull, J. M. 1983, ApJ, 275, 652

Sedlmayr, E. 1994, in Lecture Notes in Physics, Berlin Springer Verlag, Vol. 428, IAU Colloq. 146: Molecules in the Stellar Environment, ed. U. G. Jorgensen, 163

Serra Díaz-Cano, L., & Jones, A. P. 2008, A&A, 492, 127

Sibthorpe, B., Ade, P. A. R., Bock, J. J., et al. 2010, ApJ, 719, 1553

Sigmund, P. 1969, Physical Review, 184, 383

—. 1981, Sputtering by Particle Bombardment I, ed. R. Behrisch (Berlin, Springer)

Silvia, D. W., Smith, B. D., & Shull, J. M. 2010, ApJ, 715, 1575

—. 2012, ApJ, 748, 12

Smartt, S. J., Eldridge, J. J., Crockett, R. M., & Maund, J. R. 2009, MNRAS, 395, 1409

Spyromilio, J., & Leibundgut, B. 1996, MNRAS, 283, L89

Spyromilio, J., Leibundgut, B., & Gilmozzi, R. 2001, A&A, 376, 188

Spyromilio, J., Meikle, W. P. S., Learner, R. C. M., & Allen, D. A. 1988, Nature, 334, 327

Steidel, C. C., Pettini, M., Dickinson, M., & Persson, S. E. 1994, Astronomical Journal, 108, 2046

Sugerman, B. E. K., Ercolano, B., Barlow, M. J., et al. 2006, Science, 313, 196

Sutherland, R. S., & Dopita, M. A. 1995, ApJ, 439, 381

Suto, H., Koike, C., Sogawa, H., et al. 2002, A&A, 389, 568

Szalai, T., Vinkó, J., Balog, Z., et al. 2011, A&A, 527, A61

Temim, T., Gehrz, R. D., Woodward, C. E., et al. 2006, Astronomical Journal, 132, 1610

Tielens, A. G. G. M. 2005, The Physics and Chemistry of the Interstellar Medium (Cambridge)

Tielens, A. G. G. M., McKee, C. F., Seab, C. G., & Hollenbach, D. J. 1994, ApJ, 431, 321

Timmes, F. X., Woosley, S. E., Hartmann, D. H., & Hoffman, R. D. 1996, ApJ, 464, 332

Todini, P., & Ferrara, A. 2001, MNRAS, 325, 726

Umeda, H., & Nomoto, K. 2002, ApJ, 565, 385

van der Tak, F. F. S., Black, J. H., Schöier, F. L., Jansen, D. J., & van Dishoeck, E. F. 2007, A&A, 468, 627

Vinkó, J., Sárneczky, K., Balog, Z., et al. 2009, ApJ, 695, 619

von Helden, G., Tielens, A. G. G. M., van Heijnsbergen, D., et al. 2000, Science, 288, 313

Wakelam, V., Loison, J.-C., Herbst, E., et al. 2009, A&A, 495, 513

Wallström, S. H. J., Biscaro, C., Salgado, F., et al. 2013, A&A, 558, L2

Wang, X., Yang, Y., Zhang, T., et al. 2005, The Astrophysical Journal Letters, 626, L89

Whitelock, P. A., Catchpole, R. M., Menzies, J. W., et al. 1989, MNRAS, 240, 7P

Williams, B. J., Borkowski, K. J., Reynolds, S. P., et al. 2008, ApJ, 687, 1054

Williams, J. P., Blitz, L., & McKee, C. F. 2000, Protostars and Planets IV, 97

Wilson, T. L., & Batrla, W. 2005, A&A, 430, 561

Wooden, D. H., Rank, D. M., Bregman, J. D., et al. 1993, ApJS, 88, 477

Woosley, S. E., Hartmann, D., & Pinto, P. A. 1989, ApJ, 346, 395

Yamamura, Y., Matsunami, N., & Itoh, N. 1983, Radiation Effects, 71, 65

Zachariah, M. R., & Tsang, W. 1993, Aeros. Sci. Tech., 19, 499

Ziegler, J. F., Biersack, J. P., & Littmark, U. 1985, The Stopping and Ranges of Ions in Solids (New York: Pergamom)

Zinner, E. 2014, Treatise on Geochemistry, 2nd edition, Vol. 1 (Elsevier)

Acknowledgements

- Dr. Isabelle Cherchneff: for the opportunity to make a doctorate here at University of Basel and for showing what research really is.
- Prof. Friedrich-Karl Thielemann: for a good working environment in the Astro-group, and his help on countless occasions.
- Prof. Anthony Jones: for the helpful review of my thesis and for accepting to be the external expert at my defence.
- Prof. Alexander Tielens: for his supervision and collaboration on the analysis of Cas A observations, and for hosting me for two weeks at Leiden Observatory.

Work is not always just working, luckily... Thanks to (in alphabetical order!):

- Almudena Arcones: for introducing me to some great tapas places, for useful cake feedback and for listening to me everytime I was freaking out.
- Umberto Battino: for always finishing my cakes.
- Ruben Cabezon: for always helping me with my "shitty Mac" and with my computing problems.
- Alessandra Carrera: for all the fun all those nights out and all the gossiping.
- Matthias Hempel: for fixing my bike countless times, dragging me to swimming in the Rhine and for all the German translations.
- Roger Käppeli: for the useful German words, the silly jokes and the discussions about life, the Universe and everything (=money).
- Albino Perego: for bringing me to lunch with the others on my first days here and always helping with everything I was able to come up with.
- Marco Pignatari: for organizing countless nights out and making me discover the best food and drinks around.
- Julia Reichert: for all the translations, funny (Swiss) German words, (many) drinks out, and gossip ;). Long live the last row of the seminar room!
- The Swiss Group: for infos about Swiss life, Swiss German and everything Swiss.

As I always used to conclude my email to the group: please forward if I forgot someone!
